## *Electron Compton scattering and its application to condensed matter phenomena*

ALINA TALMANTAITE

# Electron Compton scattering and its application to condensed matter phenomena

Alina Talmantaite

A thesis presented for the degree of Doctor of Philosophy


Department of Physics
Durham University
United Kingdom

October 2022

# Electron Compton scattering and its application to condensed matter phenomena

Alina Talmantaite

**Abstract:** Investigation of electron Compton scattering using electron energy loss spectroscopy has been carried out to study projected electron momentum density distributions in amorphous carbon films, as well as two technologically important materials: few-layer $WS_2$ films, which undergo indirect-to-direct band gap transition in the monolayer limit, and $VO_2$ flakes which exhibit a metal-to-insulator transition upon cooling to below ≈67 °C.

An important concept underlying the Compton scattering measurements is the so-called impulse approximation, the validity of which is crucial for the interpretation of the Compton scattering data in terms of electron momenta in the sample. Hence, a simple material – amorphous carbon film – has been selected to test the impulse approximation at low electron scattering angles, which provides the possibility for a faster, more efficient data collection and eliminates the need for the core electron background subtraction from the acquired electron momentum density profiles via complex computational methods. Further, plasmon background subtraction has been investigated in the context of electron beam damage-resistant materials, as well as options to carry out high spatial resolution (sub-nm) Compton measurements using scanning-transmission electron microscopy.

As for electron Compton measurements in monolayer and bilayer $WS_2$, suitable experimental conditions have been first established in order to avoid any sample damage associated with the electron beam irradiation. Here, Compton scattering experiments were carried out in order to study the differences in the projected electron momentum densities in the two structures resulting from the changes in the band gap type. The results were also verified via CASTEP density functional theory calculations. Furthermore, considering that the $WS_2$ samples contained quite significant amorphous surface carbon contamination, theoretical calculations were appropriately adjusted for an improved match to the experimental measurements.

Finally, Compton scattering measurements were carried out on $VO_2$ flakes to study the properties of electrons in the metallic and insulating phases. Just as in the measurements of $WS_2$ films, optimisation of experimental conditions which minimise electron beam damage

and maximise electron count rate has been of high importance. The measured data was then compared to the theoretical predictions found in the literature, which combine both density functional theory and quantum Monte Carlo calculations to obtain the difference Compton profiles.

**Publications:** Talmantaite A, Hunt MRC, Mendis BG. Electron Compton scattering and the measurement of electron momentum distributions in solids. Journal of Microscopy. 2020;279(3):185-8.

Mendis BG, Talmantaite A. Towards electron energy loss Compton spectra free from dynamical diffraction artifacts. Microscopy and Microanalysis. 2022;1–10.

# Contents

# List of Figures

# List of Tables

# Declaration

The work in this report is based on research carried out in the Department of Physics, Durham University, United Kingdom. No part of this report has been submitted elsewhere for any other degree or qualification and it is all my own work unless referenced to the contrary in the text.

# Acknowledgements

First and foremost I would like to thank my parents for their unconditional support throughout this journey and comforting words when they were most needed.

I am extremely grateful to my PhD supervisor Dr Budhika G. Mendis for his infinite patience and guidance throughout my PhD. I could not have asked for a better mentor!

I would also like to thank my second supervisor Dr Michael R. C. Hunt for interesting and enlightening conversations about 2D materials.

I am also grateful to Mr Leon Bowen and Dr Diana Alvarez Ruiz for their enthusiasm to help with any electron microscopy-related issues.

I would also like to express my appreciation to Sam Thompson for fantastic XRD measurements of $VO_2$.

In addition, I would like to thank Prof Ariel Ismach and his team at Tel Aviv University for supplying $WS_2$ samples.

Finally, I am especially grateful to all of my friends and my housemate, Behzad, for being a source of joy in my life on a daily basis.

# Chapter 1

# Introduction

One of the key drivers of technological innovation is development of novel functional materials which could improve and completely redesign existing technology in a variety of fields such as energy generation, data storage, transport and biomedical sciences [1–5]. Successful integration of materials with tailored physico-chemical properties into device architectures is a challenging process; it requires comprehensive understanding of the material's electronic structure and ability to alter it for specific device functions and operational conditions.

The work presented in this thesis focuses on the development of electron Compton scattering as a method to study ground state electronic structure of technologically important materials. Hence, this chapter sets the background for theoretical band structure calculations within the framework of density functional theory and overviews both photon- and electron-based Compton scattering experiments, providing details on the probe-sample interaction mechanism, interpretation of the experimental data and a brief historical account of the development of the technique. Finally, it summarises alternative frequently encountered methods to measure the electronic structure of a material such as angle-resolved photoemission spectroscopy and angular correlation of electron-positron annihilation radiation.

## 1.1 Calculations of ground state electronic structure in solids

In principle, all observable properties of an arbitrary solid emerge from its unique configuration of electrons and nuclei governed by the Pauli exclusion principle and interparticle Coulomb interactions. Due to the substantial mass difference between electrons and nuclei, it is frequently assumed that electrons adjust to nuclear motion adiabatically and therefore

remain in their instantaneous ground state at any given time. This is known as the Born-Oppenheimer approximation (BOA), due to which the total wavefunction describing the solid can be separated into electronic and nuclear components [6]. Within the BOA, the ground state of the solid is then described by a many-body electronic wavefunction $\Psi_0$, which is in theory obtained solving a many-body Schrödinger equation

$$\widehat{H}\Psi = E\Psi, \tag{1.1.1}$$

where E is the total energy of the state $\Psi$ corresponding to the Hamiltonian operator $\widehat{H}$. Here, the Hamiltonian is composed of a kinetic energy operator $\widehat{T}$, electron-electron potential $\widehat{V}_{ee}$, and external potential $\widehat{V}_{ext}$ representing electron interactions with nuclei, i.e.

$$\widehat{H} = \widehat{T} + \widehat{V}_{ee} + \widehat{V}_{ext}. \tag{1.1.2}$$

However, due to a vast number of electrons comprising any practically useful material (1 g of iron, for instance, contains approximately $3 \times 10^{23}$ electrons), the number of parameters describing the many-body electronic wavefunction becomes too large for the Schrödinger equation to be solved even with the most advanced computing technology. Therefore, over the decades, a lot of effort has been placed into development of various approximations to the Schrödinger equation, among which density functional theory (DFT) has emerged as one of the most successful and widely applied techniques.

In DFT, the fundamental variable describing an arbitrary system – whether it is a solid or a molecule – is its electron density at a position $\mathbf{r}$, $n(\mathbf{r})$. Hence, all the properties of the system are expressed as functionals of electron density. The mathematical basis for this framework was laid by the Hohenberg-Kohn theorems [7] which assert that the external potential created by the nuclei, $V_{ext}(\mathbf{r})$, is a unique functional of the ground state electron density $n_0(\mathbf{r})$. In particular, given $n_0(\mathbf{r})$, the Hamiltonian describing the system and therefore all associated many-electron eigenstates and physical properties of the solid or the molecule are fully determined. Furthermore, Hohenberg and Kohn state that for a given external potential $V_{ext}(\mathbf{r})$, there exists a total energy functional $E[n(\mathbf{r})]$ which attains its minimum value for the ground state electron density $n_0(\mathbf{r})$ and represents the ground state energy of the system.

Despite reformulation of the many-body theory in terms of density functionals, Hohenberg and Kohn theorems do not provide a practical method to extract properties of materials directly from electron density. However, a major breakthrough in development of DFT was

achieved by Kohn and Sham [8], who showed that an interacting N-body system generating a particular ground state electron density can be replaced by a simpler auxiliary system of the same ground state electron density but composed of N non-interacting particles. Consequently, the ground state energy of the original system can be obtained by solving a set of single-particle Kohn-Sham equations:

$$\left[-\frac{\hbar^2}{2m_0}\nabla^2 + V_{ext}(\mathbf{r}) + V_H(\mathbf{r}) + V_{XC}(\mathbf{r})\right]\psi_i(\mathbf{r}) = \varepsilon_i\psi_i(\mathbf{r}), \tag{1.1.3}$$

where $\varepsilon_i$ is the total energy of the single particle of mass $m_0$ in a state $\psi_i$, and the Kohn-Sham Hamiltonian is a sum of the kinetic energy operator and an auxiliary effective potential consisting of electron-nuclei interaction potential $V_{ext}(\mathbf{r})$ , Hartree potential $V_H(\mathbf{r})$ describing electron-electron Coulomb interaction, and exchange-correlation potential $V_{XC}(\mathbf{r})$. The latter term corresponds to the exchange-correlation energy, which compensates for the difference between the exact total energy and the energy known from the remaining terms of the Hamiltonian. In particular, the exchange-correlation potential accounts for the interactions between electrons due to Pauli exclusion principle, electron self-interaction in the Hartree potential and discrepancies between single-particle and many-body kinetic energies. The exact form for the exchange-correlation functional for an arbitrary solid is not known; nonetheless, there are a number of methods which can be used to approximate it. One of the simplest ones is local density approximation (LDA), in which the exchange-correlation functional for a solid of electron density $n(\mathbf{r})$ is replaced with a known functional for a homogeneous free electron gas of the same density [6]. However, in the systems where electron density varies considerably, LDA fails to produce a sufficient degree of accuracy and can be replaced by an appropriate parametrisation of generalised gradient approximation (GGA), which takes into account the gradient of the electron density. Once an explicit expression for the exchange-correlation functional is selected, Kohn-Sham equations can be solved for self-consistency as outlined in Fig. 1.1.

It is important to note that in the case of crystalline materials (or isolated molecules modelled via construction of a periodic supercell), the DFT exploits Bloch's theorem to generate the single particle states $\psi_i$ (a.k.a. Kohn-Sham orbitals) as a sum of plane waves

$$\psi_i(\mathbf{r}) = \sum_{\mathbf{G}} c_{i,(\mathbf{k}+\mathbf{G})} e^{i(\mathbf{k}+\mathbf{G})\cdot\mathbf{r}} \tag{1.1.4}$$

where $\mathbf{G}$ is a reciprocal lattice vector, $\mathbf{k}$ is a wave vector within the 1st Brillouin zone,

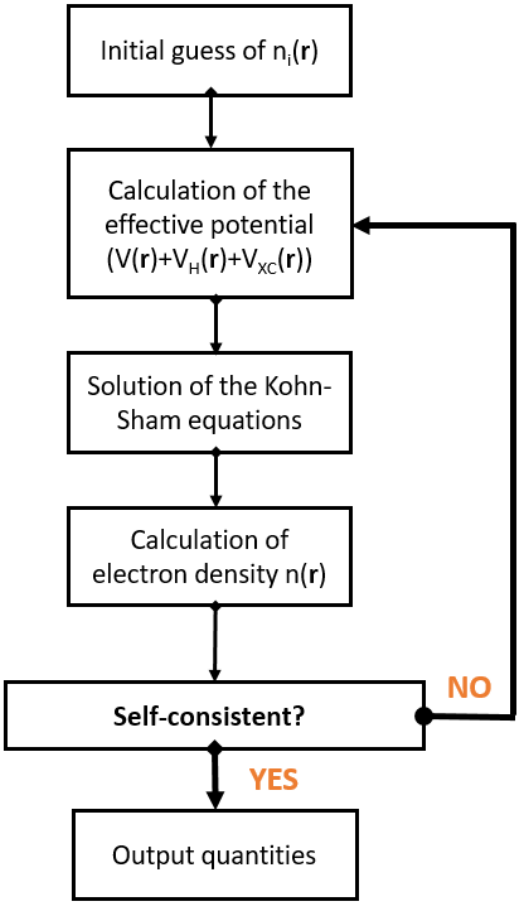


Figure 1.1: Diagram of the self-consistent approach to solve Kohn-Sham equations (adapted from [6]).

and $c_{i,(\mathbf{k}+\mathbf{G})}$ are the coefficients of the plane waves[1]. Technically, the above equation is a sum over an infinite number of reciprocal lattice vectors, but for computational purposes a cut-off value can be selected, for which $c_{i,(\mathbf{k}+\mathbf{G})}$ coefficients are negligibly small. While the plane wave approach produces a simple way to define single-particle wavefunctions and Kohn-Sham equations, it requires a large number of plane waves to describe tightly bound core electrons and rapidly oscillating valence electron wavefunctions within the core region. Hence, considering that most physical properties of solids depend on valence electrons, the plane-wave DFT additionally employs a pseudopotential approximation [9], which replaces the Coulomb potential of the nucleus and core electrons with a weaker pseudopotential acting on the so-called pseudo-wavefunctions. Outside the core region of a cut-off radius $r_c$, the pseudo-wavefunctions match the wavefunctions of valence electrons, but within the core they

[1] Isolated atoms, molecules and clusters can also be modelled using localised basis sets; however, application of such methods is beyond the context of this thesis.

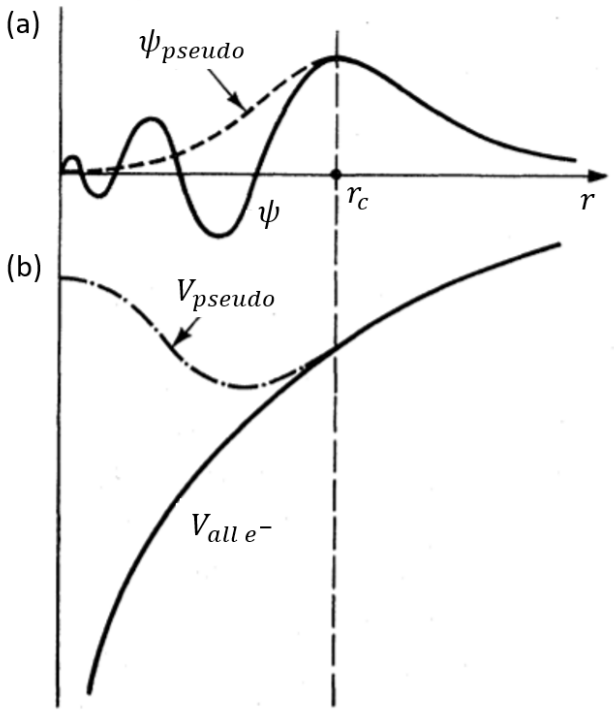


Figure 1.2: Schematic representation of the differences between (a) pseudo-wavefunctions $\psi_{pseudo}$ and real wavefunctions $\psi$, and (b) corresponding pseudopotentials $V_{pseudo}$ and all-electron potentials $V_{all\ e^-}$ (adapted from [10]).

are smooth and have no nodes, as shown in Fig. 1.2. The two most commonly used types of pseudopotentials are norm-conserving and ultrasoft pseudopotentials [6]. The difference between the two lies in the charge density they generate inside the core region $r_c$. The norm-conserving methods preserve the charge density of the original all-electron core; however, the accuracy they provide comes at the expense of increasing computational complexity. For certain elements, the constructed pseudo-wavefunctions are not significantly smoother than all-electron wavefunctions and therefore still require a large plane wave basis set. The ultrasoft pseudopotential methods, on the other hand, relax the charge density conservation and generate smooth pseudo-wavefunctions. The accuracy of ultrasoft methods is maintained by additional computational processes; however, the overall computational complexity is greatly reduced due to a relatively small number of plane waves required to describe pseudo-wavefunctions.

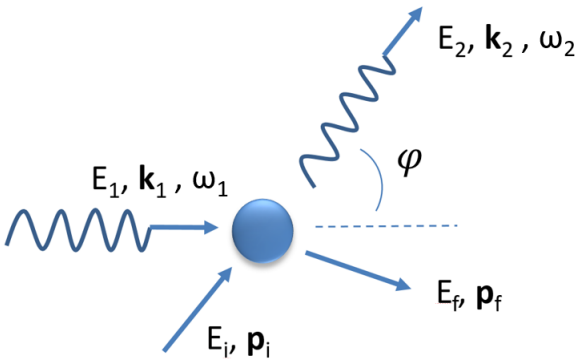


Figure 1.3: Compton scattering between a photon and an electron.

## 1.2 Measurements of ground state electronic structure in solids

### 1.2.1 Compton scattering

Usually Compton scattering is thought of as an inelastic scattering process between a high frequency photon and a charged particle, such as an electron, which results in an increase of the photon wavelength and its deflection from the original direction of propagation, as shown in Fig. 1.3. The change in the photon wavelength is captured by the well-known Compton shift equation:

$$\Delta\lambda = \frac{h}{m_0 c}(1 - \cos\phi), \tag{1.2.1}$$

where $\Delta\lambda$ is the shift in photon wavelength, $h$ is the Planck constant, $m_0$ is the electron rest mass, $c$ is the speed of light and $\phi$ is the scattering angle [11–13].

Derivation and experimental verification of Eqn. 1.2.1 [14,15] demonstrated the particle nature of electromagnetic radiation and became one of the most prominent breakthroughs in physics of the early 20$^{\text{th}}$ century. It earned A.H. Compton the Nobel prize in 1927 and laid foundations for the development of modern quantum mechanics. The given wavelength shift equation, however, describes a photon interaction with a free stationary electron and implies that there is a one-to-one correspondence between the scattering angle and the measured energy loss for monochromatic radiation. Hence, it does not fully reflect experimental results for real materials, which show broader Compton scattering peaks than expected from experimental geometry and spectrometer resolution. The observed Doppler broadening of the Compton lineshape, which is shown schematically in Fig. 1.4, was first successfully related to the electron motion in the target material by DuMond [16] and served as one of the earliest evidence of the validity of Fermi-Dirac statistics and the Pauli exclusion principle for electrons.

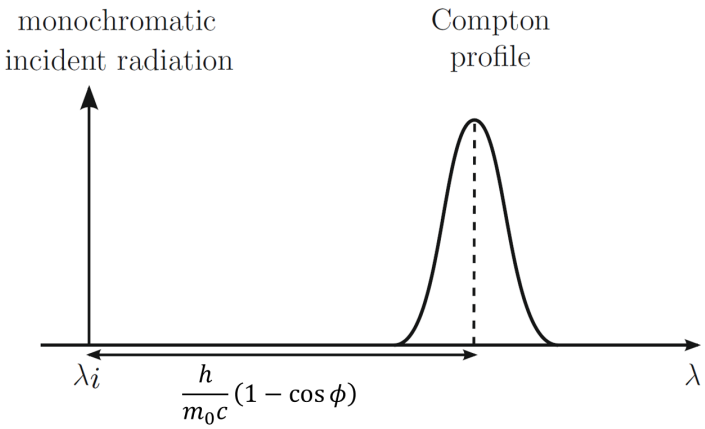


Figure 1.4: Schematic representation of a Doppler-broadened Compton profile (adapted from [17]). The broken line represents scattering by a free stationary charged particle (such as an electron) as defined by Eqn. 1.2.1.

The relation between the electron momentum density distribution and the measured Compton scattering spectrum as an energy loss distribution is not always straightforward. The following further outlines Compton scattering kinematics for a relatively simple case of non-relativistic X-ray scattering for the purpose of illustrating the correspondence between the measured spectrum and the electron momentum density. A more detailed account of the scattering interaction can be found in [11].

Considering the scattering setup displayed in Fig. 1.3, Compton experiments measure the energy and intensity of a monochromatic photon scattered at a fixed scattering vector $\mathbf{q}$ into a solid angle $d\Omega$. As the photon energy is determined with a resolution $d\omega_2$, one essentially measures a double differential scattering cross section (DDSCS), $\frac{d^2\sigma}{d\Omega d\omega_2}$ [11,12]. However, direct transformation of the DDSCS into an electron momentum density profile $J(p_z)$ can be carried out only if certain experimental conditions are satisfied. For non-relativistic X-rays, which have energy of a few tens of keV, the coupling between the probe and the target electron system is defined by an interaction Hamiltonian,

$$H_{\text{int}} = \sum_j \frac{e^2}{2m_0c^2}\mathbf{A}(\mathbf{r}_j)^2 - \sum_j \frac{e^2}{2m_0c}\mathbf{A}(\mathbf{r}_j)\cdot\mathbf{p}_j, \tag{1.2.2}$$

where $\mathbf{A}$ is the magnetic vector potential of the photon, $\mathbf{p}$ is the electron momentum operator and the summation is carried out over the target electrons [11]. When the impinging photon energy satisfies resonance conditions, i.e. $\hbar\omega_1 \approx E_N - E_I$, where $E_N$ is the energy of an intermediate electron state $|N\rangle$ that is associated with photon absorption and re-emission, the interaction Hamiltonian is dominated by the $\mathbf{A}\cdot\mathbf{p}$ term. However, under experimental conditions when the photon energy is far from the resonance absorption, one reaches the

Compton regime of inelastic scattering, and the interaction Hamiltonian consists of first order $\mathbf{A}^2$ terms [11,12]. This corresponds to the Born approximation, when the coupling between the incident electromagnetic field and the target system is weak. Consequently, the DDSCS for inelastic scattering of non-relativistic X-rays can be expressed as:

$$\frac{d^2\sigma}{d\Omega d\omega_2} = \left(\frac{d\sigma}{d\Omega}\right)_{\mathrm{Th}} S(\mathbf{q},\omega), \tag{1.2.3}$$

where $\left(\frac{d\sigma}{d\Omega}\right)_{\mathrm{Th}}$ is the Thomson scattering cross section and $S(\mathbf{q},\omega)$ is the dynamic structure factor [11–13]. The latter describes the dynamics of the scattering electrons and is given by

$$S(\mathbf{q},\omega) = \sum_F \left| \langle F| \sum_j \exp(i\mathbf{q}\cdot\mathbf{r}_j) |I\rangle \right|^2 \delta(E_F - E_I - \hbar\omega), \tag{1.2.4}$$

where $|I\rangle$ and $|F\rangle$ are the initial and final electronic states of the solid, which have energies $E_I$ and $E_F$ respectively [11]. Further, in order to express the DDSCS in terms of the Compton profile capturing the electron momentum density distribution, one has to consider inelastic scattering within the impulse approximation, which assumes that relaxation of background electrons and nuclei in the target is negligible during the photon-electron collision [11,12]. Therefore, any changes in the potential energy can be ignored, and energy conservation equations can be simplified to kinetic energy terms. It implies that the difference between the total initial and final electron state energies in the argument of the Dirac delta function in Eqn. 1.2.4 can be replaced by the difference of their kinetic energies. Then, defining the momentum of the initial electron state as $\mathbf{p} \equiv \mathbf{p}_f - \hbar\mathbf{q}$, where $\mathbf{p}_f$ is the momentum of the electron in the final free state, one can eventually write the DDSC as

$$\frac{d^2\sigma}{d\Omega d\omega_2} = \left(\frac{d\sigma}{d\Omega}\right)_{\mathrm{Th}} \frac{m_0}{\hbar q} \iint \rho(p_x,\ p_y,\ p_z = p_q) dp_x dp_y, \tag{1.2.5}$$

where the Compton profile is expressed as

$$J(p_z) = \iint \rho(p_x,\ p_y,\ p_z = p_q) dp_x dp_y, \tag{1.2.6}$$

and represents the projection of the target electrons' probability density distribution $\rho(\mathbf{p})$ along the scattering vector $\mathbf{q}$, which is set to lie in the z-direction [11]. In its essence, the impulse approximation describes scattering by free electrons, which have a momentum distribution of bound electrons. It is satisfied when the scattering experiments are carried out using photon energies that are much higher than the binding energies of the electrons in the sample [11,12]. Under the impulse approximation, the energy transfer from the photon to a

recoil electron is then given by:

$$E_I - E_F = \frac{\hbar^2 \mathbf{q}^2}{2m_0} + \frac{\hbar \mathbf{q} \cdot \mathbf{p}}{m_0}. \tag{1.2.7}$$

The first term in Eq. 1.2.7 can be interpreted as the Compton shift for scattering by a stationary electron and the second term is a Doppler shift, which shows that the change in the photon energy is linearly dependent on the component of electron's ground-state momentum along the scattering vector $\mathbf{q}$ [11,12]. Finally, at low photon beam energies ($\ll m_0c^2$) Eqn. 1.2.7 can be simplified to

$$E_I - E_F = \frac{2E_I}{m_0 c} \sin(\frac{\phi}{2}) p_z, \tag{1.2.8}$$

from which the projection of electron momentum along the scattering vector ($p_z$) can be easily derived from the photon energy loss data [12]. Also note that the Compton profile $J(p_z)$ is subject to a normalisation rule:

$$\int_{-\infty}^{+\infty} J(p_z) dp_z = Z, \tag{1.2.9}$$

where $Z$ is the number of electrons participating in scattering [11,12]. Integration of the Compton profile according to Eqn. 1.2.9 is frequently used to convert the measured photon count rate (i.e. the y-axis of the energy loss data) into electron momentum density $J(p_z)$ axis. A schematic of a Compton profile expected from the measurements satisfying Born and impulse approximations is shown in Fig. 1.5. It consists of both valence and core electron contributions. The valence electrons move at relatively low speeds producing small Doppler shifts and narrow Compton peaks. The core electrons, on the other hand, move at higher speeds and create a wide background in a Compton spectrum [11,12]. As physical and chemical properties of materials are determined by valence electrons, the core electron contribution can be calculated using density functional theory (DFT) and subtracted [18].

In the context of photon Compton scattering, circularly polarised electromagnetic radiation can be utilised to study spin-polarised projected electron momentum densities. In particular, for circularly polarised radiation the DDSCS includes a spin-dependent magnetic contribution, which can be separated from the usual charge scattering terms by either switching the polarisation handedness of the impinging radiation or the direction of the material magnetisation [19]. Under the impulse approximation, the magnetic Compton profile is then expressed as:

$$J_{mag}(p_z) = \iint [\rho^{\uparrow}(\mathbf{p}) - \rho^{\downarrow}(\mathbf{p})] dp_x dp_y, \tag{1.2.10}$$

where $\rho^{\uparrow}$ and $\rho^{\downarrow}$ are the spin-up and spin-down electron momentum densities [19]. Note that

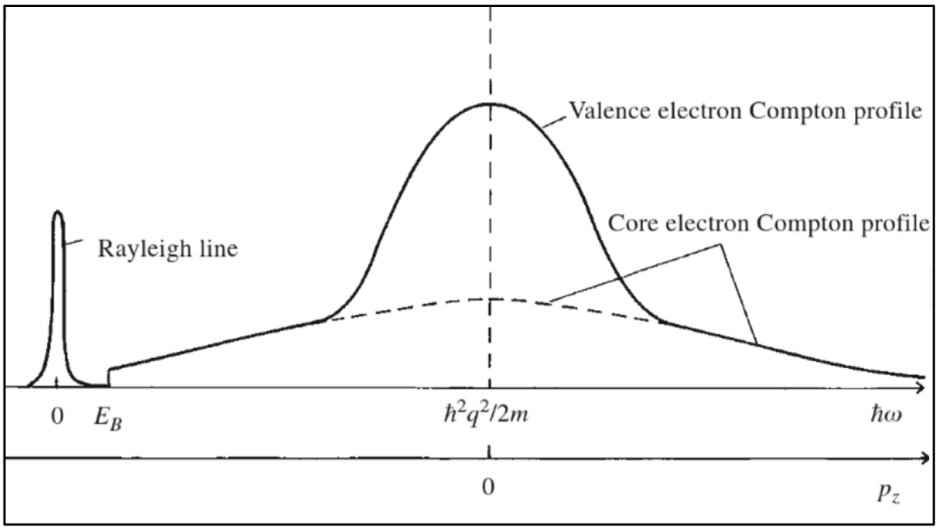


Figure 1.5: Schematic representation of a Compton profile plotted as a function of both photon energy loss $E_I - E_F$ and the projected electron momentum $p_z$ [11]. Within the impulse approximation, the energy transfer exceeds the core electron binding energy $E_B$, and the Compton profile consists of both core and valence electron contributions.

while the overall magnetic moment of a sample consists of both spin and orbital magnetic moment contributions, magnetic Compton scattering is only sensitive to the spin-related contribution [20, 21].

The early Compton scattering experiments conducted using X-rays from conventional X-ray sources such as Cu K$\alpha$ at 8.4 keV or Ag K$\alpha$ at 22.2 keV faced some practical difficulties associated with competing photon-matter interactions [11]. As shown in Fig. 1.6. the primary contribution to the photon scattering cross section under the usual experimental conditions arises from the photoelectric effect, which greatly diminishes the Compton signal and hinders the study of a large number of chemical elements. Hence, up until the 1980s good quality Compton data using an X-ray probe could be obtained only for the lightest elements such as hydrogen, helium, neon, molecular oxygen and nitrogen [11]. Measurement of Compton profiles for heavier elements was eventually achieved due to the developments in $\gamma$-ray experimental methodology in the 1970s. It offered stable, monochromatic probes provided by radioisotopes such as $^{241}$Am (59.54 keV), $^{198}$Au (412 keV) and $^{51}$Cr (320 keV) [11]. Also, contrary to X-rays, which satisfied the impulse approximation only for the valence electrons and presented difficulties in modelling and subtraction of the core electron contribution from the measured Compton profiles, $\gamma$-ray experiments ensured impulsive collisions with all the electrons in the sample. This allowed for a straightforward prediction of the core electron Compton profiles from the free-atom wavefunctions. However, the advantages offered by the $\gamma$-ray probes came at the expense of a reduced experimental resolution and an

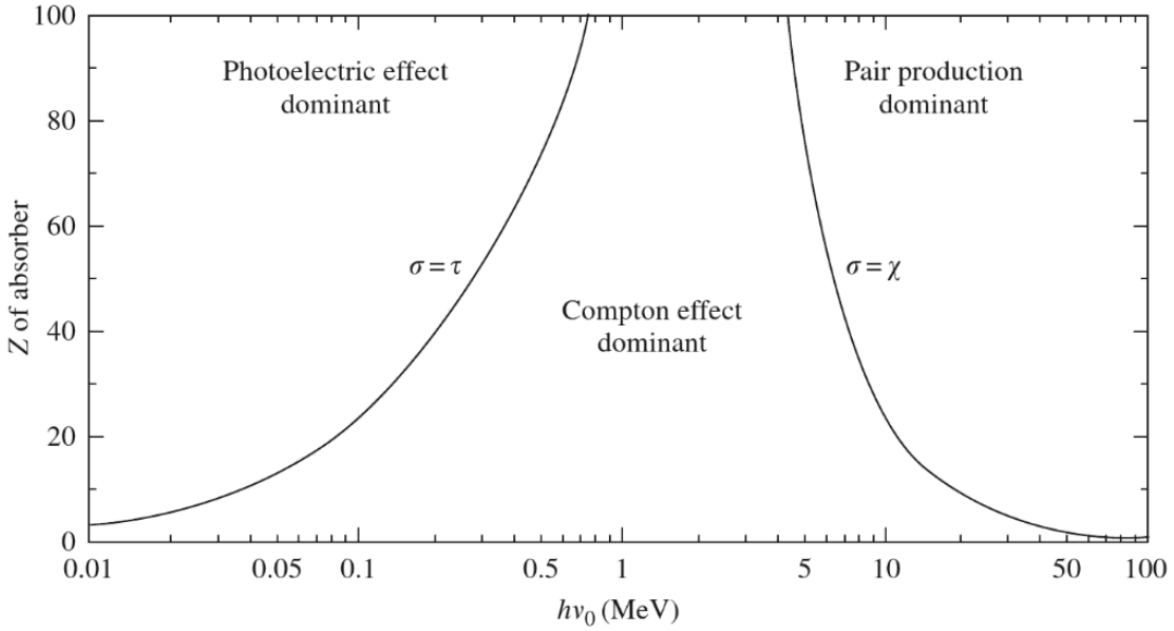


Figure 1.6: Competing interaction mechanisms between X-rays of energy $h\nu_0$ and an absorbing material of atomic number Z. The solid lines indicate experimental conditions under which the scattering cross-sections for different effects are equal [11].

increase in the measurement time, which reached weeks compared to days needed for X-ray measurements [11].

### Electron Compton scattering

The concepts governing Compton scattering of photons and the interpretation of the photon energy loss data in terms of the target electron momentum density distribution can be equally applied to experiments in which a probing particle is an electron. In this case, the DDSCS within an impulse approximation can be expressed as

$$\frac{d^2\sigma}{d\Omega dE} = \left[\frac{2m_0e^2}{(\hbar q)^2}\right]^2 \frac{m_0}{(2\pi)^2 q}\frac{k_b}{k_a}\iint \rho(p_x,\ p_y,\ p_z = p_q)dp_x dp_y, \tag{1.2.11}$$

where $E$ is the energy loss and $k_a$, $k_b$ are the wave numbers of the primary and scattered electron respectively [22].

The first electron Compton scattering experiments on atoms and molecules such as as helium, nitrogen and methane were conducted by A.L. Hughes *et al.* in the late 1930s using an apparatus consisting of an electron gun, collision chamber and an electrostatic analyzer [23,24]. The experiments were not entirely successful and therefore essentially halted until the early 1970s, when higher precision results for a number of different gases such as Ne, Ar, $H_2$ and $CO_2$ were obtained [25,26]. Substantial developments of the technique were carried out in the

1980s after B.G. Williams *et al.* proposed a new approach to measure Compton profiles using transmission electron microscopes (TEM) equipped with electron energy loss spectrometers (EELS) [27]. This method enabled the measurement of electron momentum density profiles of thin solid films that were otherwise inaccessible via earlier electron Compton measurements due to beam damage and multiple scattering effects.

Generally, TEM-based Compton scattering experiments offer a few major advantages over the traditional photon-based experiments: (i) several orders of magnitude higher inelastic scattering cross section at typical scattering angles, (ii) higher electron source brightness, (iii) a sample size threshold as small as a few nanometres in area, (iv) higher momentum resolution and (v) compatibility with simultaneous electron diffraction and energy dispersive X-ray (EDX) measurements [11, 28–30]. However, a higher inelastic scattering cross section also introduces a higher probability for multiple scattering of primary electrons within insufficiently thin samples. It predominately occurs via a combination of a large-angle (quasi-) elastic and low-angle inelastic scattering events, which in turn create a relatively high background that is not easy to subtract due to a large width of the Compton peak [31]. Hence, while the first TEM-based experiments on carbon materials [27, 32] demonstrated the feasibility of the technique, the potential applications at that time were still limited by the sample thickness, as well as insufficient performance of the associated instrumentation and radiation damage. For this reason, quite sparse experimental studies were primarily focused on the optimisation of experimental conditions.

Subsequent developments in the TEM optics and electron detection made in the following decades have greatly improved the quality of Compton measurements, however, it remains a quite underdeveloped and rarely applied technique. In recent years, only a handful of experiments have been carried out on materials such as graphite, few-layer graphene and nanodiamonds [28, 33–35]. Just as in photon Compton experiments, these measurements have been conducted in a high energy transfer regime (i.e., significantly above the binding energy of the recoil electron) in order to satisfy the impulse approximation. This results in a relatively low electron count rate, while the Compton profiles thus obtained include contributions from both valence and core electrons. Therefore, one of the goals of the work presented in this thesis is to investigate electron Compton scattering in amorphous carbon films in a 'low energy' transfer regime at small electron scattering angles. In this regime, only valence electrons are Compton scattered, which can remove the core electron background subtraction procedures and increase the electron count rate. The potential of this technique can further be tested using technologically important 2D materials, which in principle eliminate the aforementioned

experimental issues associated with the sample thickness and multiple scattering. The 2D systems at the focus of this thesis are monolayer and bilayer $WS_2$ films, which undergo a direct-to-indirect band gap transition with an increasing sample thickness. Lastly, in this work the sensitivity of electron Compton scattering is investigated by studying the effects of the metal-to-insulator phase transition on the projected electron momentum density distribution in $VO_2$. The current advances in both photon and electron Compton scattering experiments in the relevant 2D and metal-insulator transition material groups are further presented in Chapter 2, which also outlines the dominant projected electron momentum measurement strategies.

### 1.2.2 Alternative techniques

#### Angle-resolved photoemission spectroscopy

Angle-resolved photoemission spectroscopy (ARPES) is one of the major experimental techniques used to study electronic structure of solids. It is based on the photoelectric effect, which describes the energetics of electron emission from a solid upon its irradiation with photons of sufficient energy (i.e. above the work function of the solid). Photoemission is typically described as a phenomenological three-step process, which involves (i) optical excitation of a bound electron to an excited Bloch eigenstate in bulk material, (ii) propagation of the excited electron towards the surface and (iii) transmission of the photoelectron through the surface potential barrier into vacuum[2] [36]. Relaxation of the system during the photoemission process is neglected within the framework of the impulse approximation (or sudden approximation), which assumes that there are no interactions between the system and the electron after the collision.

ARPES experiments are carried out using monochromatic radiation (e.g. from a synchrotron X-ray beam line, a gas discharge lamp or laser source), which is directed at a monocrystalline sample [37]. Photoemitted electrons are then collected by an electron analyser, which measures their kinetic energy $E_{kin}$ for a given direction of emission and hence completely determines their momentum $\mathbf{k}^{out}$ in vacuum [36], as shown in Fig. 1.7(a). Subsequently, $E_{kin}$

[2]From a rigorous quantum mechanical perspective, the photoemission process should be treated as a one-step process, i.e. an optical transition between the initial N-electron eigenstate of the semi-infinite crystal to the final (N-1)-electron eigenstate described by a certain probability and subject to appropriate boundary conditions at the surface of the crystal. However, due to the complexity of the quantum mechanical description, the three-step process is preferred in practice [36].

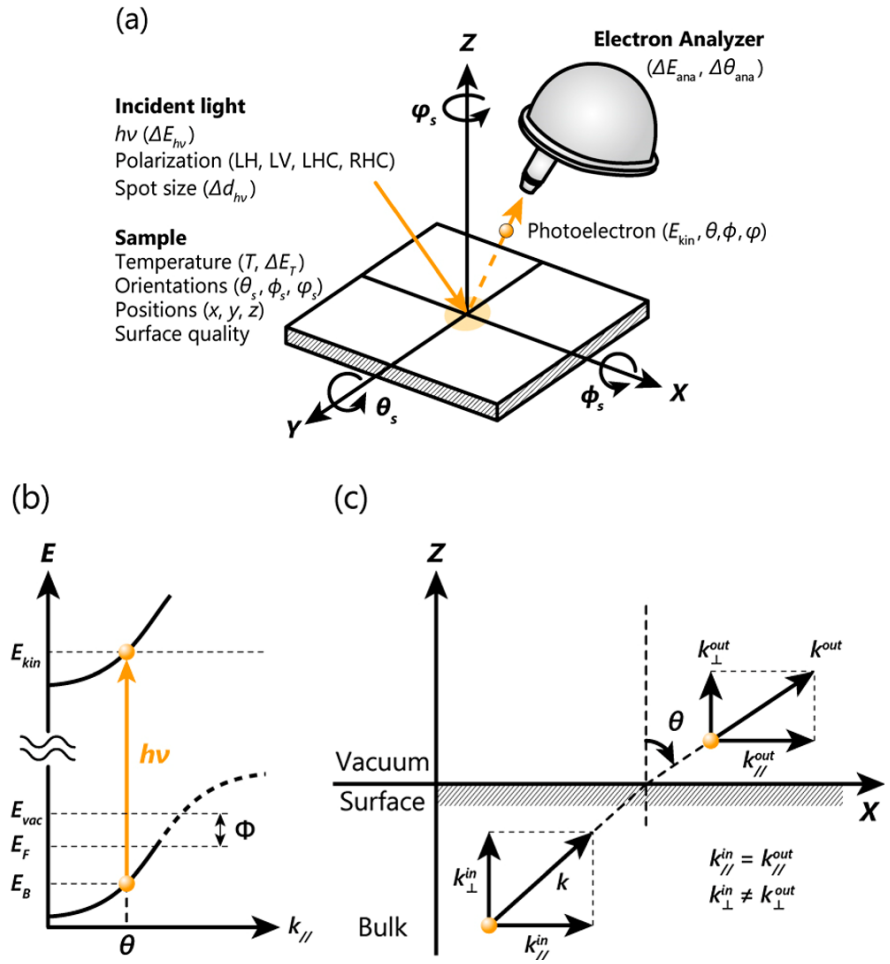


Figure 1.7: (a) Schematic representation of ARPES experimental set-up and major experimental variables. Electronic dispersion of a sample is reconstructed from the measured $E_{kin}$ and $\mathbf{k}^{out}$ of photoemitted electrons using energy (b) and momentum (c) conservation laws [37].

and $\mathbf{k}^{out}$ are used to determine electron binding energy $E_B$ and momentum $\mathbf{k}$ in bulk using total energy and momentum conservation laws (shown schematically in Fig. 1.7(b) and 1.7(c)). Note that while the momentum component parallel to the surface of the sample $\mathbf{k}_{//}$ is conserved, the perpendicular component $\mathbf{k}_\perp$ is not. Hence, ARPES is particularly suited to study low-dimensional materials, which have negligible electronic dispersion along the surface normal [36,38]. As for three-dimensional materials, which require full knowledge of the crystal momentum $\mathbf{k}$ to reconstruct electronic dispersion $E(\mathbf{k})$, perpendicular momentum component $\mathbf{k}_\perp^{in}$ can be derived from band structure calculations, determined from additional photoemission measurements for which $\mathbf{k}_{//}^{out} = \mathbf{0}$ or from complementary experimental techniques such as very-low-energy electron diffraction [36,39]. An example of electronic dispersion maps for $WS_2$/graphene heterostructures measured via ARPES is shown in Fig. 1.8 [40].

Over the years, functionality of ARPES technique has been expanded to include spin, spatial and temporal resolution features in order to facilitate studies of magnetic properties of ma-

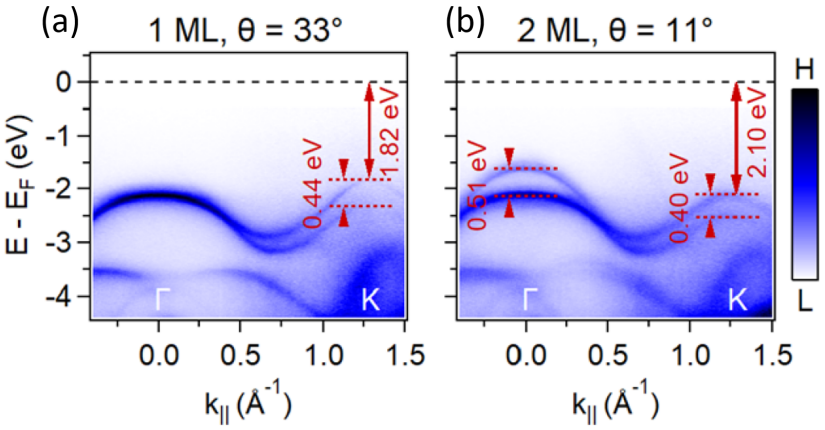


Figure 1.8: Electronic band structure of (a) monolayer, 1 ML, and (b) bilayer, 2 ML, $WS_2$ films deposited on graphene [40]. Measurements were carried out via ARPES using 100 eV photon probe with a spot size of 600 nm. Angle $\Theta$ corresponds to the twist angle between $WS_2$ and graphene.

terials, local electronic structure and its dynamic changes respectively [37]. Careful tuning of experimental conditions allows for energy resolution of the order of ≈1 meV, temporal resolution of up to 11 fs and angular resolution reaching 0.05° on modern ARPES instruments [37].

### Angular correlation of electron-positron annihilation radiation

Measurement of angular correlation of electron-positron annihilation radiation (ACAR) is one of the more commonly encountered experimental techniques used to study electron momentum density distribution in solids. A diagram of an ACAR experimental setup is shown in Fig. 1.9. Here, a positron with an energy of $\lesssim 1$ MeV is emitted by a radioactive source (typically $^{22}$Na, $^{58}$Co or $^{64}$Cu) and implanted into a sample, where it thermalises with the crystal lattice through inelastic interactions such as electron-hole pair generation, ionisiation events, plasmon and phonon excitations [41]. In a highly crystalline material, a thermalised positron further diffuses as a delocalised Bloch wave and eventually annihilates with an electron in the sample emitting a pair of $\gamma$-photons. Decay into a single or multiple photons is also possible, but probabilities of these processes are low [41].

In the centre-of-mass frame of electron-positron annihilation, the two photons are emitted in anti-parallel directions with an energy of 511 keV each. However, due to the net momentum of the electron-positron pair in the laboratory frame, deviations in the photon energy and emission trajectory occur (Fig. 1.9) [41]. The measured deflections in the photon angular distribution are in principle related to two-photon momentum density, but thermalisation of the positron in the sample implies that the photon momenta essentially describe the electron

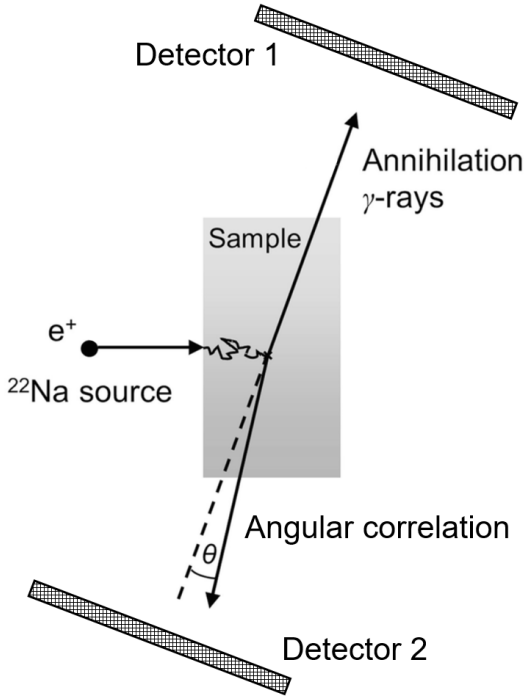


Figure 1.9: Schematic representation of an ACAR experimental setup. Image adapted from [42].

momentum density in the crystal. Due to strong Coulomb repulsion between positrons and atomic cores, the main contribution to annihilation events and therefore momentum density profiles comes from valence electrons [41, 42]. It is also important to note that the data of ACAR experiments are subject to certain distortions, i.e. electron wavefunctions are altered by the positron within the sample; hence, the measurements have to be corrected and interpreted appropriately.

Depending on the type of an ACAR detector, which can have either a long-slit or two-dimensional geometry, the measured electron momentum densities are represented either as 1D or 2D projections. These are very similar to electron momentum density profiles measured via Compton scattering, as shown in Fig. 1.10. 3D electron momentum density can also be reconstructed by taking 2D measurements along various crystallographic directions [42–44]. Momentum resolution attainable in ACAR measurements depends on the angular resolution of the detectors, positron spot size and the sample temperature [45]. In principle, the detector angular resolution can be improved by increasing the detector-detector distance; however, that in turn reduces the count rate. Recently, 2D-ACAR measurements have been performed with $(0.21 \times 0.17)$ a.u.$^2$ momentum resolution, where the momentum components are normal to the detector-detector direction [46].

In addition to electron momentum density studies via angular-correlation experiments, electron-

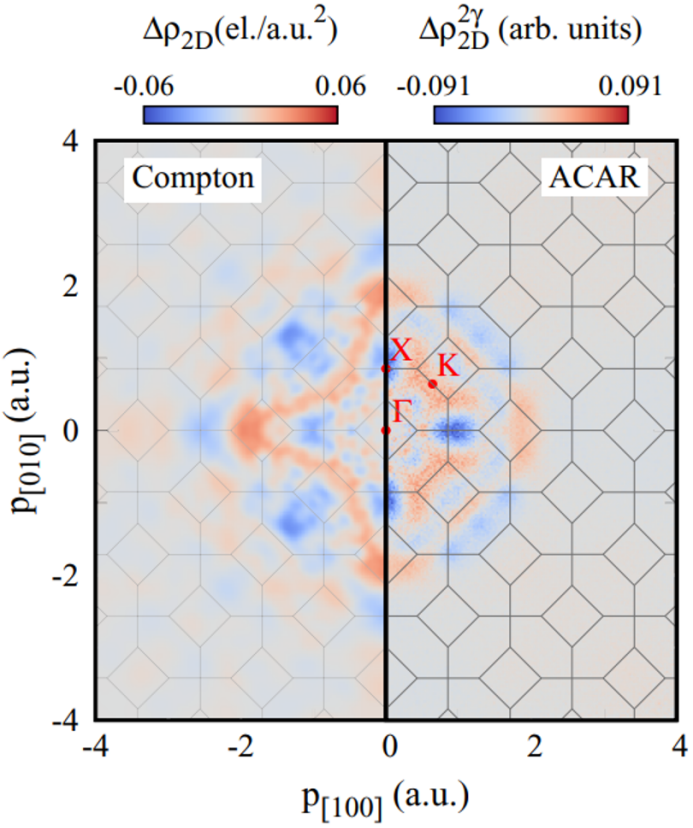


Figure 1.10: Comparison between 2D radial anisotropy of projected electron momentum distribution of Pd measured via Compton scattering and ACAR [46]. 2D Compton projections were generated from 10 1D Compton spectra. ACAR measurements show larger anisotropy at low momenta and lower anisotropy at high momenta compared to the corresponding Compton measurements. This occurs due to preferential sampling of valence electrons via ACAR [46].

positron annihilation can be used to study defects via measurements of positron lifetime and Doppler broadening of the $\gamma$-photons [41, 42, 47]. While ACAR experiments require samples of high crystallinity where positrons propagate as delocalised Bloch waves, samples of sufficiently high defect density exhibit positron trapping in localised states before annihilation with electrons. Trapping occurs in low-density regions of the sample such as vacancies, dislocations and grain boundaries [41, 42, 47]. This leads to an increase in positron lifetime, the measurement of which provides information on the total electron density in the area where electrons and positrons annihilate. Local electron momentum density distribution of these vacancy-type defects is further characterised by the Doppler broadening experiments. Doppler broadening can also be used to study overall electron momentum density distribution of the sample; however, its resolution is inferior to that of ACAR experiments [41, 47].

# Chapter 2

# $VO_2$ and TMD materials background

Meeting growing global technological demands while achieving sustainable development goals is one of the biggest challenges society will face in the coming decades. This can be addressed in part by development of next-generation low-power electronic and optoelectronic devices, which utilise novel materials with superior physical and chemical properties. Two of such materials - $VO_2$ exhibiting reversible metal-insulator transition and two-dimensional semiconducting $WS_2$ - are at the focus of the electron Compton scattering experiments presented in this thesis. Hence, this chapter describes physical and electronic structure of the given materials, outlines a number of their potential applications and overviews the state of progress in the associated Compton scattering experiments.

## 2.1 $VO_2$ and metal-insulator transitions

### 2.1.1 Structure of $VO_2$

The first report on a temperature-dependent transition between metallic and insulating states in vanadium dioxide ($VO_2$) was published by Morin in 1959 [48]. The material and its peculiar resistance behaviour, as depicted in Fig. 2.1, has attracted a lot of attention, not only due to a wide range of potential applications (Sec. 2.1.2), but also due to the underlying transition mechanism, the fundamental description of which has remained controversial up to this day [49, 50].

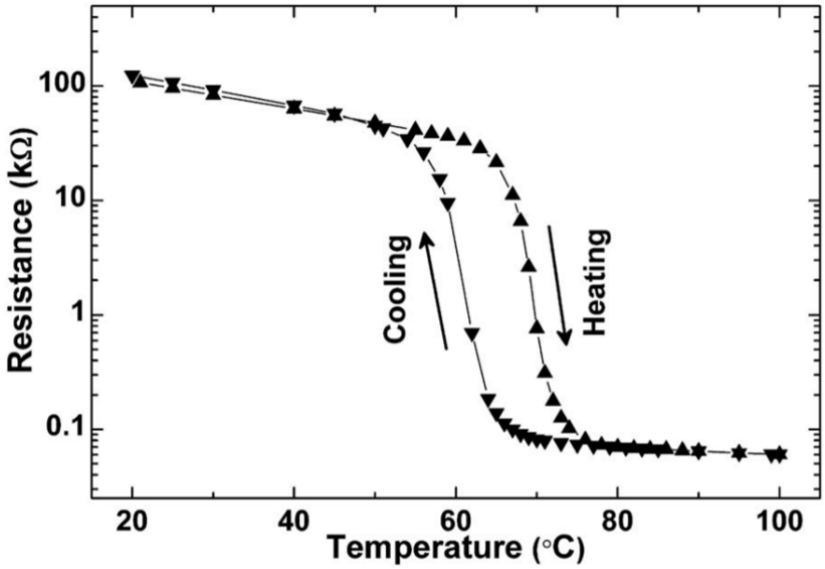


Figure 2.1: Resistance-temperature plot of a $VO_2$ film showing a metal-insulator transition (MIT) with changes in resistivity reaching three orders of magnitude [51]. The MIT is associated with the $VO_2$(M1) and $VO_2$(R) polymorphs. Heating and cooling processes show a hysteresis loop which is typically associated with different phase transition paths due to strain, lattice defects and doping [52].

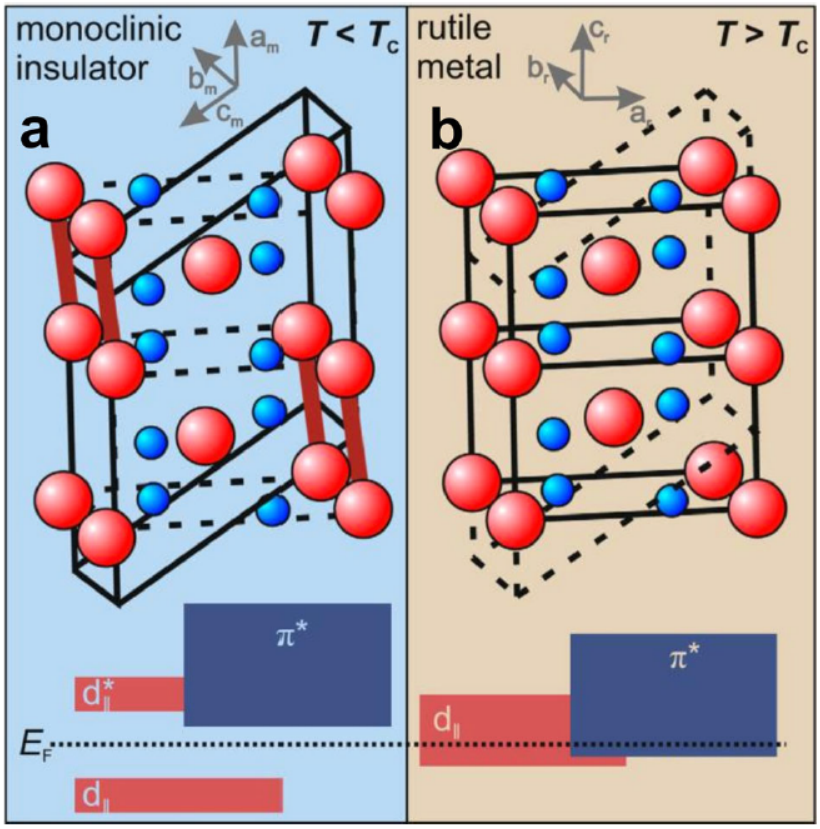


Figure 2.2: Crystal structure and band structure of insulating monoclinic $VO_2$(M1) crystal (a) and metallic tetragonal (rutile) $VO_2$(R) crystal (b). Vanadium atoms are labeled in red, while oxygen is in blue. The solid lines represent unit cells for each phase, and the dashed lines show the unit cells of the opposite phase for direct comparison. In $VO_2$(R), the nearest V-V atoms are 0.287 nm apart, while in $VO_2$(M1) V-V pairs with interatomic distances of 0.312 nm and 0.265 nm are formed. The bottom sections of each panel show electronic band structure near the Fermi level for the respective crystal structures [50,53].

Table 2.1: Crystal structures and lattice constants of $VO_2$(M1) and $VO_2$(R) polymorphs (adapted from [54]).

| **$VO_2$ polymorphs** | **Crystal structure (space group)** | **Lattice constants in bulk** | | | |
|---|---|---|---|---|---|
| | | ***a*** (Å) | ***b*** (Å) | ***c*** (Å) | $\beta$ (°) |
| $VO_2$(M1) | Monoclinic ($P2_1/c$ (14)) | 5.38 | 4.52 | 5.74 | 122.6 |
| $VO_2$(R) | Tetragonal ($P4_2/mnm$ (136)) | 4.55 | 4.55 | 2.86 | |

$VO_2$ can generally take a number of crystalline phases, each of which exhibits interesting and complex physical and chemical properties due to strong electron correlation [52,54,55]. However, the resistance behaviour shown in Fig. 2.1 is associated with $VO_2$(M1) and $VO_2$(R) polymorphs, linked to each other via a reversible, temperature-driven metal-to-insulator transition (MIT) accompanied by a structural tetragonal-to-monoclinic phase transition. The changes in the system occur essentially instantaneously [56] at a transition temperature of approximately 68 °C, above which insulating $VO_2$(M1) turns into metallic $VO_2$(R). In the metallic $VO_2$(R) phase, $V^{4+}$ ions are located at the vertices and body centre of a tetragonal unit cell, as shown in Fig. 2.2(b). Each $V^{4+}$ ion is further surrounded by six $O^{2-}$ ions, forming an octahedral $VO_6$ structural unit. Once the temperature of the systems drops below the critical temperature, the highly symmetric tetragonal unit cell becomes distorted, i.e. vanadium atoms tilt with respect to their positions in the $VO_2$(R) phase and form V-V pairs stacked along the rutile *c*-axis ($c_r$) with two different interatomic lengths, as shown in Fig. 2.2(a). Compared to vanadium atoms, positional changes in oxygen octahedra are minor. Consequently, the resulting insulating $VO_2$(M1) phase is then described by a monoclinic unit cell that is essentially twice as large as its tetragonal counterpart [50,53]. The lattice parameters of both polymorphs are presented in Table 2.1.

The electronic structure of $VO_2$ in both metallic and insulating phases was first described via band theory by Goodenough, who proposed that the MIT is caused by the lattice distortion [57], i.e. a Peierls transition. In particular, due to the octahedral crystal field, $3d$ orbitals of a $V^{4+}$ ion are split into higher energy $e_g$ states and lower energy $t_{2g}$ states, which are occupied by one electron (Fig. 2.3). In addition, the structure of $VO_2$ further lifts degeneracy of the $t_{2g}$ states, splitting them into $d_{||}$ and $\pi^*$ orbitals [49,50,57–59]. In the metallic $VO_2$(R) phase, the $d_{||}$ and $\pi^*$ bands overlap and contain electronic states at the Fermi level as shown in Fig. 2.2(b). In the insulating $VO_2$(M1) state, on the other hand, the V-V pair formation and their tilting induces an upwards shift of the $\pi^*$ band with respect to the Fermi level and a further splitting of the $d_{||}$ band into bonding-antibonding orbitals (Fig. 2.2(a)) [49,50,57,58].

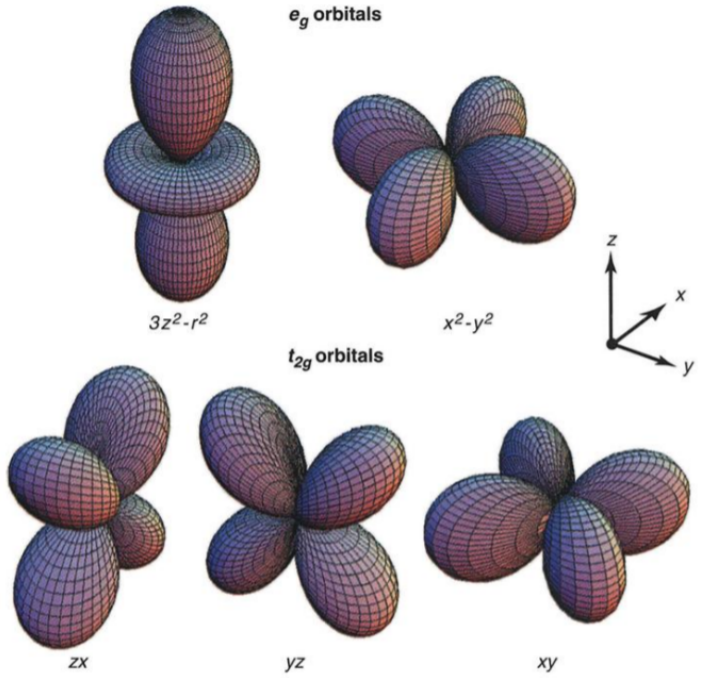


Figure 2.3: Splitting of the d orbitals in the cubic (octahedron type) crystal field. The $d_{x^2-y^2}$ and $d_{3z^2-r^2}$ orbitals pointing towards $O^{2-}$ ions have higher energy and form the $e_g$ band. The $d_{xy}$, $d_{yz}$ and $d_{zx}$ orbitals, on the other hand, point between the $O^{2-}$ ions and form the lower energy $t_{2g}$ band [60].

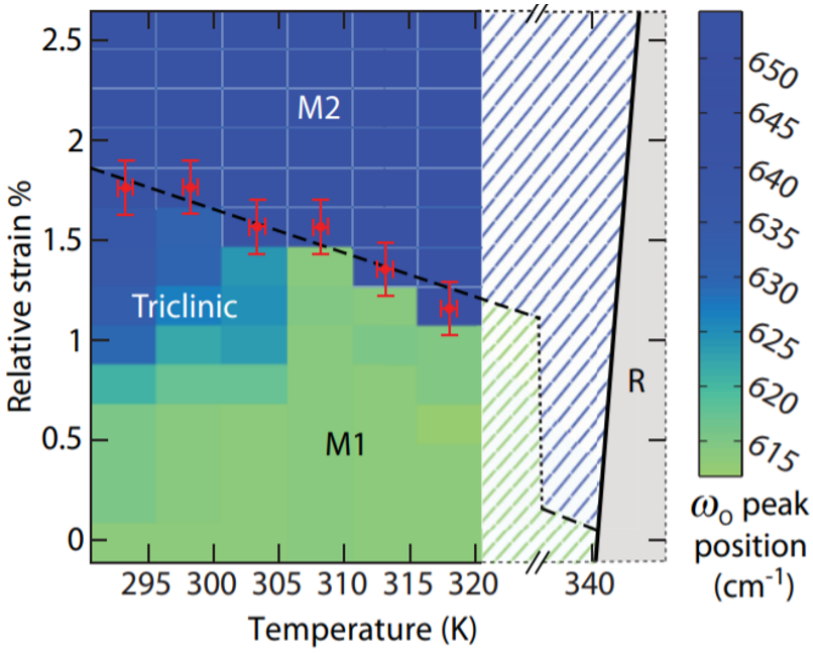


Figure 2.4: Strain-temperature phase diagram of insulating M1, M2 and triclinic (T) phases of $VO_2$. The structural changes in the material were tracked by the shift in its phonon frequency $\omega_0$ via Raman spectroscopy. The shaded region and the solid black line represent qualitative measurements, for which peak shift analysis was not sufficiently precise (adapted from [61]).

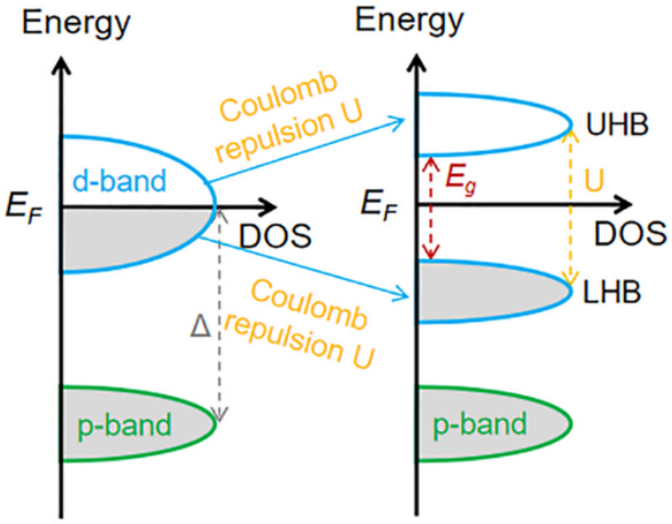


Figure 2.5: A schematic density of states (DOS) diagram of a generic Mott-Hubbard insulator representing light transition metal oxides. Here, Coulomb repulsion U causes the split of the $d$ band into upper and lower Hubbard bands (UHB and LHB respectively) [63].

Interpretation of the MIT in $VO_2$ via Peierls transition provides a qualitative description of the band gap opening in the monoclinic phase; however, it fails to provide a correct estimate of the band gap size, which reaches approximately 0.6 eV [50] according to experimental measurements. Furthermore, discovery of insulating monoclinic $VO_2$(M2) and triclinic $VO_2$(T) phases induced by temperature or strain (Fig. 2.4) further suggests that structural distortion may not be the only cause driving MIT in $VO_2$ [61]. Hence, in order to overcome inadequacies of the Peierls-type model for MIT, Zylbersztejn and Mott proposed a Mott-Hubbard model, where metal-to-insulator and phase transitions are initiated by strong electron-electron correlations rather than electron-lattice interactions [53, 62]. Here, calculations of the $VO_2$ band structure are carried out using an additional Hubbard correlation energy (U) term, which accounts for Coulomb repulsion between electrons. Zylbersztejn and Mott considered that in the metallic $VO_2$(R) phase electron correlations in the $d_{||}$ band are screened by the $\pi^*$ band; however, the extent of the screening in the insulating phase is reduced due to antiferromagnetic displacement of vanadium atoms perpendicular to the $c_r$ axis, which causes an upwards shift of the $\pi^*$ band [53, 62]. For this reason, the $d_{||}$ band splits into upper and lower Hubbard bands separated by a band gap $E_g$, as illustrated in Fig. 2.5. Nonetheless, extensive studies of MIT in $VO_2$ have shown that, just as Peierls transition, the Mott-Hubbard model alone does not provide an accurate description of physical properties, such as ground state magnetic and electronic features, for both insulating and metallic phases of the material [50].

Currently, electronic band structure calculations for $VO_2$, an example of which is shown in

Fig. 2.6, typically require both electron correlations and a monoclinic crystal structure for the insulating phase, but the debate whether either of the conditions is sufficient or necessary to open an insulating band gap still remains [50,53]. Hence, in order to achieve clarity on the nature of metal-to-insulator and crystallographic phase transitions, particular focus is nowadays placed on experimental studies of intermediate non-equilibrium phases of $VO_2$ and its response to different perturbations [53].

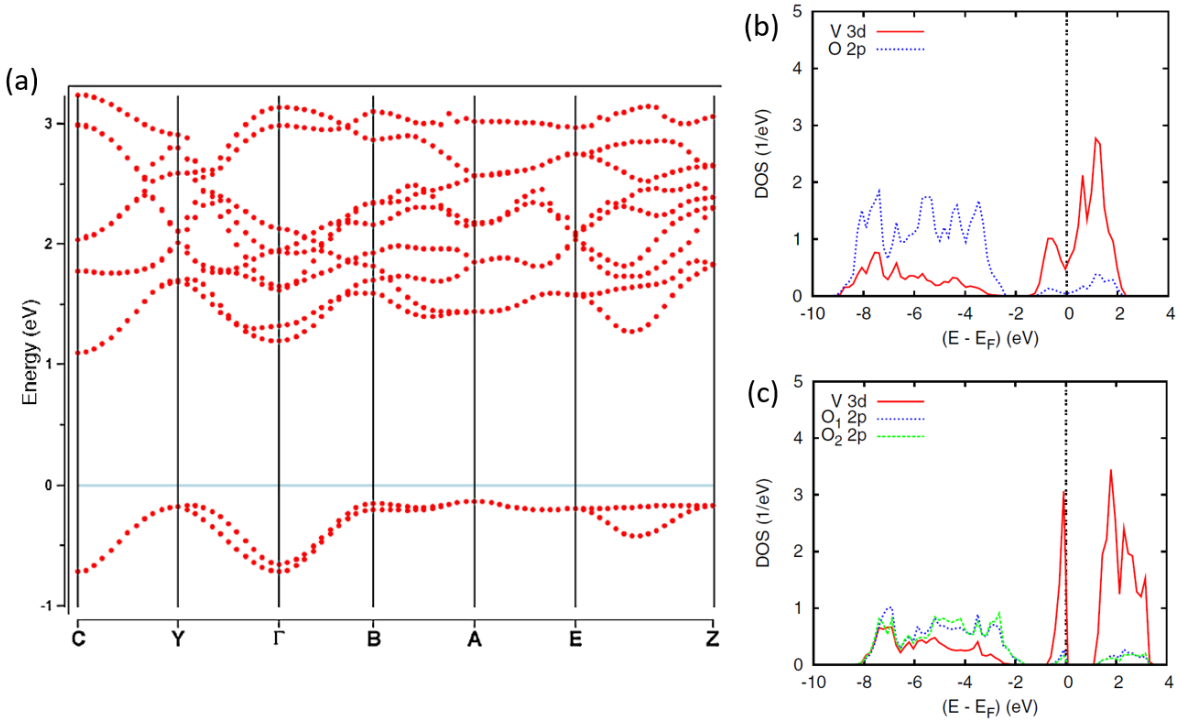


Figure 2.6: (a) Electronic band structure diagram for $VO_2$(M1) and partial DOS for both (b) $VO_2$(R) and (c) $VO_2$(M1) phases calculated using DFT with a hybrid HSE (Heyd, Scuseria, and Ernzerhof) functional [59].

### 2.1.2 Applications of $VO_2$

Ever since the discovery of MIT in $VO_2$, the material has attracted a lot of interest for potential applications in a variety of optical and electronic devices, such as field-effect transistors, sensors, switches, smart windows and memory devices. This section outlines only a few major $VO_2$-based devices, but a more thorough description of its application can be found in [64].

Along with the transition between metallic and insulating states, $VO_2$ also exhibits sharp changes in the infrared transmission. Together with modulation of the material via doping and construction of nanoarray structures or composite films, $VO_2$ shows promising characteristics to be used as an energy-saving thermochromic window coating [52,65]. In particular,

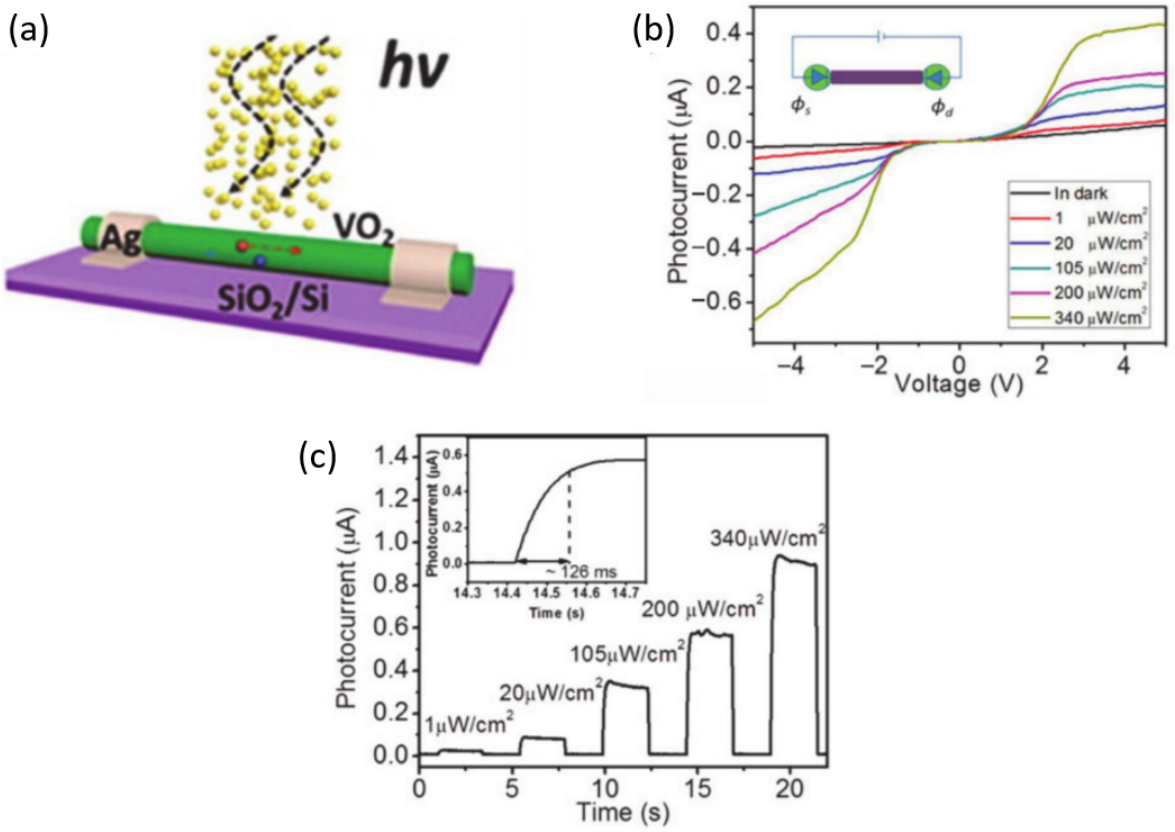


Figure 2.7: A diagram of a UV light detector made of $VO_2$ (a), I-V curves of the detector in the dark and under UV light of different intensities (b), photocurrent strength as a function of UV illumination intensities (c). The inset in (c) shows the device's response time which is approximately 126 ms (adapted from [52]).

$VO_2$-based coatings could transmit near-infrared radiation at ambient temperatures below the critical MIT temperature ($T_c$), while blocking it above $T_c$. However, optimisation of such coatings in terms of critical temperature, IR and luminous transmittance has been a challenging task and their commercial application has not been realised yet [52,65].

MIT in $VO_2$ can also be utilised in the development of optical switches and photodetectors [52]. For instance, it has been shown that $VO_2$ microwires undergo a photoinduced MIT in ultraviolet (UV) light [66] with responsivity several orders higher than that of graphene, $MoS_2$, GaS and GaSe [52,67]. A schematic of the $VO_2$ photodetector, its characteristic I-V curves and photocurrent measurements are shown in Fig. 2.7.

Furthermore, it has been recognised that $VO_2$ can be a promising alternative to silicon in field-effect transistors (FET), breaking the inherent size limitations of silicon-based FETs [52,68]. One of the major challenges associated with FET scaling are unscalable voltage supply, high leakage power and unsatisfactory current on/off ratios. These issues can be addressed by increasing the steepness of the sub-threshold current-voltage (I-V) slopes, which is limited to

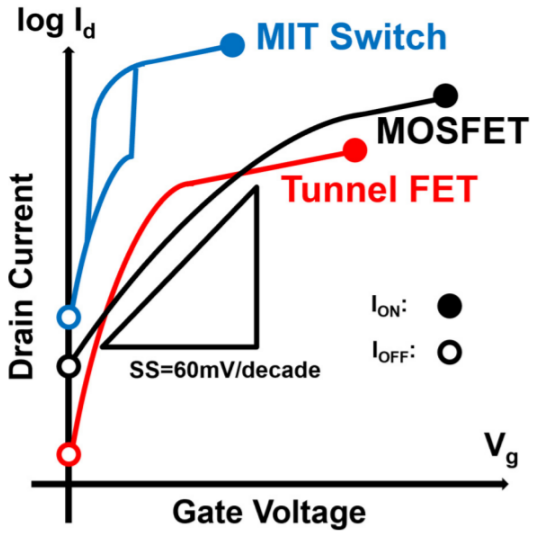


Figure 2.8: I-V curves for MIT FET, MOSFET and Tunnel FET [68].

approximately 60 mV/decade in current at room temperature in conventional metal-oxide-semiconductor FET (MOSFET). As shown in Fig. 2.8, which compares I-V curves for MOSFET, tunnel FET and MIT FET, the latter produces very steep sub-threshold I-V slopes of approximately 4 mV/decade in current; however, problems remain with the $VO_2$-based FET integration with other devices and general practicability due to hysteresis and significant DC offset voltage [68].

### 2.1.3 Compton scattering experiments in MIT materials and $VO_2$

Compton scattering experiments provide a versatile tool to study electronic structure in materials exhibiting metal-to-insulator transitions [69–72]. Such experiments are predominantly carried out in X-ray synchrotron facilities, which can support a wide range of experimental conditions (e.g. temperature, pressure) necessary for a MIT to occur. The resulting changes in the ground state electron momentum density distribution of a MIT material are frequently described by the difference of the Compton profiles measured on both sides of the transition point, as illustrated in Fig. 2.9. It shows Compton scattering data for $Rb_4C_{60}$, which undergoes a pressure-driven MIT at approximately 0.8 GPa [69]. Information on the symmetry of the electron orbital states can be further provided by taking Compton measurements along a number of crystallographic directions; they can then be used to reconstruct two-dimensional differential electron momentum density maps. An example of these anisotropies in $LaCoO_3$, which undergoes a spin-state change and a MIT at ≈500 K, is shown in Fig. 2.10. Even though Compton scattering experiments can provide an insight into the underlying MIT mechanism

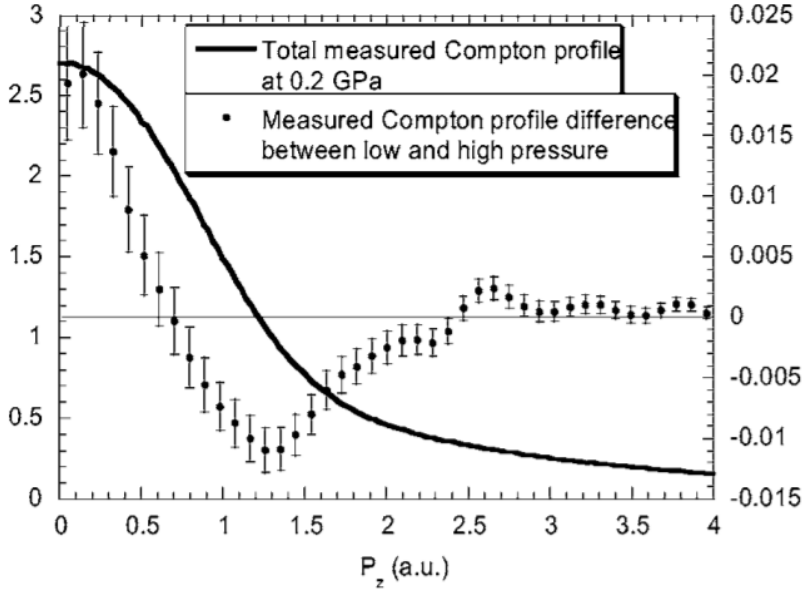


Figure 2.9: Total Compton profile of metallic $Rb_4C_{60}$ taken at 0.2 GPa is represented by the solid line (left scale).The difference profile between Compton profiles measured at low and high pressure (0.2 GPa and 2 GPa respectively) is marked by dots (right scale) [69].

and electronic behaviour of the material around the transition point, such measurements remain fairly rare.

As for $VO_2$, which is the target MIT material in this thesis, only a handful of Compton studies can be found in the literature [73–77]. The earliest theoretical calculation of Compton profiles for the high-temperature metallic phase dates back to 1976 [73]. The study, which was carried out using Hartree-Fock-Slater model and molecular-cluster approximations, predicted anisotropies of the order of 1% between a spherically averaged Compton profile and the profiles for [100] and [001] crystallographic directions. It was also speculated that a measurable difference of the Compton profiles can be obtained by comparing both high-temperature and low-temperature phases [73]. However, subsequent experimental measurements of isotropic Compton profiles of $VO_2$ using 59.54 keV gamma-rays found the aforementioned theoretical model to be incorrect, even though the measurements were taken for a low-temperature insulating phase [74].

Both theoretical and experimental Compton profiles for the low-temperature insulating $VO_2$(M1) phase were also studied in a relatively recent publication by Vashistha *et al* [75]. Here, spherically averaged Compton profiles were calculated using the DFT-LCAO (linear combination of atomic orbitals) method with Perdew-Burke-Ernzerhof (PBE) and Becke schemes to account for electron correlation and exchange respectively. Experimental Compton profiles for a polycrystalline $VO_2$(M1) sample were measured using an $^{241}$Am gamma radiation at 59.54 keV

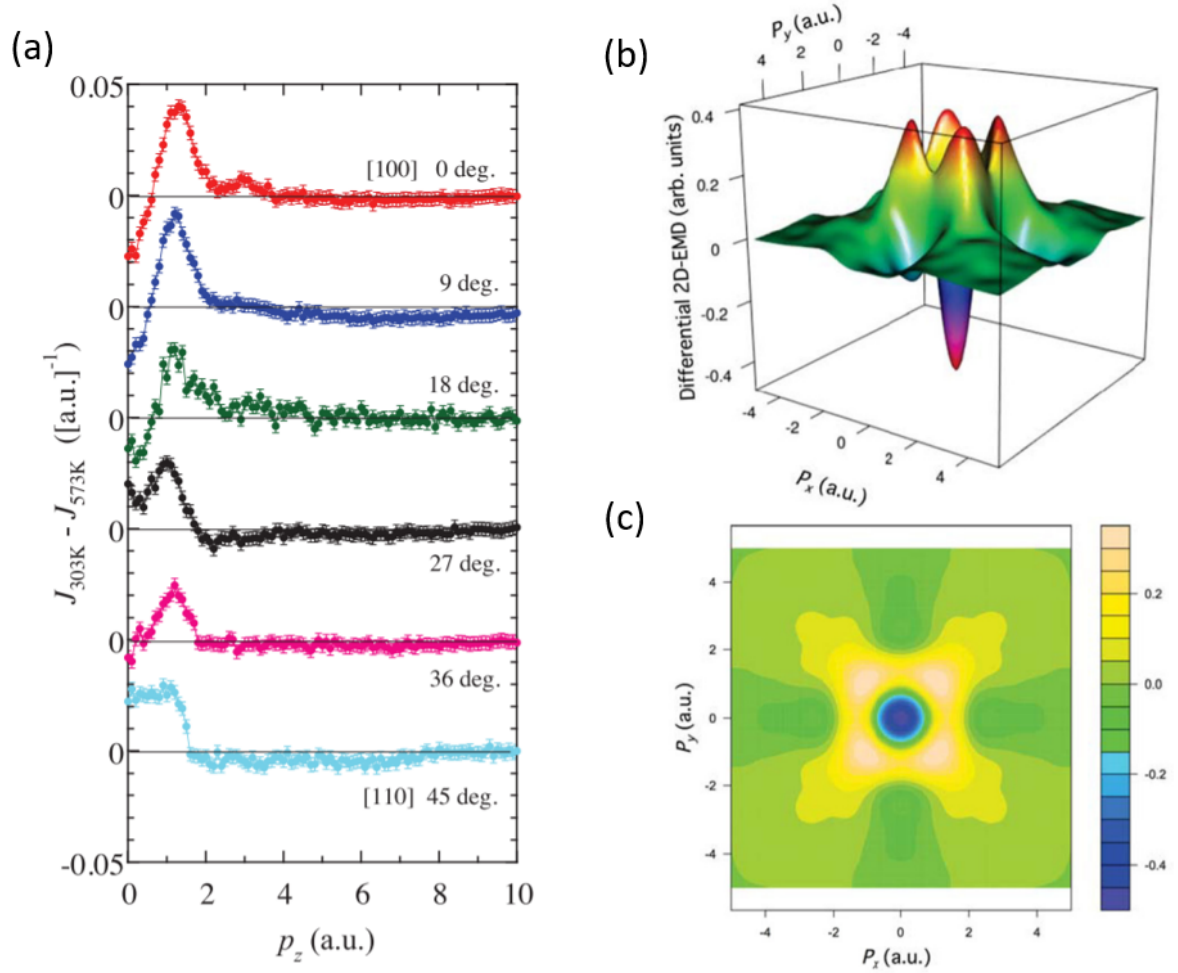


Figure 2.10: Difference Compton profiles in $LaCoO_3$ measured at 303 K and 573 K reflecting Co 3*d* electron orbital states (a). The measurements were taken for six directions spanning an angular range of 45 degrees between [100] and [110] crystallographic directions. A 3D view of differential 2D electron momentum density (b) and its contour plot (c) are reconstructed from the Compton profiles in (a)(adapted from [70]).

energy. Calculated and measured Compton profiles, as compared in Fig. 2.11, show a discrepancy in the projected electron momentum range between 0 a.u. and 3 a.u. The mismatch between the profiles is attributed to chemical bonding, which is typically underestimated within the DFT-LCAO scheme [75].

The first study of changes in electron momentum density across the MIT in $VO_2$ powder using both simulation and experiment was carried out by Ruotsalainen *et al.* in 2018 [76]. The group measured spherically averaged Compton profiles using X-ray synchrotron radiation at 87 keV energy, and compared the experimental data with a homogeneous electron gas (HEG) model and DFT calculations, where electron exchange and correlation for metallic and insulating $VO_2$ phases were treated using LSDA (local spin density approximation) and LSDA+U schemes respectively. Experimental results, as displayed in Fig. 2.12, show major

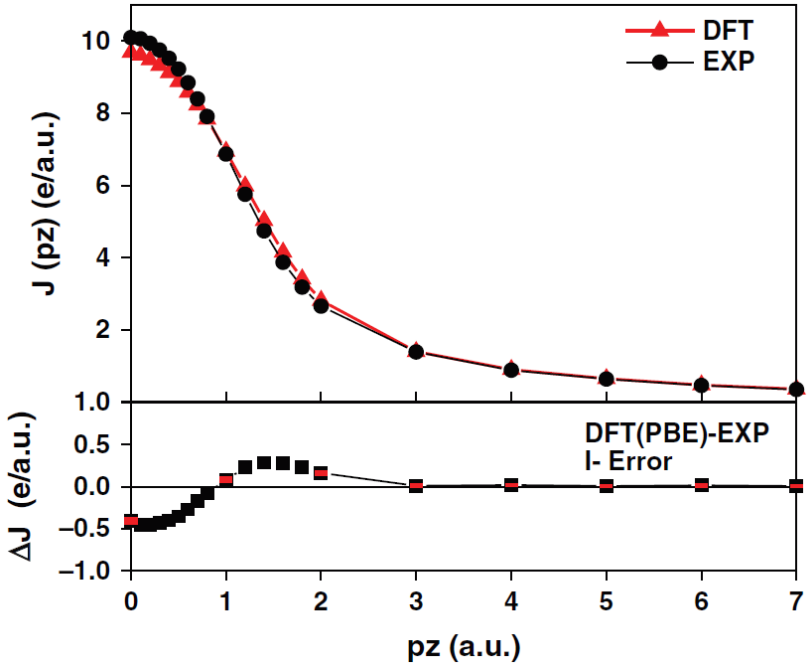


Figure 2.11: Theoretical and experimental Compton profiles for an insulating $VO_2$(M1) phase (upper panel) and the difference profile between the two (lower panel) [75].

fluctuations in difference Compton profiles in the $p_z$ range between -4 a.u. and 4 a.u., which indicates that the MIT in $VO_2$ affects only the valence electron states [76]. As expected, the measured data compares poorly with the HEG model, which is known to provide a poor description of valence electrons in oxide materials [76]. The DFT calculations, on the other hand, show a fairly good overall agreement with the experimental data, i.e. the calculations reproduce $p_z$ values for nodes, minima and maxima of most fluctuations in the difference Compton profile, but overestimates their absolute magnitude [76]. The differences between theory and experiment are assumed to arise due to errors in electron exchange and correlation effects, assumptions on the magnetic nature of the insulating $VO_2$ phase and neglect of thermal motion in the high temperature metallic $VO_2$ within DFT [76].

Theoretical calculations were further improved by Kylänpää *et al.*, who used both a quantum Monte Carlo (QMC) method and DFT (LDA+U) to simulate difference Compton profiles across the MIT in $VO_2$ [77]. The calculations were compared to experimental data obtained by Ruotsalainen *et al.* in Fig. 2.13. Expectedly, QMC calculations show a good agreement with the experimental data, within a multiplicative factor of x5 for the magnitude, due to a more accurate treatment of electronic correlations in QMC compared to DFT. The LDA+U approach in DFT also provides an improvement to the calculations made by Ruotsalainen *et al.* due to the optimisation of the Hubbard U term with QMC [77].

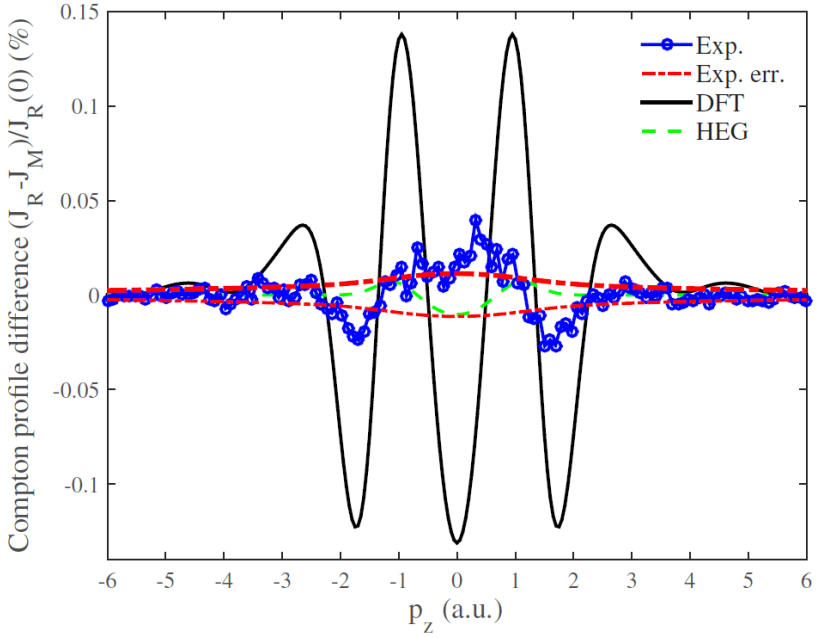


Figure 2.12: Comparison of experimental and theoretical Compton profiles for polycrystalline $VO_2$ across the MIT. The projected momentum densities $J_R$ and $J_M$ refer to metallic and insulating phases respectively [76].

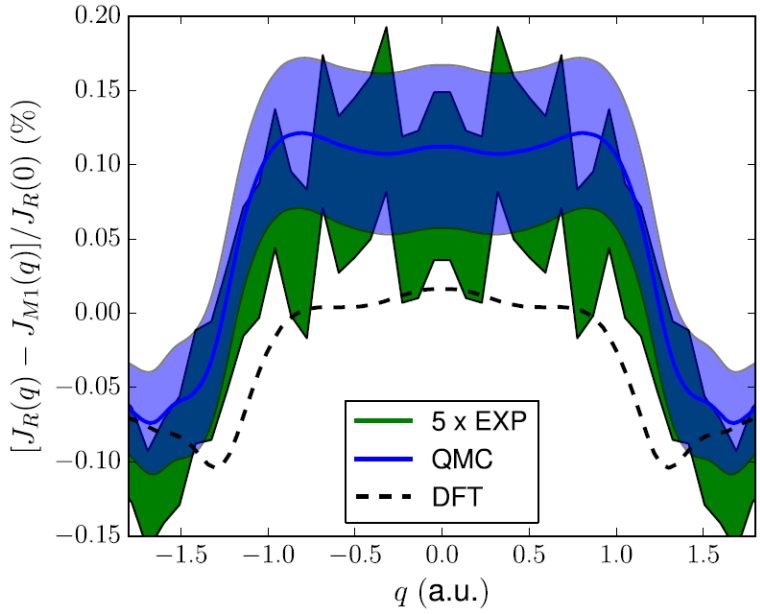


Figure 2.13: Comparison of experimental difference Compton profile (scaled) [76] and theoretical calculations within QMC (with $1\sigma$ statistical error) and DFT (LDA+U) frameworks [77].

## 2.2 Transition metal dichalcogenides (TMDs) and $WS_2$

### 2.2.1 Structure of TMDs

The existence of 2D materials such as graphene and monolayer TMDs was long doubted for their seeming violation of the Mermin-Wagner theorem, which states that at finite temperatures the long range order in 2D crystals would be broken by thermal vibrations [78]. Nonetheless, identification of a free-standing graphene sample by Novoselov and Geim [79] in 2004 showed that these materials can be stabilised by lateral rippling, which suppresses thermal vibrations that are otherwise expected in perfectly flat 2D structures [80]. This discovery initiated intensive research of the 2D material family, which now includes 2D allotropes of elements like phosphorus [81] and germanium [82], 2D ceramics (MXenes) [83], metal-organic frameworks [84] and polymers [85].

Amongst a wide range of 2D materials, monolayer TMDs have been recognised as one of the most attractive structures to study fundamental physical phenomena and develop new-generation electronic and optoelectronic devices (Sec. 2.2.2). As shown in Fig. 2.14, they are composed of three stacked atomic sub-layers X-M-X, where M is a group IV-VII, IX, X transition metal (e.g. Ti, Nb, W), and X is a chalcogen (e.g. S, Se). The elements in both M and X planes are bound by strong covalent M-X bonds, while the layers in bulk material are held together by weak van der Waals forces in various stacking orders [86]. Metal atoms in TMDs typically have either octahedral or trigonal prismatic coordination, which generates either tetragonal or hexagonal lattice symmetry respectively (Figs. 2.14(a) and 2.14(b)). In a monolayer TMD with a particular metal and chalcogen combination, only one of the given phases is thermodynamically stable [86]. Furthermore, the preferred metal coordination governs the splitting of its non-bonding d orbitals. As shown in Fig. 2.15, the latter are located in the gap between bonding and antibonding bands of covalent M-X bonds ($\sigma$ and $\sigma^*$ respectively). In TMDs with trigonal prismatic coordination, the d bands are split into three groups: $a_1$, e and e', corresponding to $d_{z^2}$, $d_{x^2-y^2,xy}$ and $d_{xz,yz}$ orbitals [86]. As for TMDs with octahedral coordination, two groups are formed: $e_g$ and $t_{2g}$ representing $d_{z^2,x^2-y^2}$ and $d_{yz,xz,xy}$ orbitals respectively [86]. Progressive filling of the d bands with electrons determines electronic character of the material, i.e. TMDs with filled bands are semiconducting, while those with half-filled bands are metallic. However, deviations from this picture occur due to unaccounted distortions in coordination of certain M-X combinations. The band structure of a TMD is further affected by chalcogen species but its impact is minor: heavier chalcogens tend to broaden the d bands, which in turn decreases the size of a band gap [86]. In $WS_2$,

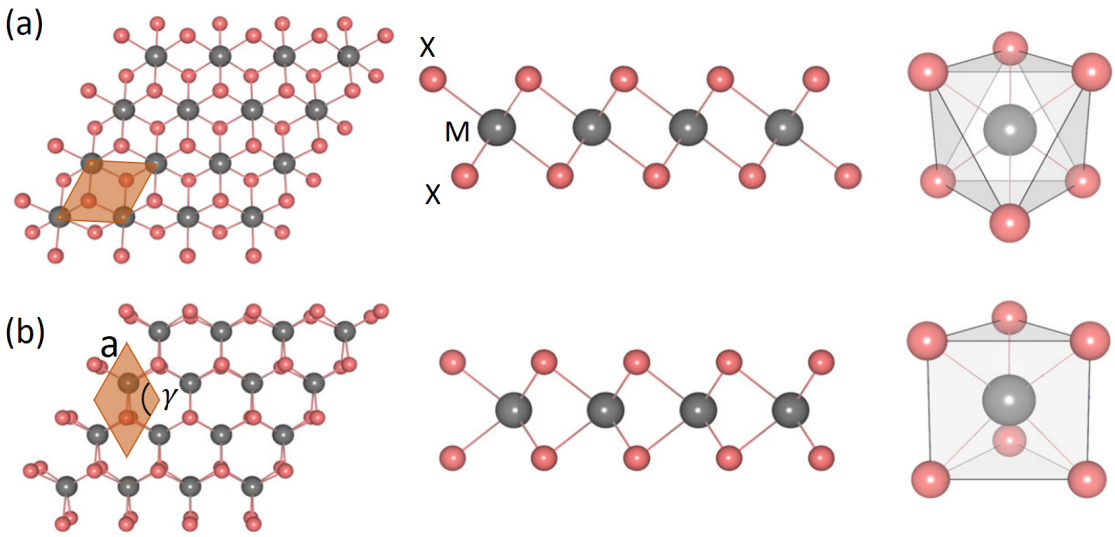


Figure 2.14: Top and side views of a generic TMD monolayer showing (a) tetragonal lattice symmetry generated by octahedrally coordinated transition metal atoms and (b) hexagonal lattice symmetry generated by trigonal-prismatically coordinated transition metal atoms. In the literature, these phases are referred to as 1T and 1H phases respectively. The shaded areas represent unit cells with a lattice parameter $a$. Image adapted from [87].

Table 2.2: Band gaps $E_g$ and hexagonal lattice parameters $a$ and $c$ for monolayer and bulk $WS_2$ [88, 89]. Markers T and E correspond to theoretical and experimental values respectively.

| Structure | $a$ (Å) | $c$ (Å) | $E_g$ (eV) |
|---|---|---|---|
| Monolayer $WS_2$ | 3.16 (T) | — | 2.05 (T) |
| Bulk $WS_2$ | 3.15 (E) | 12.32 (E) | 1.35 (E) |

which is one of the most widely studied TMDs, thermodynamically stable phase has trigonal prismatic metal coordination, hexagonal lattice and semiconducting character. The lattice parameters and the band gap size for both monolayer and bulk $WS_2$, are listed in Table 2.2.

Further prominent changes in electronic structure occur in semiconducting TMDs, which have similar band structures and undergo a transition from a direct band gap in a monolayer limit to an indirect gap in bulk material. These changes are captured in Fig. 2.16, which shows band structure diagrams for one to four layer $WS_2$. First principles calculations show that the bottom of the conduction band and the top of the valence band are energetically stable at the $K$ point with varying layer number, while the valence band near the $\Gamma$ point and the conduction band near the $Q$ point (which is located approximately in the middle between the $\Gamma$ and $K$ points) undergo significant changes. Specifically, the electronic states at the $K$ point are mostly associated with the $d_{x^2-y^2,xy,z^2}$ states of the transition metal and some mixture of p orbitals of the chalcogens, which are insensitive to interlayer coupling. The

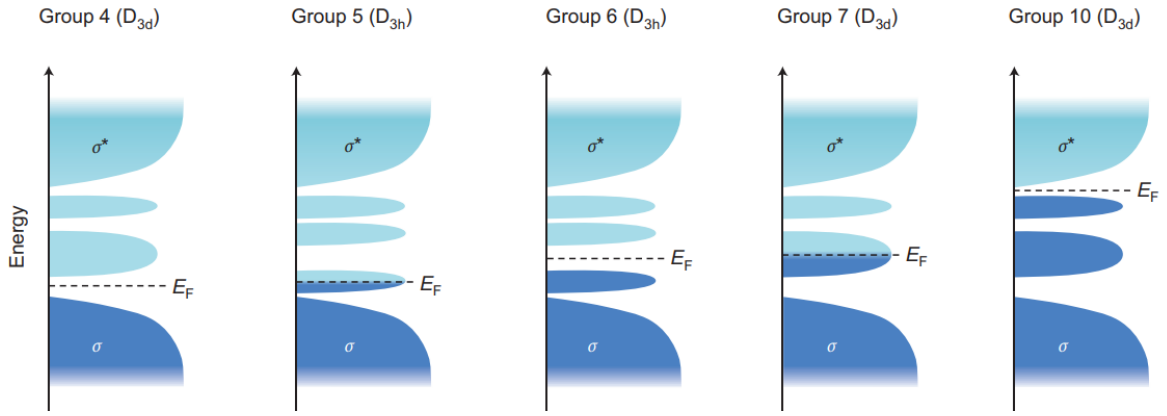


Figure 2.15: Qualitative picture of the d band filling in TMDs from groups IV-VII, X. The filled states are shown in dark blue and the empty ones are light blue. Trigonal prismatic and octahedral coordinations are denoted by $D_{3h}$ and $D_{3d}$ point group symmetries. TMDs with filled d bands and the Fermi level $E_F$ positioned in the band gap have a semiconducting character [86].

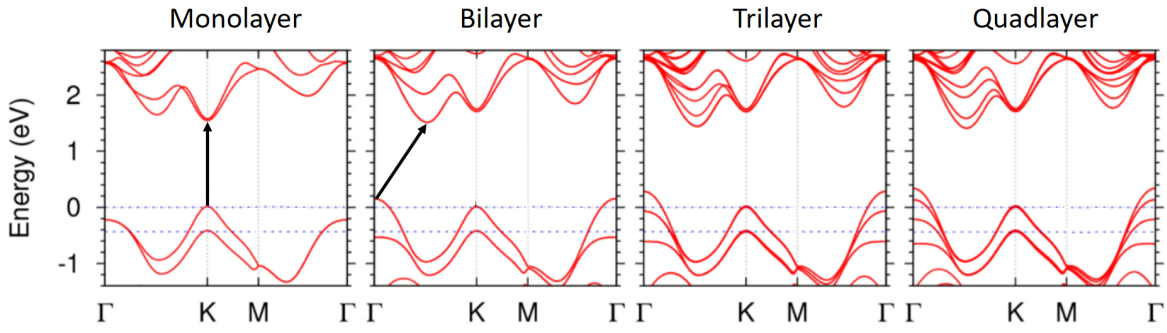


Figure 2.16: Electronic band structures of one to four layer $WS_2$ calculated via DFT (GGA). Note the valence band splitting at the $K$ point due to spin-orbit coupling in all of the structures. Image adapted from [90].

states near the Γ and $Q$ points, on the other hand, are influenced by contributions of the chalcogen $p_z$ orbitals. Close proximity between $p_z$ orbitals of neighbouring layers in ≥2 layer TMDs facilitates large electron interlayer hopping, which in turn alters band energies near the Γ and $Q$ points and causes the direct-indirect energy band gap transition. Experimentally these changes can be observed via PL spectroscopy, as shown in Fig. 2.17.

### 2.2.2 Applications of 2D transition metal dichalcogenides and $WS_2$

Unique physical and chemical properties of semiconducting TMDs have opened new prospects for the development of electronic and optical components in a wide variety of fields. Due to their tunable band gap, TMDs can be integrated into FETs and diodes, which can further be used in gas sensing, solar cells and LEDs [91]. Also, due to their exceptional mechanical properties, TMDs are able to withstand a high level of deformation, which is relevant in

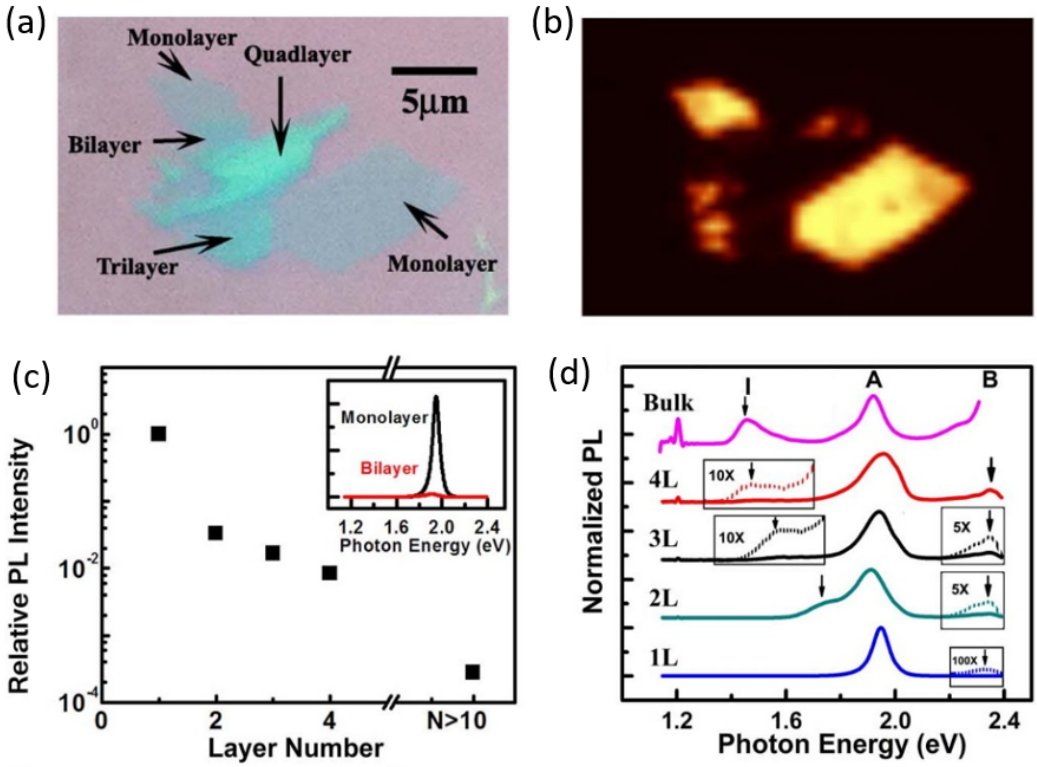


Figure 2.17: (a) An optical image of $WS_2$ flakes on a Si substrate with a $SiO_2$ cap-layer, (b) corresponding PL images excited at 2.41 eV, where only monolayers exhibiting a direct band gap are visible. (c) Relative PL intensity as a function of the $WS_2$ layer number. The inset in (c) shows PL spectra for monolayer and bilayer $WS_2$. (d) PL spectra of $WS_2$ (normalised with respect to the peak A). Peak I represents indirect band gap transitions, while peaks A and B represent direct-gap transitions between the conduction band and the split valence band at K points (see Fig. 2.16). Image adapted from [90].

the development of flexible electronic devices [91]. This section further outlines a number of interesting TMD applications, focusing mainly on $WS_2$ as an active material. A more detailed summary of TMD-based devices can be found in [92, 93].

2D TMDs have been recognised as convenient materials for implementation in memristors, i.e. electrical devices with programmable resistance that retain the history of their state [94]. They mimic basic biological functions of synapses and therefore can be used for neuromorphic computing and development of artificial intelligence. The standard operational mechanisms employed in memristors typically require large operating currents, which are incompatible with low-power consumption goals[1] [94, 95]. However, it has been shown that a memristor incorporating $WS_2$ required low program current of 1 μA in the ON state, displayed fast switching times of 13-14 ns and successfully replicated synaptic functions [95].

[1] Powerful computers, which can be used for pattern recognition, can consume ≈1 MW of electricity compared to ≈20 W needed to power the human brain [95].

Another promising field for 2D TMD integration is quantum photonics, where it could be used to make single-photon emitters. These light sources are central to next-generation quantum communications, information and computing technologies, and ideally produce indistinguishable single photons at high generation and extraction efficiencies [96,97]. An example of a quantum emitter based on a monolayer $WS_2$ flake deposited on top of a silica nanopillar array of 170 nm in height is shown in Fig. 2.18(a). The spectra representing PL intensity at the location of a nanopillar and away from it are depicted in panels 2 and 1 respectively in Fig. 2.18(b), while panel 3 shows a PL intensity spectrum of a $WS_2$ monolayer deposited on 190 nm nanopillars. Multiple lines in the PL spectra suggest that the nanopillar sites facilitate emission of a number of different photons; however, their spread is reduced at higher pillar sites, leading to a higher probability of the desired single-photon emission per site [96].

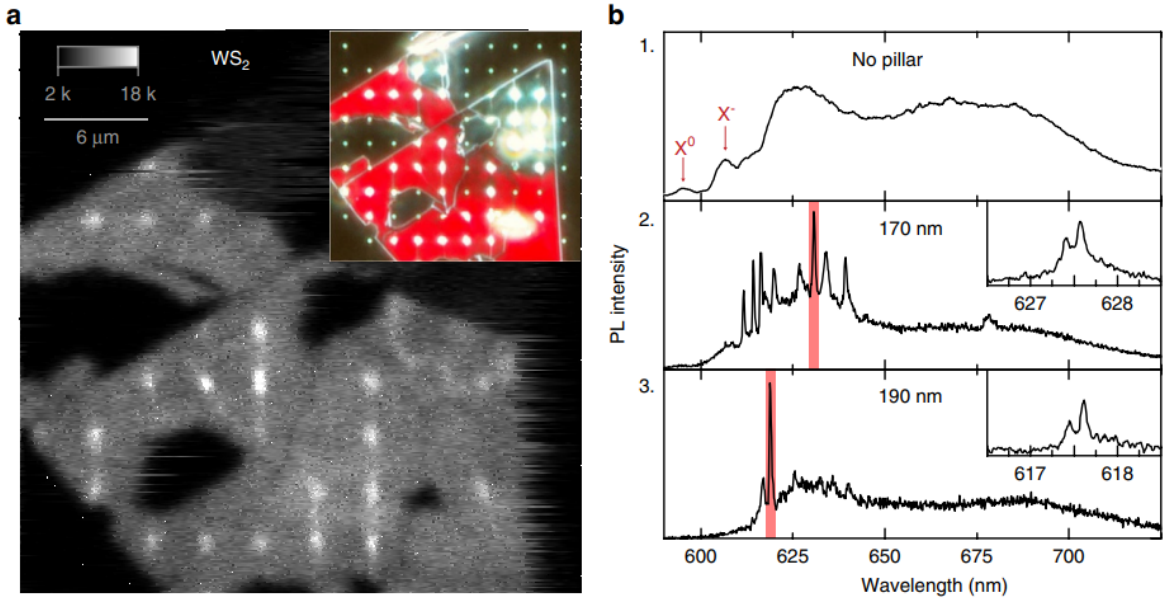


Figure 2.18: Quantum emitter array using monolayer $WS_2$ as an active material. (a) Shows an integrated PL intensity raster scan of the flake measured at 10 K. The bright spots correspond to unpierced nanopillar sites and the inset shows a dark-field optical micrograph of the same area. (b) Shows the PL spectra measured at a location away from a nanopillar and nanopillar sites . Note the $X^0$ and $X^-$ peaks as well as the broad emission band measured at a flat $WS_2$ site, which appear due to unbound, weakly localised or defect-related exitons. Image adapted from [96].

Structural characteristics of monolayer TMDs and other 2D materials also allow for the assembly of heterostructures – stacks of multiple 2D materials held together by van der Waals forces. Mechanical, electronic and optical properties of these assemblies differ from the properties of the constituent layers and hence assist the development of practical applications [98,99]. One of the device classes in which heterostructures are found particularly useful is photodetectors. While individual 2D materials frequently have either slow response time or unsat-

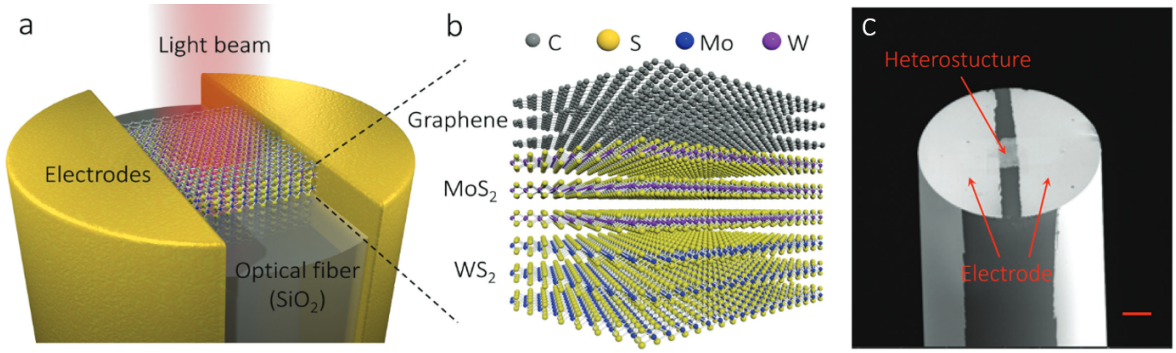


Figure 2.19: Heterostructure-based photodector integrated into an optical fibre. Schematic representations of the device and the heterostructure are shown in (a) and (b) respectively. (c) Shows a scanning electron micrograph of the device, where the scale bar represents 20 µm. Image adapted from [100].

isfactory responsivity for photodetection, these issues can be overcome by an appropriate heterostructure design, where a built-in electric field at layer interfaces facilitates effective electron-hole pair separation and therefore improves photodetection properties [100]. An example of a heterostructure-based photodetector is shown in Fig. 2.19. It consists of a multilayer graphene–$MoS_2$–$WS_2$ assembly integrated into an optical fibre with gold electrodes, which concentrates all the input power onto the heterostructure.

### 2.2.3 Compton scattering experiments in transition metal dichalcogenides

Layered transition metal dichalcogenides provide an interesting system to study via Compton scattering. In theory, the technique can capture interlayer coupling and electronic changes associated with an indirect-to-direct band gap transition in materials like $WS_2$ and $MoS_2$. So far, a thorough study tracking these changes in TMDs has not been carried out; however, there are a number of Compton scattering studies investigating bulk TMDs such as $WS_2$ [101], $WSe_2$ [101], $WTe_2$ [102] and $FeS_2$ [103]. Interestingly, in these experiments Compton scattering data is used to test the performance of Hartree-Fock (HF) calculations and various electron exchange and correlation functionals within DFT. Hence, the data is presented predominantly as difference profiles between theoretical and experimental Compton profiles, as shown in Fig. 2.20. Analogous measurements were also carried out on doped TMDs such as $TaS_{0.5}Se_{1.5}$ [104] and $Cr_{0.5}X_{0.5}Se_2$ (X=Mo, W) [2], and a mixed TMD MoTeSe [105]. Note that all the outlined experiments involve TMD irradiation with gamma rays either from $^{137}$Cs or $^{241}$Am sources.

In the context of a broader class of 2D materials, Compton scattering experiments have been carried out so far only on few-layer graphene [35]. An important feature of these experiments

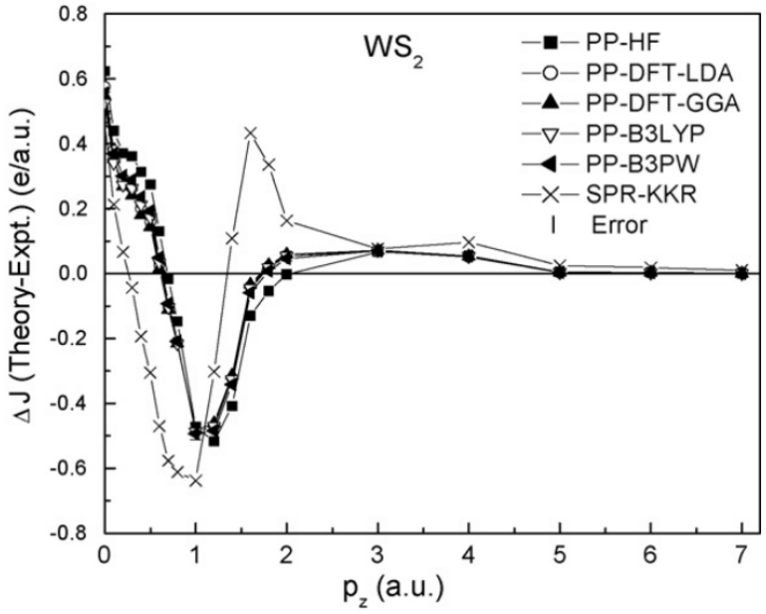


Figure 2.20: Isotropic difference Compton profiles for polycrystalline $WS_2$ comparing various theoretical models and experimental data (image adapted from [101]). Theoretical calculations were carried out within pseudopotential (PP) HF, DFT and their hybrid schemes (B3LYP, B3PW), as well as using a spin polarised relativistic Korringa–Kohn–Rostoker (SPR-KKR) method. Experimental data was obtained using a $^{137}$Cs gamma ray source at 661.65 keV energy. Substantial differences between experimental and theoretical Compton profiles in the low momentum region are attributed to the limitations of theoretical models in predicting electron momentum densities [101].

is that they were conducted using a 120 keV electron beam in TEM as a source of radiation, as opposed to X-ray or gamma radiation in experiments on TMDs and MIT materials described in section 2.1.3. Furthermore, the study also compares the Compton profile for few-layer graphene with the one for graphite, as illustrated in Fig. 2.21. It was concluded that the electron density is more delocalised in graphene compared to bulk graphite.

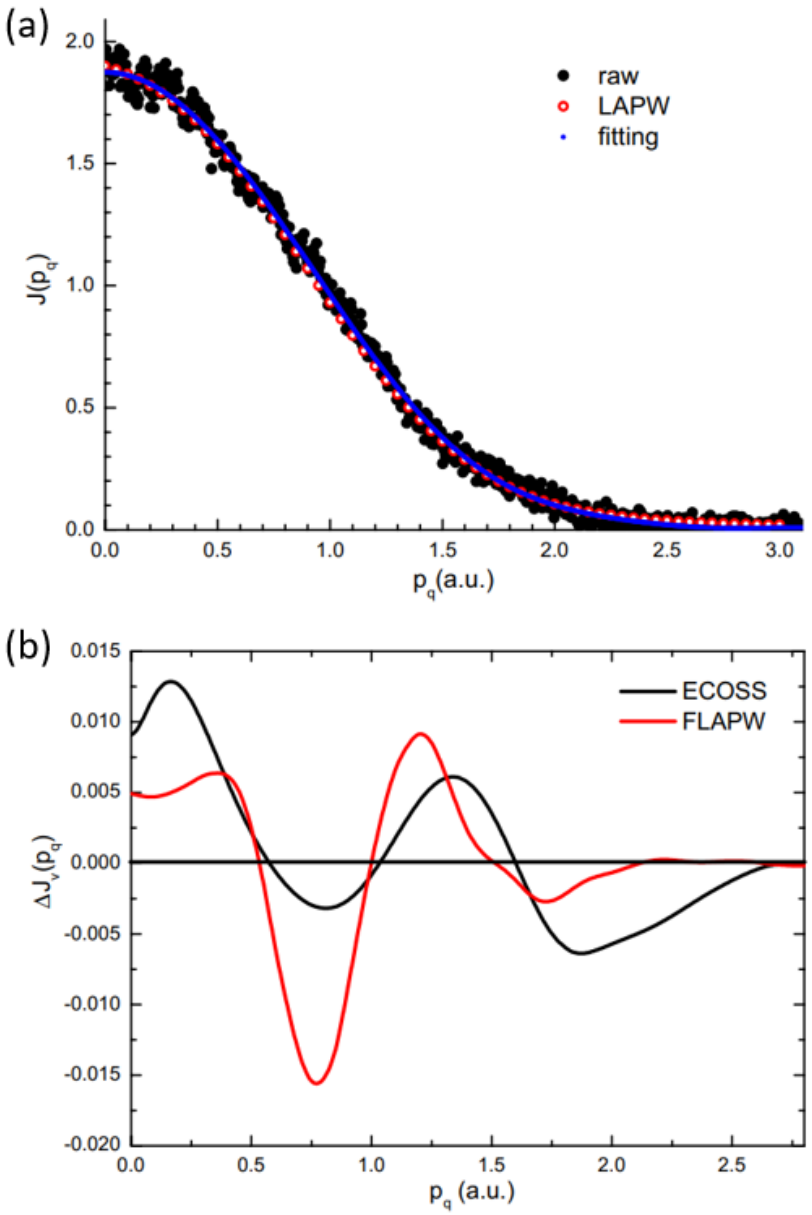


Figure 2.21: (a) Experimental electron Compton profile of valence electrons in few-layer graphene (in black). A polynomial fitting to the data is shown in blue and a theoretical profile calculated via full-potential linearized augmented plane wave (FLAPW) approach in DFT is shown in red. (b) Comparison of theoretical and experimental difference Compton profiles of valence electrons $\Delta J_{\mathrm{v}}(p_q) = J_{\mathrm{v}}^{\mathrm{graphene}}(p_q) - J_{\mathrm{v}}^{\mathrm{graphite}}(p_q)$ (ECOSS stands for electron Compton scattering from solids) [35].

# Chapter 3

# Experimental techniques

Electron Compton scattering experiments presented in this thesis involve two major experimental techniques – transmission electron microscopy (TEM) and electron energy loss spectroscopy (EELS). Hence, this chapter outlines the main principles underpinning the operation of a transmission electron microscope, including electron-matter interactions, microscope structure, operational modes and instrumental limitations. The chapter also briefly overviews scanning transmission electron microscopy – a technique that incorporates features of scanning electron microscopy into the standard TEM operation. Lastly, it discusses EELS, which is key in detection and measurement of inelastically scattered electrons.

## 3.1 Transmission electron microscopy

The ideas behind electron microscopy emerged in early 20th century, not long after de Broglie proposed that all matter exhibited wave-like behaviour [106]. Due to wavelengths of electrons, which can be five orders of magnitude smaller than those of visible light photons, electron microscopes surpassed the resolution limits of optical microscopes. In combination with diffraction and spectroscopic techniques, electron microscopes are nowadays one of the most versatile tools used to study materials on an atomic scale.

As electrons couple strongly to matter, interactions between the electron beam and a specimen produce a variety of secondary signals, summarised in Fig. 3.1. In transmission electron microscopes, which use a high-energy (e.g., 200 keV) electron beam to penetrate a thin sample, both elastically and inelastically scattered electrons can be used to obtain information characterising crystal structure [107], orientation [108], defects [109] and strain [110]. Inelastically scattered electrons can further provide information about dielectric response [111] of the

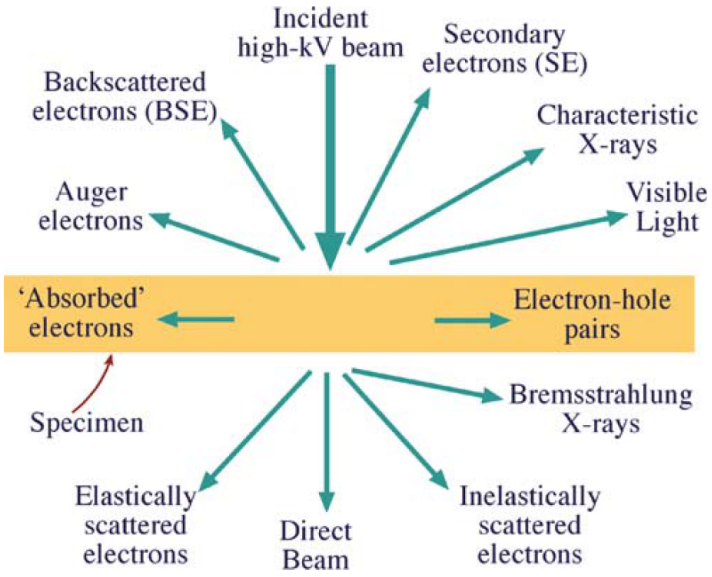


Figure 3.1: Secondary signals arising from interactions between an electron beam and a specimen [106].

material, electronic structure and bonding [112] of constituent atoms. The ionising interactions between the beam and the sample can also generate characteristic X-rays and Auger electrons, which may be used to derive quantitative information about sample elemental composition [106].

Despite a vast amount of information that can be obtained via TEM, the technique is limited by a number of factors. In order to be able to record any transmitted electron signal, the samples typically have to be under 100 nm in thickness. Therefore, bulk specimens are thinned down using, for instance, ion milling [113] which can introduce structural and chemical changes in the sample and leave unwanted artefacts in the TEM data [106]. Further complications may arise due to electron beam damage: higher resolution and signal-to-noise ratio typically require higher electron dose and acceleration voltage, which can be detrimental to sensitive samples such as 2D materials [114]. Higher resolution also implies that only very small sections of a sample can be studied, making TEM a poor sampling tool [106].

### 3.1.1 TEM structure and operation

One of the most important parts of a TEM is the electron source, which produces a nearly monochromatic and partially coherent electron beam (Fig. 3.2). There are two main types of electron sources: thermionic and field-emission electron guns. Each of these has a different energy spread, lifetime, current stability and brightness [106]. Field-emission guns are the

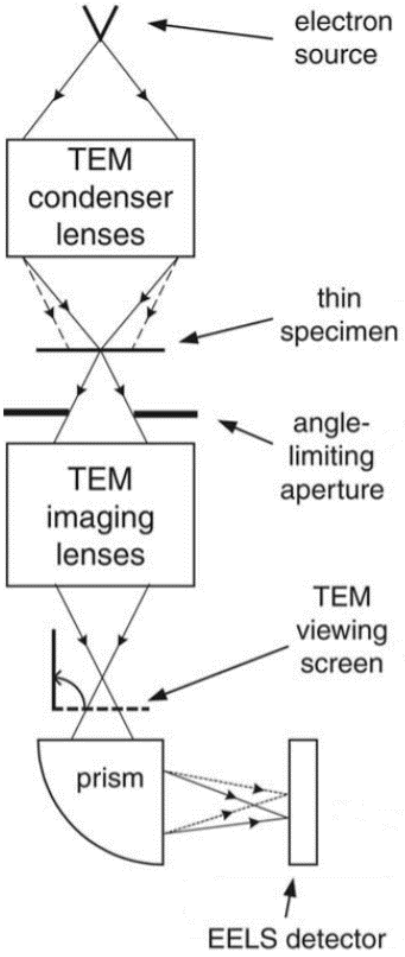


Figure 3.2: Structure of a TEM equipped with an electron energy loss spectrometer [115].

best electron sources and produce a beam originating from (thermally assisted) electrons tunnelling out of a fine tungsten needle in the presence of an electric field (Fig. 3.3). As the electron beam is emitted from a large area, electromagnetic condenser lenses are used to demagnify the source size and control illumination on the sample (i.e., focused or parallel beam). The strongest and the most important lens in a TEM is the objective lens, which, together with intermediate and projector lenses (the three are denoted as imaging lenses in Fig. 3.2), create and magnify diffraction patterns and images of a sample. These are then projected on either a phosphor screen or a camera, or directed to spectrometers such as an electron energy loss spectrometer for further analysis.

However, the electromagnetic lens system in a TEM is not perfect and limits the maximum resolution of the microscope. The most relevant aberrations within the experimental framework of this thesis are diffraction and spherical aberrations. The former originates from the wave nature of electrons and a finite size of the objective lens aperture, due to which the

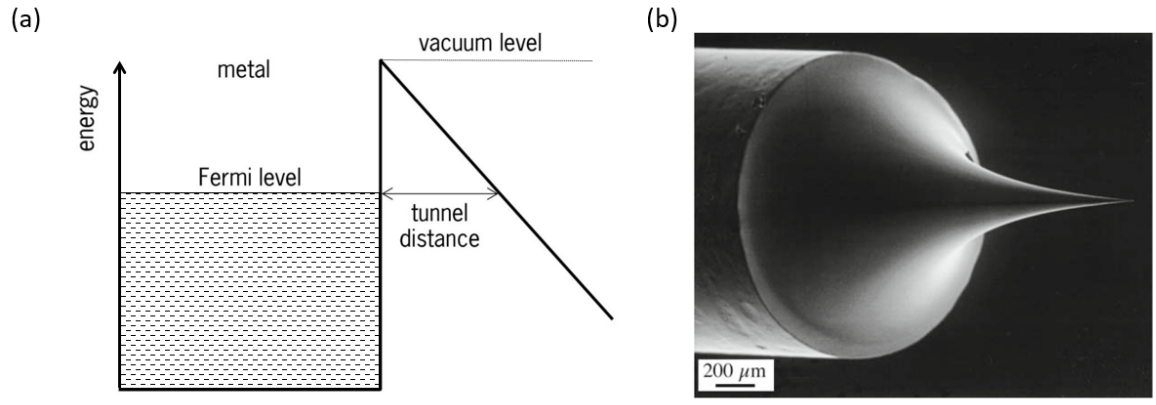


Figure 3.3: (a) shows energy levels in a FEG at 0 K. In the presence of a strong electric field, the vacuum level band is bent, allowing electron tunneling thought the potential barrier. (b) shows a tungsten FEG tip [106].

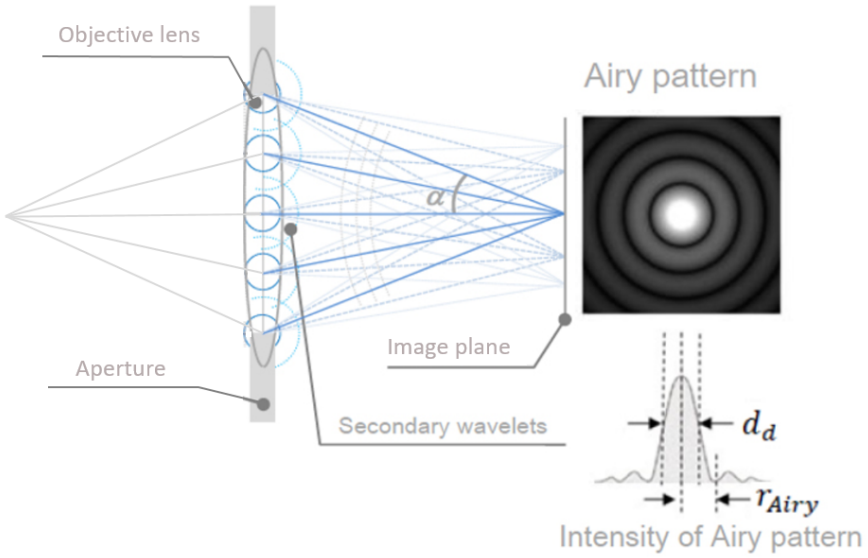


Figure 3.4: As the electron beam diffracts from the objective lens aperture, its propagation can be thought of in terms of spherical wavelets which interfere with each other. The figure shows the wavelets that interfere constructively and create an Airy pattern on the image plane of the objective lens, which defines the fundamental resolution of a TEM (adapted from [116]).

electron beam spreads as secondary Huygens wavelets and a point object has the profile of an Airy disc. (Fig. 3.4). In order to reduce the effects of diffraction aberration, one could increase the size of the objective lens aperture; however, that would increase spherical aberration ($C_s$) - a defect resulting from radial inhomogeneities in the magnetic field of the lens. As shown in Fig. 3.5, differences in the magnetic field change the extent of electron deflection, such that higher angle rays are more strongly focused, causing point objects to be imaged as

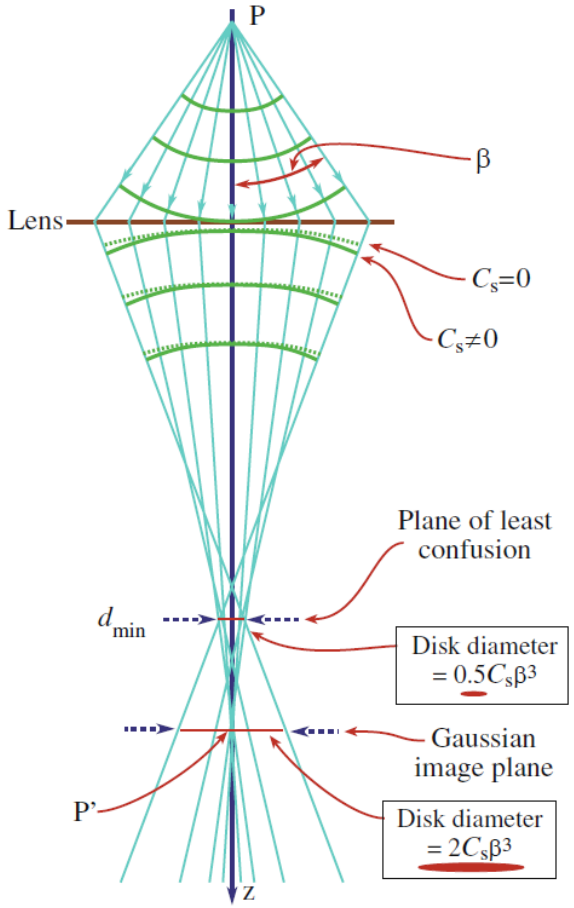


Figure 3.5: Schematic representation of spherical aberration in an electromagnetic lens [106].

discs. [106]. While the highest attainable resolution (information limit) of a $C_s$-limited TEM is approximately 1 Å, sub-Å resolution can be achieved using $C_s$ correctors implemented in the most advanced TEMs.

### 3.1.2 TEM operation modes

Versatility of a TEM in detailed analysis of materials partially originates from a number of modes the instrument can operate in. One of its major advantages is accessibility of both real-space images and diffraction patterns of a sample. The switching between imaging and diffraction modes is controlled by changing the strength of an intermediate lens, as shown in Fig. 3.6. In the imaging mode, the object plane for the intermediate lens is set to the image plane on the objective lens, while in the diffraction mode the object plane is adjusted to the back focal plane of the objective lens [106].

The imaging mode can be divided into two sub-modes - bright field and dark field imaging. The bright field mode uses an objective aperture to select a transmitted beam to form an

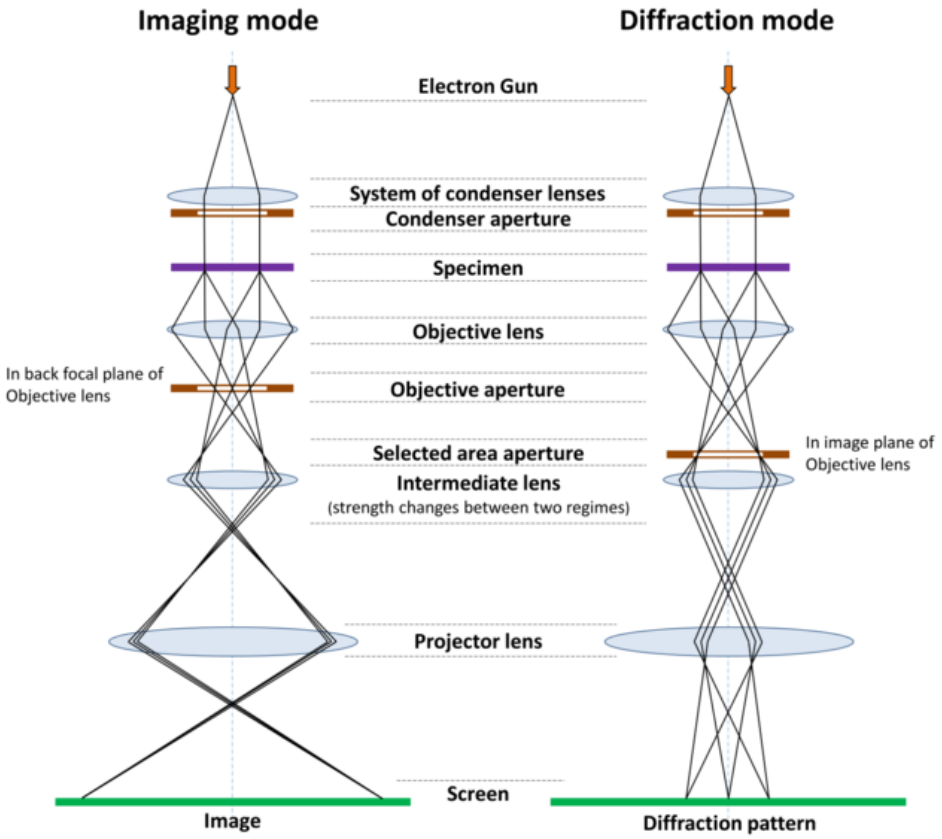


Figure 3.6: Electron ray path diagram in imaging and diffraction modes in TEM [117].

image, as shown in Fig. 3.7(a). In this case, electrons scattered by the sample are blocked,

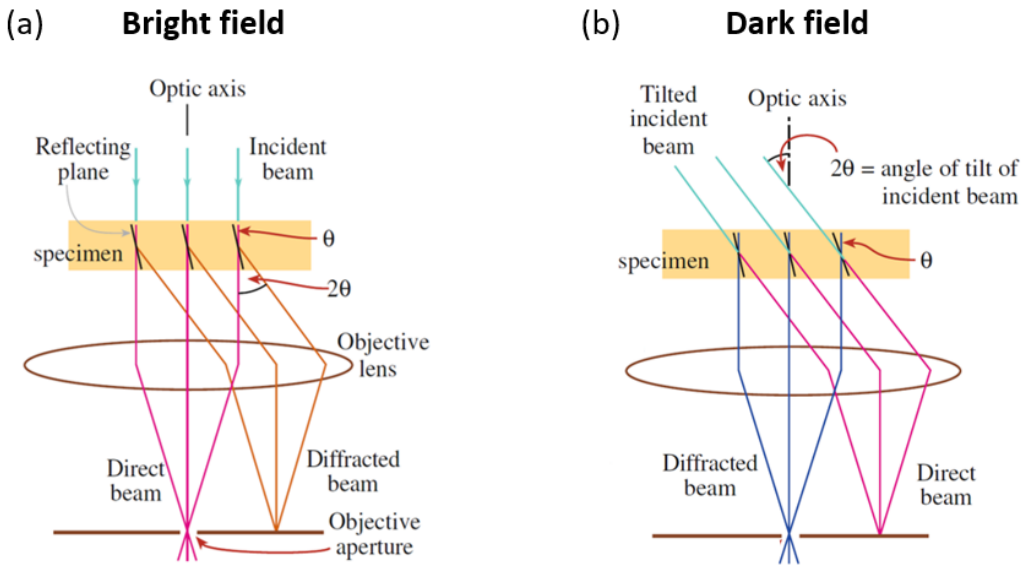


Figure 3.7: Electron ray path diagrams representing a bright field imaging mode which uses a transmitted electron beam, (a), and a dark field imaging mode which uses a scattered beam, (b) [106].

and the sample appears dark with respect to vacuum. In the dark field mode, the primary electron beam is tilted, and the scattered beam is selected for imaging (Fig. 3.7(b)). As a result, the sample in the image appears light in comparison to dark vacuum. Furthermore, the dark field mode can also be used to carry out momentum resolved spectroscopic energy measurements of the scattered beam. For instance, by controlling the beam tilt angle one can detect Compton scattered electrons, which are in the focus of this thesis.

In combination with electron images, one can further obtain diffraction patterns, which convey crystallographic information about the sample (for instance lattice parameter, grain orientation and defects). The symmetry of the pattern, i.e. positions of particular diffracted spots and potential systematic absence thereof, reveals the structure and orientation of the unit cells comprising the material. The intensity of individual spots for weak, kinematic scattering is described by the square modulus of the structure factor, $|F_{hkl}|^2$, where the structure factor coherently sums the electron waves scattered by every atom within a given unit cell. It is defined as:

$$F_{hkl} = \sum_i f_i \exp\left[2\pi i(hu_i + kv_i + lw_i)\right], \tag{3.1.1}$$

where $f_i$ denotes an atomic scattering factor of the $i^{th}$ atom, which is located at a position $(u_i, v_i, w_i)$ within the unit cell, and terms $h$, $k$, $l$ are the Miller indices of the (hkl) planes involved in scattering. Note that the exponential term in equation 3.1.1 takes into account the phase difference between electrons scattered by different but parallel (hkl) planes and determines the conditions under which the scattering amplitude is zero.

Despite the benefits of describing diffraction in terms of the structure factor, a more common approach to it is the well-known Bragg's law, which describes the conditions under which the electron beams diffracted by parallel (hkl) planes interfere constructively, i.e.:

$$2d_{hkl}\sin\theta = n\lambda, \tag{3.1.2}$$

where $d_{hkl}$ is the interplanar distance between (hkl) planes, $\theta$ is the Bragg angle, $\lambda$ is the wavelength of electrons and $n$ is the order of reflection, which is typically set to 1.

The details on how the mentioned operational modes are used to set up particular experiments are presented in Chapter 4.

### 3.1.3 Scanning transmission electron microscopy (STEM)

Despite significant technological improvements in aberration correction in conventional TEM and its capacity to transfer information on sub-Å level, scanning TEM (STEM) has emerged

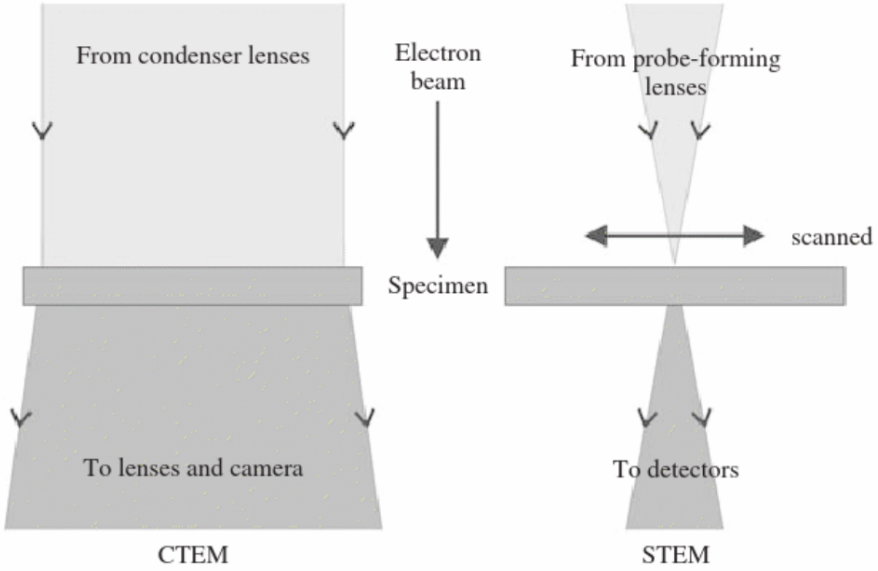


Figure 3.8: Electron probe and imaging differences between TEM (denoted as CTEM in the image) and STEM [121].

as the preferred technique in sample characterisation on an atomic scale. Its advantages over TEM include imaging modes that are more straightforward to interpret and a possibility to use multiple detectors at the same time [118,119]. While standard measurements in TEM employ a wide, nearly parallel electron beam to illuminate the sample, STEM operates by rastering a highly convergent electron probe across the specimen (Fig. 3.8). A simplified diagram of STEM electron optics is presented in Fig. 3.9. Here, the condenser and objective lenses demagnify the electron source and focus the beam to a spot, the size of which can be made smaller than the size of atoms in a specimen using aberration correction [120]. The motion of the probe across the sample is controlled by scan coils. Moreover, unlike in TEM, image formation in STEM does not require any post-specimen electromagnetic lenses.

STEM can operate in both bright field and annular dark field modes. Bright field images are formed by a detector positioned along the optic axis, which detects the low-angle scattered electrons. STEM and TEM bright field images are related through the principle of reciprocity [120]. However, the most widely used imaging mode in STEM is the annular dark-field mode, which uses electrons scattered at high angles to provide atomic number (Z) contrast images. One of the major advantages of this mode is direct correspondence between the obtained image and atomic sample structure, which is not always achieved in high resolution TEM or bright field STEM images. Furthermore, the annular dark field mode also accommodates simultaneous measurements of inelastically scattered electron using EELS.

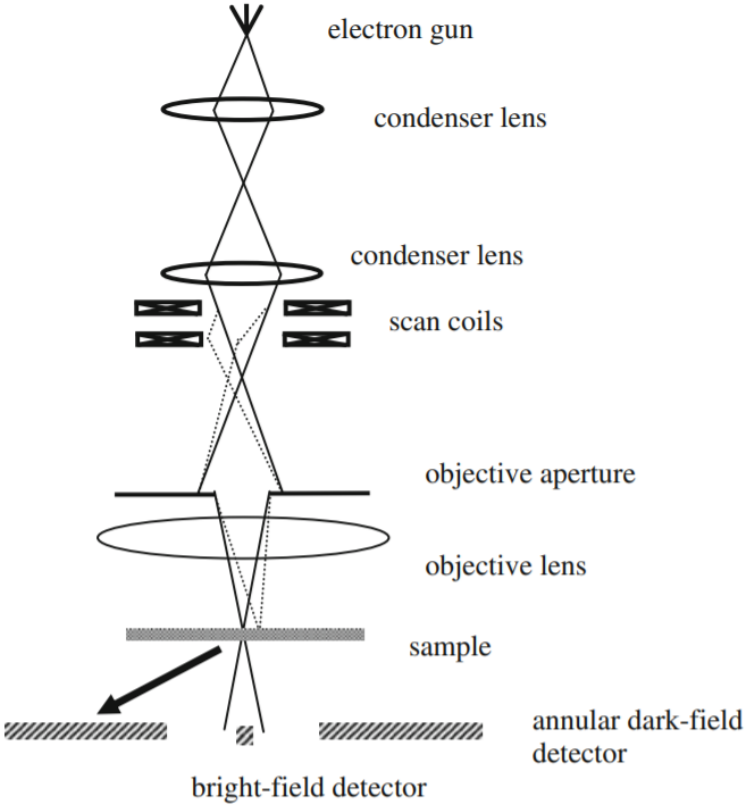


Figure 3.9: Electron optics of STEM. An electron beam produced by an electron gun is focused to a fine spot by condenser and objective lenses. The probe is further rastered across a specimen using scanning coils [120].

Due to rotational symmetry of the probe-forming electromagnetic lenses, resolution of STEM images is mostly limited by spherical aberration. Hence, a lot of effort has been placed into its correction by breaking the rotational symmetry via introduction of magnetic multipole elements such as quadrupole and octupole lenses displayed in Fig. 3.10 [122]. The aberration correcting element in STEM typically consists of a series of quadrupoles and octupoles in order to produce a beam with negative spherical aberration, which counteracts the positive spherical aberration of the objective lens (Fig. 3.11). The alternating combination of the multipoles is necessary due to characteristic behaviour of the octupole lens: it can introduce negative spherical aberration only along a pair of axes perpendicular to the direction of beam propagation, say x and y in Fig. 3.11. The coplanar axes at 45° to x and y axes, on the other hand, introduce positive spherical aberration [123]. Therefore, in order to have a negatively aberrated beam, a quadrupole lens has to be used to create a line focus, which is then directed along the negative aberration axis of an octupole. If, for instance, the first pair of quadrupole and octupole lenses creates a negatively spherically aberrated line focus

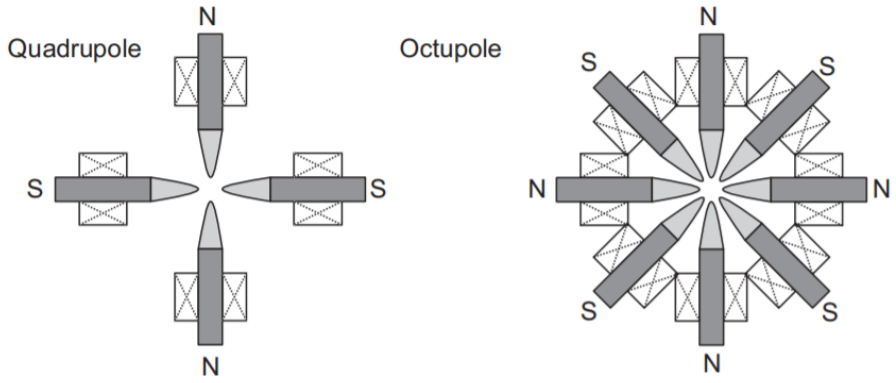


Figure 3.10: Diagram of magnetic multipoles used in spherical aberration correction (electron beam comes out of the page) [122].

in x direction, further multipole elements reshape the beam and introduce negative spherical aberration along the y-axis. Then, the final quadrupole lens recreates a round beam with desired negative spherical aberration [123].

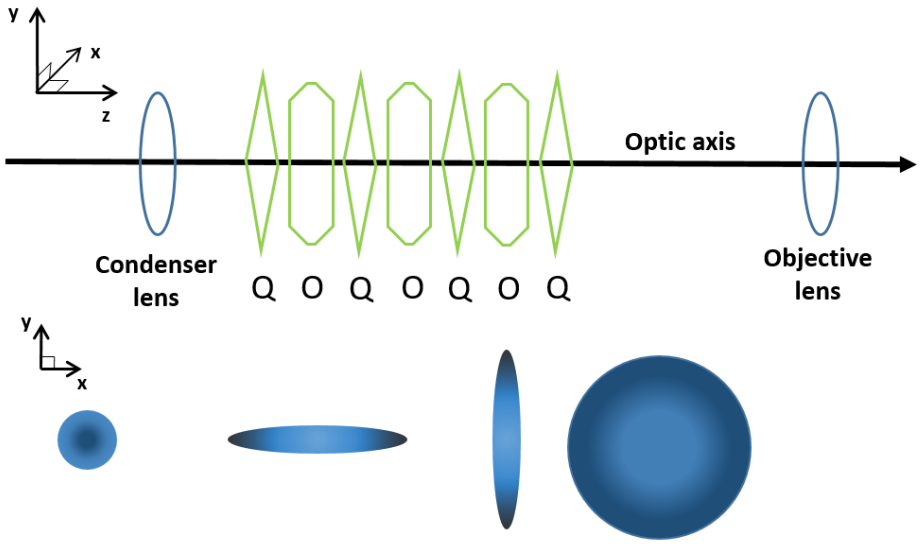


Figure 3.11: A series of quadrupole (Q) and octupole (O) lenses representing a spherical aberration correction unit in STEM. It creates an electron beam with negative spherical aberration to counteract positive spherical aberration of the objective lens. Image is adapted from [123].

## 3.2 Electron Energy Loss Spectroscopy

Electron energy loss spectroscopy (EELS) is one of the major spectroscopic techniques used in a TEM. It studies energy changes in the initially near-monochromatic electron beam after

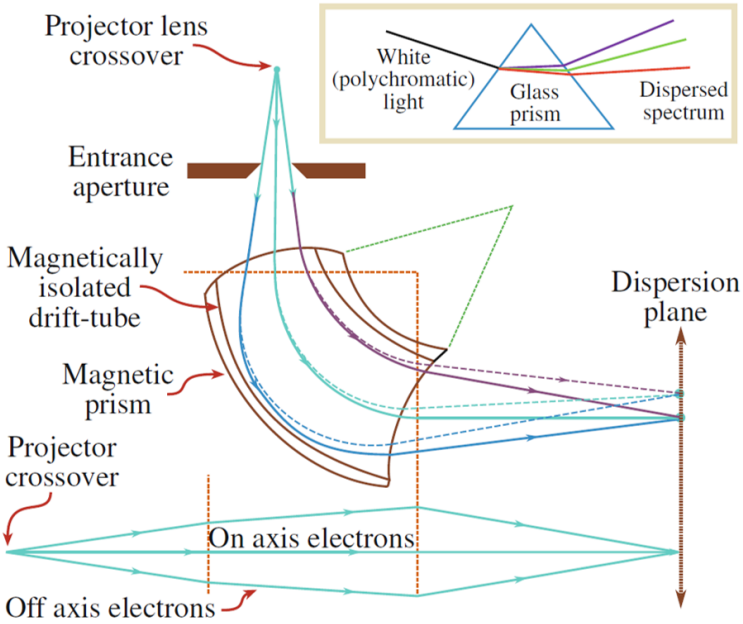


Figure 3.12: Magnetic prism changes the direction of electron motion, dispersing the electrons according to their energy [106].

it has passed through a sample. The measurable energy losses which result from inelastic interactions span a range of up to ~2 keV. Generally, losses of up to 50 eV correspond to beam interactions with valence electrons, and losses beyond 50 eV are due to interactions with the core electrons [106]. The technique provides a vast amount of information on the sample, including its chemistry, electronic structure and dielectric response.

### 3.2.1 EELS detector

The main component of the EEL detection system is a magnetic prism, shown in Fig. 3.12. It works similarly to a glass prism, which disperses white light into its components. Here, however, a uniform magnetic field created by the prism exerts a Lorentz force on electrons and changes their trajectory [106]. The extent of deflection, and therefore the position at which the electron hits the dispersion plane, depends on its the velocity (or equivalently its energy), as defined by Eqn. 3.2.1:

$$R = \frac{mv}{eB}. \tag{3.2.1}$$

Here, $e$, $v$ and $m$ are the electron charge, speed and relativistic mass [31], and $R$ is the radius of its circular orbit within the magnetic field $B$.

Unlike the glass prism, the magnetic prism also as acts as a focusing element, i.e. electrons of the same energy which are travelling in on- or off-axis directions are brought to the same

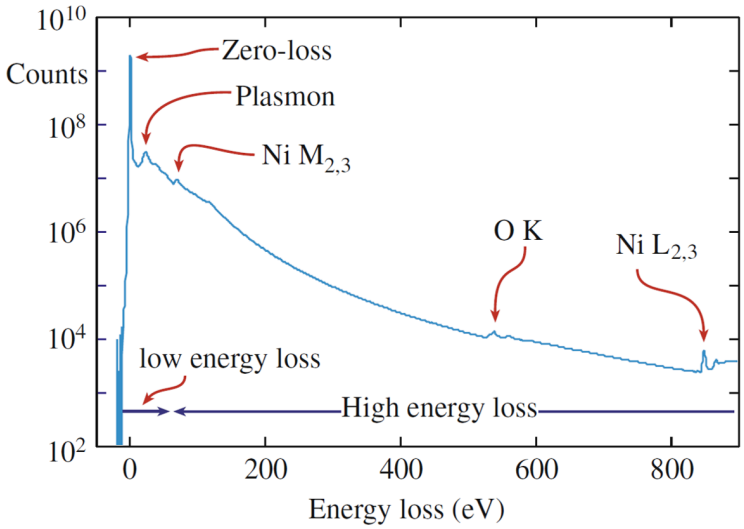


Figure 3.13: Typical EEL spectrum contains peaks associated with zero-loss, plasmon excitations and ionising interactions between the beam and core electrons in the sample [106].

focal point in the dispersion plane, finally forming a spectrum that relates electron energy loss and intensity.

### 3.2.2 EEL spectrum

The most prominent feature in the EEL spectrum (Fig. 3.13) is the zero-loss peak (ZLP). Due to the finite resolution of the spectrometer, it contains not only elastically scattered electrons, but also those electrons that lose energy of the order of meV due to phonon exitations, etc [106]. The full width at half maximum (FWHM) of the ZLP defines the resolution of the spectrometer, although is often subtracted from the spectra.

The low-loss part of the EEL spectrum also contains peaks associated with both bulk and surface plasmon excitations, which refer to collective oscillations of weakly bound valence or conduction electrons, resulting in regions of fluctuating electron density within or on the surface of the material. It is the most commonly occurring inelastic excitation, which has a differential scattering cross section of a Lorentzian shape:

$$\frac{d\sigma_\theta}{d\Omega} = \frac{1}{2\pi a_0}\left(\frac{\theta_E}{\theta^2+\theta_E^2}\right). \tag{3.2.2}$$

Here, $\theta$ is the scattering angle, $\theta_E$ is the characteristic scattering angle[1] and $a_0$ is the Bohr radius [106]. The bulk plasmon energy typically spans the range of 5-30 eV, and for materials

[1]The characteristic scattering angle is the most likely scattering angle for a given electron beam energy and energy loss value $E$. It is given by $\theta_E \approx \frac{E}{\gamma m_0 v^2}$. It simplifies to $\theta_E \approx \frac{E}{2E_0}$ for non-relativistic electrons of energy below ≈100 keV [106].

that have a free-electron structure it can be expressed as:

$$E_P = \hbar\omega_P = \hbar\sqrt{\left(\frac{ne^2}{\varepsilon_0 m_0}\right)}, \tag{3.2.3}$$

where $\omega_P$ is a plasmon frequency, $\hbar$ is a reduced Planck's constant, $\varepsilon_0$ is the permittivity of free space and $n$ is the density of free electrons of mass $m_0$ and charge $e$. The surface plasmons, on the other hand, are of lower energy compared with those of the bulk, and due to their low intensity become important only in the thinnest samples [31]. The low-loss spectrum may further contain peaks corresponding to inter-band transitions. These also occur in the energy loss region of up to ~25 eV and can be used in phase identification via a "fingerprinting" technique, which compares the recorded low-loss spectrum with the stored spectra of known samples [106].

Generally, the low-loss spectrum can be interpreted as the dielectric response of the sample to the incident electron beam. As the intensity of the spectrum is a function of the imaginary part of the dielectric function, Kramers–Kronig relations can be used to derive its real part. This information can also be obtained using optical spectroscopy; however, the advantage of EELS is that it offers better spatial resolution, and a single EEL measurement in the range of ~1.5-3 eV corresponds to optical analysis in the wavelength range of 400-800 nm (i.e., UV to infra-red) [106].

Finally, ionising interactions between the beam and core electrons in the sample are represented in the high energy-loss part of the spectrum (>~50 eV), where they give rise to peaks named core-loss edges. These carry elemental information about the sample, and, depending on both their short and long range fine structure, one can obtain data on bonding, coordination and density of states [106]. Clearly, the information derived from the high-loss energy range is similar to energy-dispersive X-ray (EDX) measurements, which detect characteristic X-rays emitted upon relaxation of an ionised atom (Fig.3.14). The EDX measurements of light elements have a low X-ray fluorescence (i.e. low probability of X-ray emission during relaxation), while EELS is much more efficient since, in principle, it can detect all ionisation events, irrespective of the atom relaxation mechanism. In this respect, both EELS and EDX are considered to be complementary techniques.

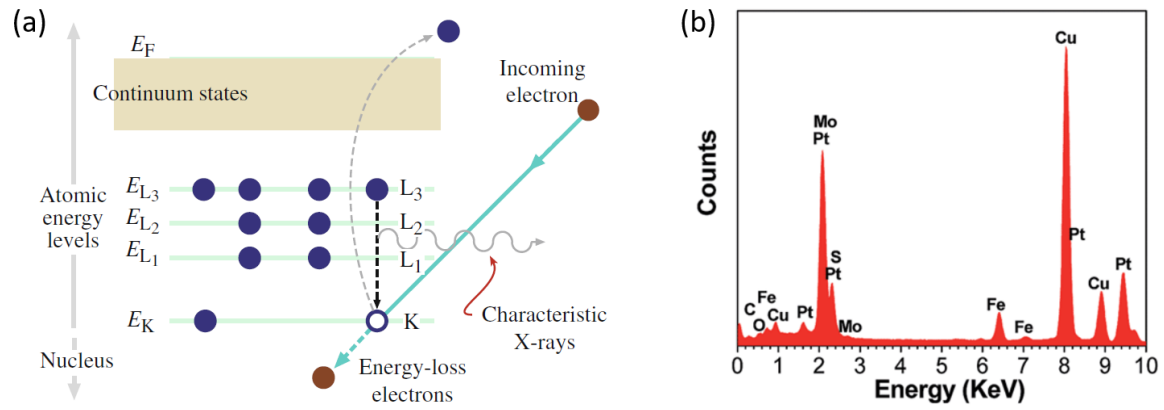


Figure 3.14: Ionisation of a K-shell electron is followed by electron relaxation from the L shell, (a). The process results in the emission of the characteristic X-ray, the energy of which depends on the energy difference between the involved shells, and hence on the type of the ionised atom [106]. (b) shows an EDX spectrum of a 2D $MoS_2$ sheet containing $Fe_3O_4$ and Pt nanoparticles (the Cu peaks are due to the background signal from the TEM specimen grid) [124].

# Chapter 4

# Experimental methodology

Electron Compton scattering experiments presented in this thesis are carried out on 3 groups of materials: amorphous carbon film, transition metal dichalcogenide $WS_2$ and metal-to-insulator transition exhibiting $VO_2$. Each of these systems requires customised experimental setup in order to capture the relevant changes in the projected electron momentum densities. Hence, this chapter describes the equipment and experimental conditions used to carry out Compton scattering experiments in each material. In addition, it also briefly outlines the sample preparation procedures for $WS_2$ thin films and $VO_2$ flakes.

## 4.1 TEM and EELS system

The experiments outlined in this thesis were carried out using a JEOL 2100F TEM equipped with a Gatan GIF Tridiem EELS detector and an Oxford X-Max 65T SDD X-ray detector, as shown in Fig. 4.1. The TEM uses a ZrO/W(100) Schottky field emission gun, which produces a bright and highly stable electron beam accelerated up to a maximum energy of 200 keV [125]. The HRTEM and diffraction images were recorded with Orius CCD camera (in experiments with amorphous carbon) and Rio CMOS camera (in experiments with $WS_2$ and $VO_2$). Both EELS and TEM imaging detectors were controlled via *Digital Micrograph* software, while the energy-dispersive X-ray measurements were carried out via *Aztec* software.

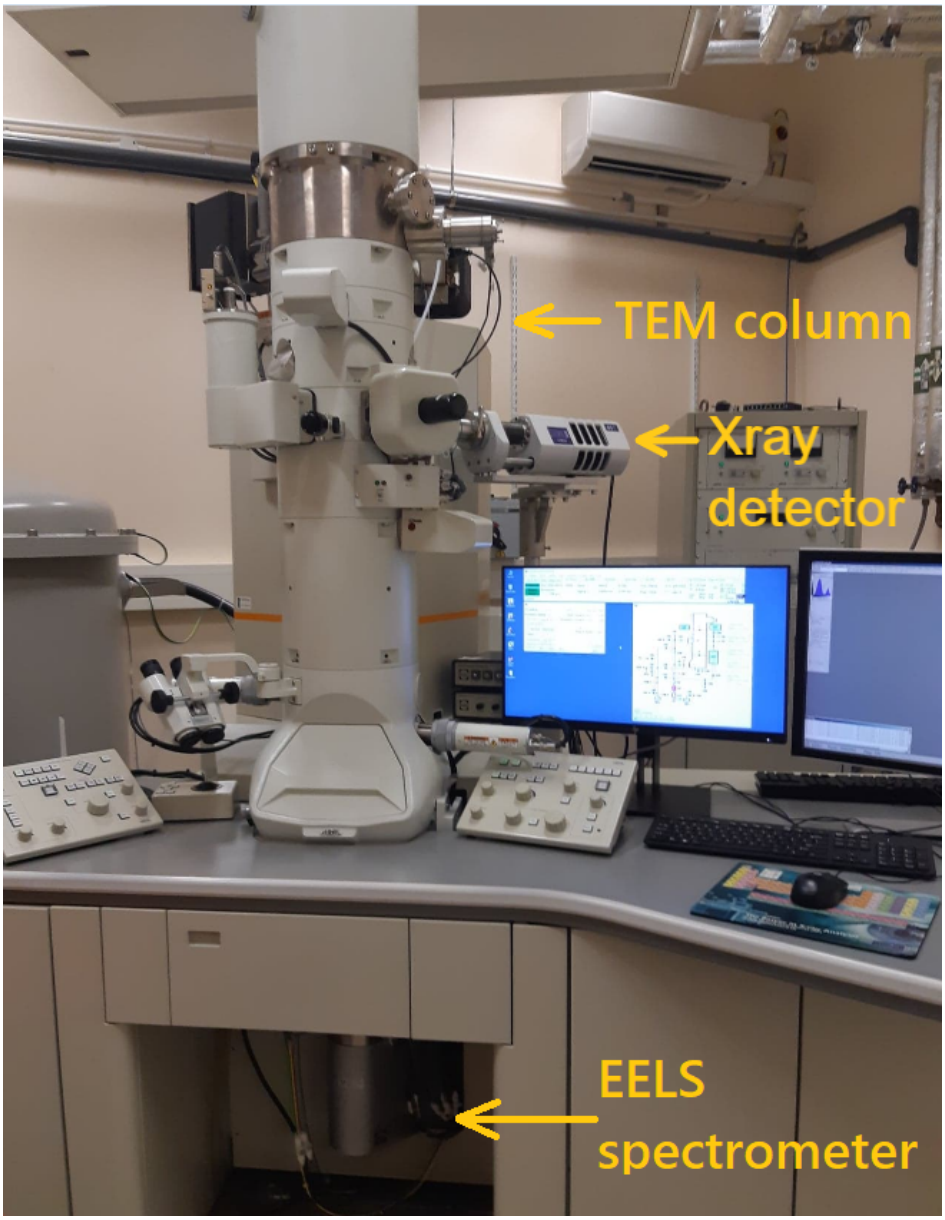


Figure 4.1: TEM and EELS system used for electron Compton scattering experiments.

## 4.2 Electron Compton scattering experiments in amorphous carbon

Investigation of the validity of impulse approximation and plasmon background subtraction in electron Compton scattering was carried out on 10 nm-thick holey carbon grids. Normally, EELS is performed using a beam centred along the optic axis of the TEM; however, Compton-scattered electrons are deflected at fairly large angles away from the optic axis. Therefore, in order to direct these electrons towards the spectrometer, a centred dark field mode is used, in which a parallel electron beam is tilted at a finite angle with respect to the sample surface

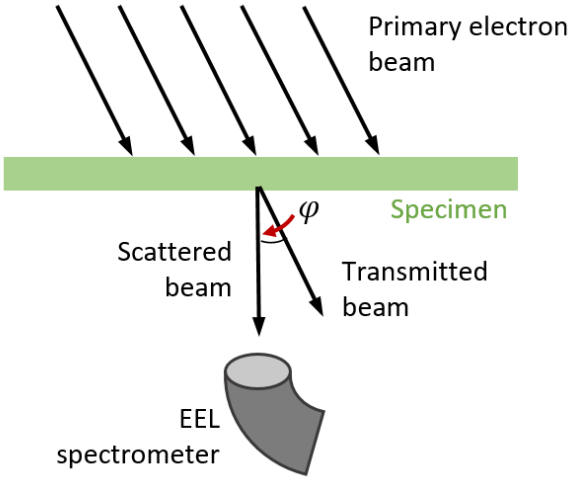


Figure 4.2: Compton scattering experiments in TEM using a tilted electron beam.

normal (Fig. 4.2).

The impulse approximation defines a one-to-one correspondence between the particle scattering angle and the energy of the Compton profile peak. Hence, in order to establish whether the soft collisions between the beam and the sample electrons can be modelled within this approximation, the changes in energy of the Compton profile peak were studied as a function of the beam tilt angle. The data obtained were further compared with a theoretical prediction for relativistic electrons, the details and derivation of which are presented in Sec. 4.1. EEL spectra were acquired using a 20 $\mu$m objective lens aperture and energy dispersions of 0.3-0.5 eV/channel. Defining $d = \frac{1}{q}$, where $q$ is the length of the scattering vector, one can obtain the electron scattering angle, $2\theta$, using Bragg's law:

$$\lambda = 2d\sin\theta, \tag{4.2.1}$$

where $\lambda$ is the wavelength of the primary electron and $\theta$ is the beam tilt angle. Applying the small angle approximation (i.e. $\sin\theta \approx \theta$), the electron scattering angle is then expressed as

$$2\theta = q\lambda, \tag{4.2.2}$$

where $q$ is measured via *Digital Micrograph* as the distance between the transmitted electron beams in bright field and centred dark field modes in diffraction space, as shown in Fig. 4.3.

The projected momentum densities of amorphous carbon films were obtained after subtracting the plasmon background, assuming that the zero-loss peak ZLP contribution to the Compton profile is negligible.

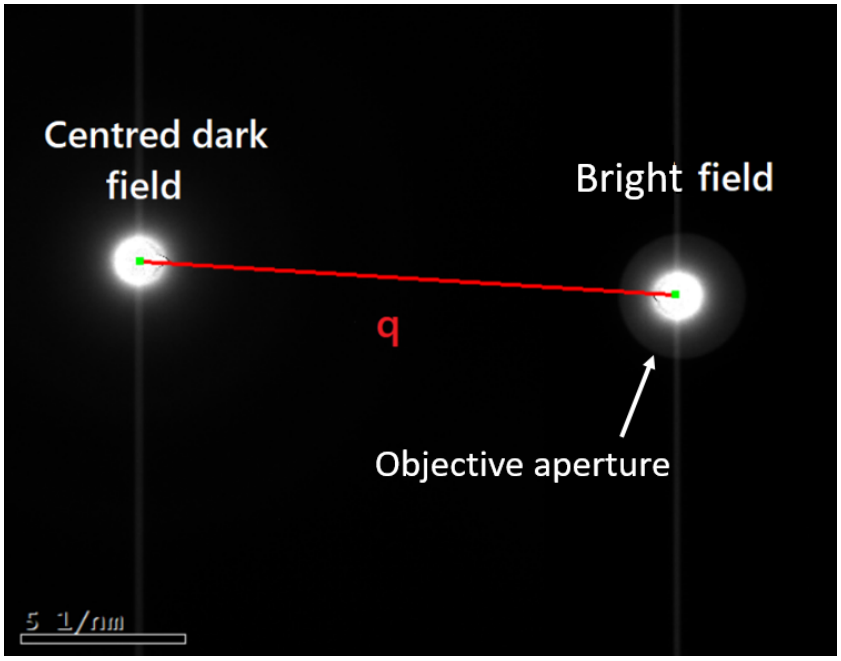


Figure 4.3: Transmitted electron beam in bright field and centred dark field modes.

Electron Compton scattering measurements were also carried out using a collapsed TEM beam as an approximation to the standard STEM set-up. Under these conditions, the beam convergence angle is determined by the size of the condenser lens aperture. Two beam convergence angles were tested in the experiments - 4.9 mrad and 12.3 mrad, corresponding to 3.9 $nm^{-1}$ and 9.7 $nm^{-1}$ momentum spread in the primary electron beam. The resulting EELS spectra and Compton profiles were analysed as those obtained using a parallel electron beam, i.e. the scattering angle was defined with respect to the centre of the STEM probe disc in reciprocal space.

## 4.3 Electron Compton scattering in $WS_2$

The $WS_2$ sample studied in this work was prepared by Pranab Kishore Mohapatra and Assael Cohen from Tel Aviv University, Israel. The film was grown on a sapphire substrate via "growth-etch" metal-organic chemical vapour deposition (GE-MOCVD) at a temperature of 850 °C and 50 Torr pressure [126]. The method involves a pulsed delivery of tungsten carbonyl ($W(CO)_6$) and di-tert-butyl sulfide (DTBS) precursors with a supply of $H_2O$ vapour between the growth cycles [126]. Here, $H_2O$ vapour acts as an etchant for part of $WS_2$ nuclei and carbon contaminants ensuring the growth of large $WS_2$ domains. After the growth, the $WS_2$ film was transferred onto a TEM grid using the surface-energy-assisted process [126,127]. Specifically, a layer of polystyrene was spin-coated on the substrate and baked to secure good adhesion

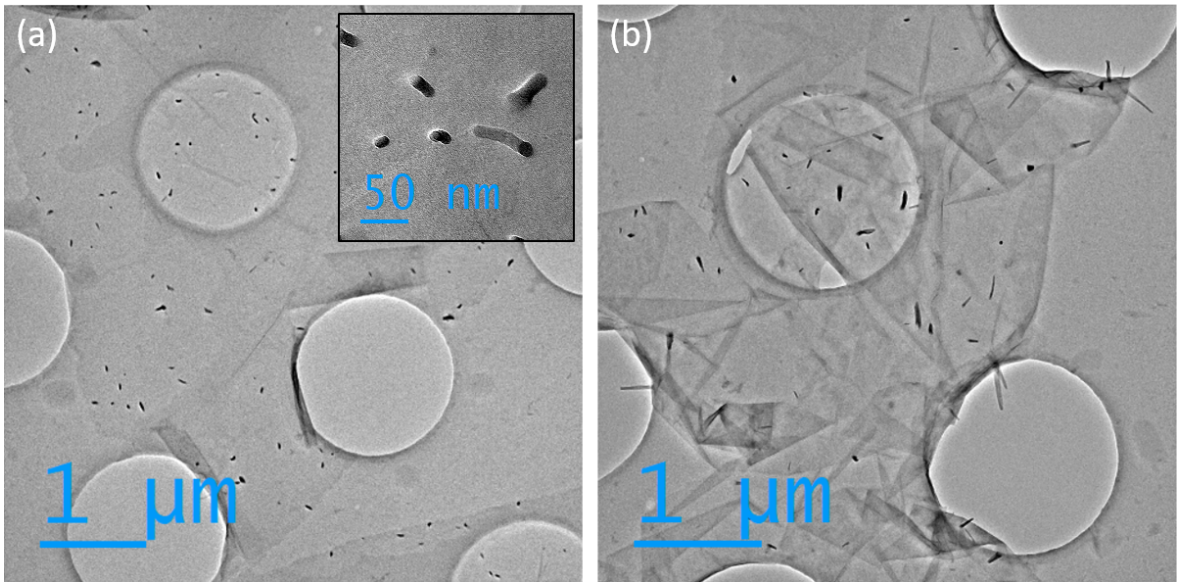


Figure 4.4: Monolayer (a) and multilayer (b) regions of the $WS_2$ sample deposited on an amorphous holey carbon TEM grid. The films contain a number of protruding contaminating particles, which are shown magnified in the inset of (a). These are most likely associated with the $WS_2$ growth or transfer processes.

between $WS_2$ and the polymer. The assembly was then immersed into deionised water resulting in delamination of $WS_2$/polystyrene film from the substrate due to hydrophobic and hydrophilic properties of the $WS_2$ and sapphire respectively. The film was then transferred onto the TEM grid and the remaining polystyrene coating was dissolved with toluene [126,127]. TEM micrographs of the deposited monolayer and multilayer domains of $WS_2$ are shown in Fig. 4.4.

Due to scarcity of suitable multilayer $WS_2$ regions in the given sample for electron Compton scattering experiments, another sample of multilayer/bulk $WS_2$ was prepared using a shear exfoliation method. For that, $WS_2$ powder purchased from *Sigma-Aldrich* was dispersed in IPA and mixed using a *Silverson L5M* homogeniser for an hour at 3000 rpm. The resulting dispersion was drop-cast onto a holey carbon TEM grid, which was then blotted on a filter paper and air-dried.

In order to investigate layer-dependent variations in $WS_2$ electronic band structure via electron Compton scattering, the EELS spectrum must be acquired along well-defined crystallographic scattering directions, unlike in amorphous carbon, which is isotropic. As shown in Fig. 2.16, the most significant changes in $WS_2$ band structure with an increasing number of layers occur along the Γ-K direction of the reciprocal lattice. Therefore, in order to measure these changes, the electron beam has to be tilted so that only electrons scattered along the $[10\bar{1}0]$ K-reciprocal direction are selected by the objective aperture. Fig. 4.5 shows the setup

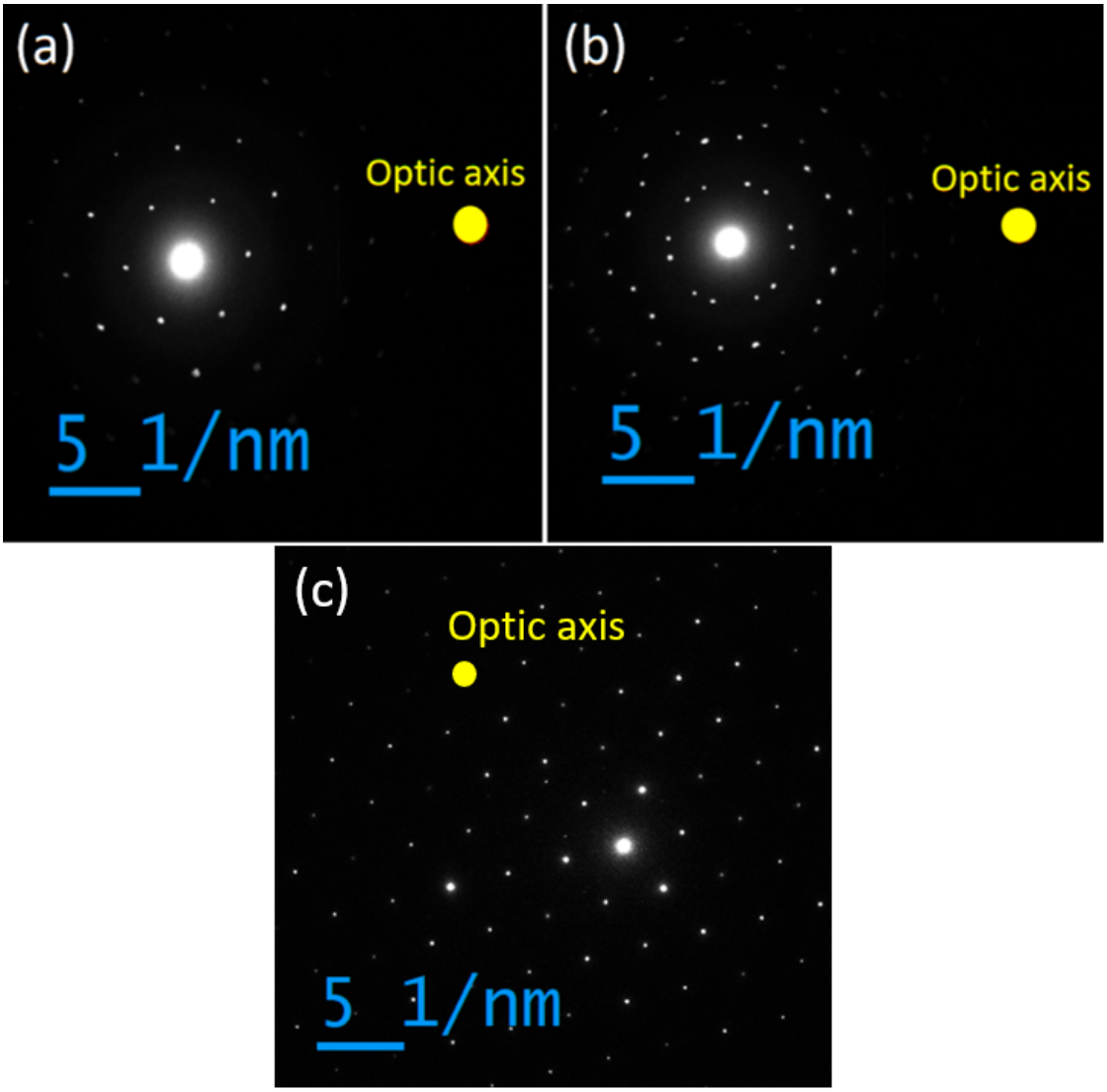


Figure 4.5: Electron beam and diffraction pattern alignment for electron Compton scattering experiments in monolayer (a), bilayer (b) and bulk (c) $WS_2$.

in diffraction space for monolayer, bilayer and bulk $WS_2$. As bilayer regions are rotationally misaligned, the scattering vector for the bilayer is chosen to pass inbetween the two K-points of the individual layers. The measurement of the bulk sample also required additional steps in the setup of the experiment due to dynamical electron scattering effects (Sec. 6.3). In particular, the sample had to be tilted away from the zone axes in order to minimise the high intensity Bragg reflections, as shown in Fig. 4.6. Despite tilting away from the zone axis, strong scattering in $WS_2$ meant that a large number of Bragg beams were still observed during Compton EELS measurement (Fig. 4.5(c)).

Due to the strong plasmon background and potential inaccuracies associated with its subtraction, Compton scattering experiments for monolayer and bilayer were carried out at 39.5 mrad scattering angle, which places the Compton peak at approximately 420 eV. This energy is

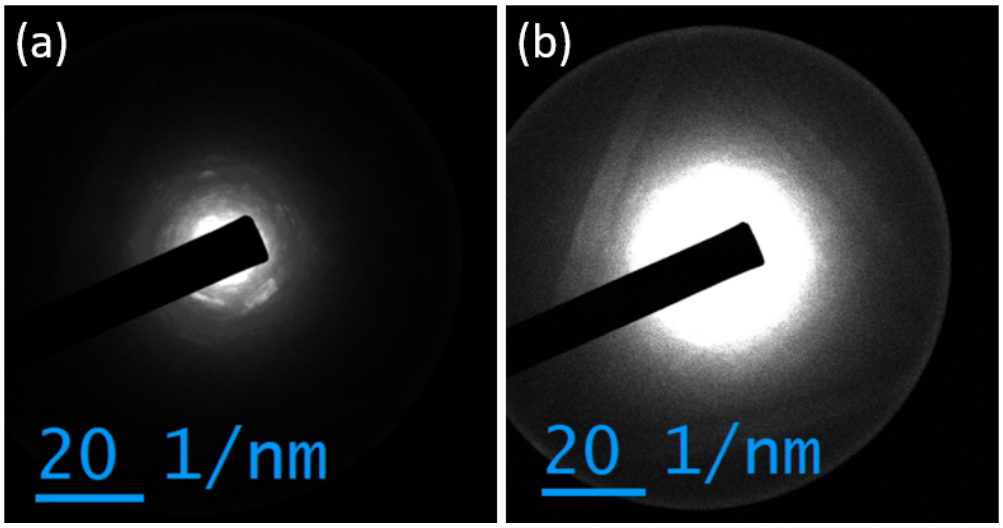


Figure 4.6: Convergent beam electron diffraction patterns for bulk $WS_2$ showing the incident beam directed away from the zone axes. The image contrast in (b) is digitally increased compared to (a) in order to see the Kikuchi bands.

Table 4.1: Electron binding energies in free W($1s^2$ $2s^2p^6$ $3s^2p^6d^{10}$ $4s^2p^6d^{10}f^{14}$ $5s^2p^6d^4$ $6s^2$) and S($1s^2$ $2s^2p^6$ $3s^2p^4$) atoms in eV. Table adapted from [128].

| Z | | K | $L_1$ | $L_2$ | $L_3$ | $M_1$ | $M_2$ | $M_3$ | $M_4$ |
|---|---|---|---|---|---|---|---|---|---|
| 74 | W | 69529 | 12103 | 11546 | 10209 | 2823 | 2577 | 2283 | 1874 |
| 16 | S | 2476 | 232 | 170 | 168 | 20.20 | 10.36 | | |

| Z | | $M_5$ | $N_1$ | $N_2$ | $N_3$ | $N_4$ | $N_5$ | $N_6$ | $N_7$ |
|---|---|---|---|---|---|---|---|---|---|
| 74 | W | 1811 | 599 | 495 | 428 | 261 | 248 | 38 | 36 |

| Z | | $O_1$ | $O_2$ | $O_3$ | $O_4$ | $O_5$ | $P_1$ |
|---|---|---|---|---|---|---|---|
| 74 | W | 80 | 51 | 41 | 9.0 | | 8.0 |

also higher than the carbon K-edge core loss peak due to any hydrocarbon contamination on the specimen surface. Under these experimental conditions only the electrons of binding energy of up to ≈420 eV are sampled. Therefore, for $WS_2$, 70 electrons per formula unit will contribute to the Compton peak (Table 4.1). For the bulk material, the scattering angle was 33.4 mrad; however, extraction of the Compton profile remained complicated despite the effort to reduce multiple scattering artefacts.

The measurements were taken using a 20 $\mu$m objective aperture and EELS energy dispersion of 0.5 eV/channel. Also, due to the sensitivity of the monolayer $WS_2$ to a high energy electron beam, the irradiation intensity was minimised by increasing the first condenser lens strength (i.e. spot size) to the highest value possible. The total fluence during Compton measurements was kept below the critical value (see Section 6.2 for more details). The projected momentum

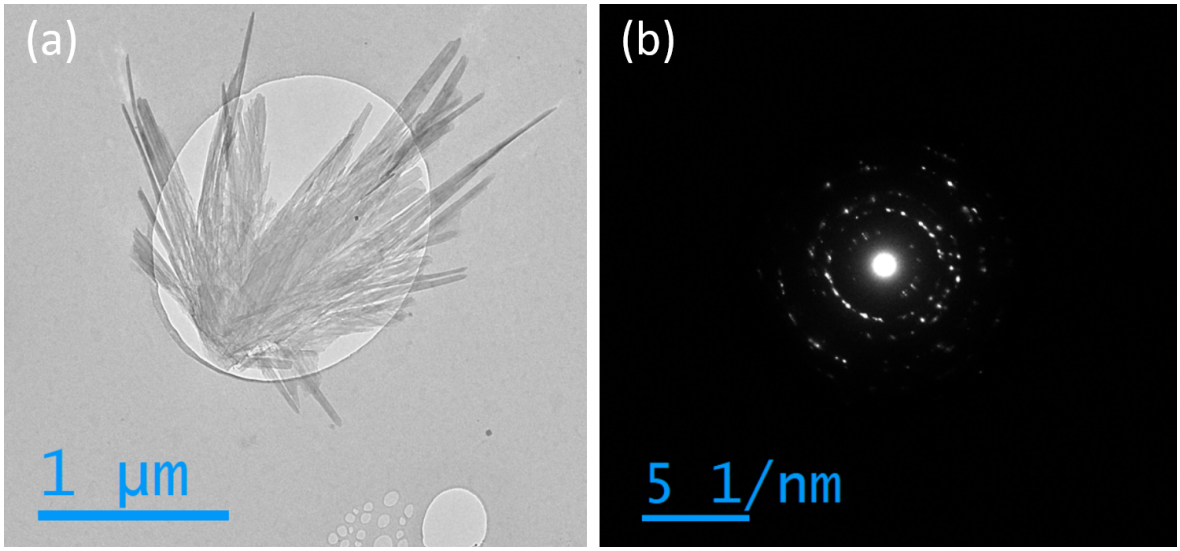


Figure 4.7: TEM image of a $VO_2$ flake, (a), and a corresponding electron diffraction pattern, (b), taken at room temperature.

densities of $WS_2$ films were obtained assuming that at these high electron scattering angles the ZLP and plasmon contribution to the Compton profile is negligible after background subtraction.

## 4.4 Electron Compton scattering in $VO_2$

The $VO_2$ sample for TEM was prepared via a drop-casting method using $VO_2$ powder obtained from *Sigma-Aldrich*. A small amount of powder was dispersed and ultrasonicated in IPA in order to produce electron-transparent $VO_2$ flakes. The dispersion was then drop-cast onto a holey carbon TEM grid, which was subsequently blotted on a filter paper and air-dried. An image and a corresponding diffraction pattern of one of the deposited flakes are shown in Fig. 4.7

As outlined in Sec. 2.1.1, the phase change in $VO_2$ occurs at approximately 68 °C, beyond which the insulating material becomes metallic. Therefore, in order to track changes in $VO_2$ electronic structure, electron Compton scattering measurements were carried out at both room temperature (≈21 °C) and 90 °C, at a scattering angle of 40 mrad. Under these experimental conditions, the Compton profiles peak at about 430 eV and consequently represent 25 electrons per formula unit, as indicated in Table 4.2. Furthermore, due to the polycrystalline nature of the flakes and difficulty in consistently obtaining Compton measurements along a specific crystallographic direction, isotropic Compton profile measurements were obtained by summing a number of EELS spectra acquired along arbitrary scattering directions. As

Table 4.2: Electron binding energies in free V($1s^2$ $2s^2p^6$ $3s^2p^6d^3$ $4s^2$) and O($1s^2$ $2s^2p^4$) atoms in eV. Table adapted from [128].

| Z | | K | $L_1$ | $L_2$ | $L_3$ | $M_1$ | $M_2$ | $M_3$ | $M_4$ | $M_5$ | $N_1$ | $N_2$ |
|---|---|---|---|---|---|---|---|---|---|---|---|---|
| 23 | V | 5470 | 633 | 525 | 518 | 72 | 44 | 43 | 8 | | 6.740 | |
| 8 | O | 538 | 28.48 | 13.62 | | | | | | | | |

in experiments with $WS_2$, the measurements were taken using a 20 µm objective aperture, 0.5 eV/channel EELS energy dispersion and minimised electron irradiation intensity. The sample heating was carried out with Gatan model 900 heater and Gatan model 914 tomography holder, which can maintain constant temperatures of up to 100 °C. As the holder temperature is not calibrated, a higher temperature of 90 °C was deliberately selected (it is not expected to deviate from the real temperature by more than a few degrees), and the sample was kept at this temperature for 30 minutes in order to ensure consistent phase transition in all the $VO_2$ flakes.

# Chapter 5

# Electron Compton scattering in amorphous carbon films

Traditionally, electron Compton scattering experiments are carried out in a high energy transfer regime in which electron scattering angles are relatively large. This approach ensures validity of the impulse approximation and provides a way to convert the obtained Compton profile into an electron momentum distribution of the probed material. However, experiments conducted in this regime present a number of complications such as low electron count number and a need to subtract the core electron contribution from the Compton profile via density functional theory (DFT) methods.

In this chapter, an alternative experimental method employing low energy transfer is studied with the aim to improve data collection efficiency and eliminate the need of the core electron background subtraction from the acquired electron momentum density profiles. Here, experiments are carried out on an amorphous carbon film, studying Compton scattering at low angles. Particular emphasis is placed on investigating the validity of the impulse approximation and relatively simple plasmon background subtraction methods. The chapter also explores the possibility of conducting similar experiments in STEM mode, which could potentially enable extraction of Compton profiles at high spatial resolution.

## 5.1 Impulse approximation theory

Interpretation of the Compton spectrum in terms of the momentum distribution of target electrons relies on the validity of the impulse approximation, which assumes that relaxation

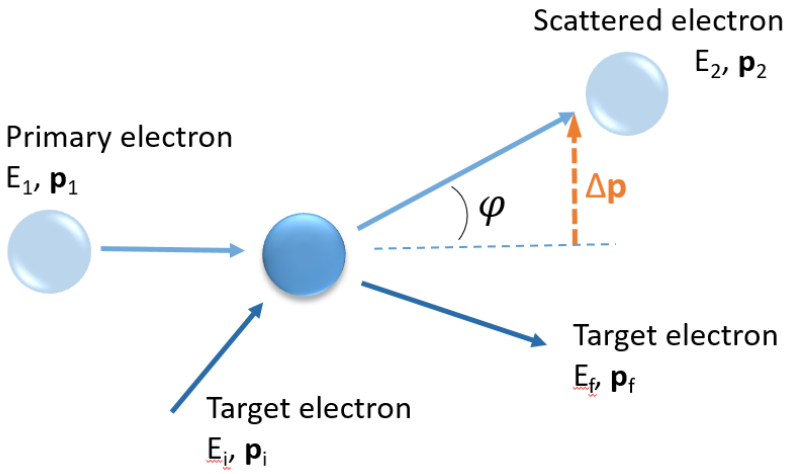


Figure 5.1: Compton scattering process between the primary and target electrons.

of background electrons and nuclei in the target is negligible during the collision [12,32]. Under this condition, any changes in the potential energy can be ignored. In TEM, where highly energetic electron beams are accelerated to a substantial fraction of the speed of light, relativistic effects must be considered, giving the following energy and momentum conservation relations:

$$E_1 + E_i = E_2 + E_f, \tag{5.1.1}$$

$$\mathbf{p}_1 + \mathbf{p}_i = \mathbf{p}_2 + \mathbf{p}_f, \tag{5.1.2}$$

$$E^2 = (T + m_0c^2)^2 = (pc)^2 + (m_0c^2)^2, \tag{5.1.3}$$

where $E_1$, $\mathbf{p}_1$ and $E_2$, $\mathbf{p}_2$ are the energies and momenta of the primary and scattered electron; $E_i$, $\mathbf{p}_i$ and $E_f$, $\mathbf{p}_f$ are the initial and final energies and momenta of the target electron (Fig. 5.1); $T$ is the kinetic energy of an electron of rest mass $m_0$, and $c$ is the speed of light. Equations 5.1.1-5.1.3 can be used to obtain the relation linking the energy, $\Delta T$, and momentum, $\Delta\mathbf{p}$, transferred by the primary electron:

$$\Delta T(m_0c^2) = \frac{1}{2}c^2\left|\Delta\mathbf{p}\right|^2 - \frac{1}{2}(\Delta T^2) - c^2\mathbf{p}_i \cdot \Delta\mathbf{p} - T_i\Delta T. \tag{5.1.4}$$

Further, assuming that $|\mathbf{p}_1| \simeq |\mathbf{p}_2|$, the magnitude of the momentum transfer is given by $|\Delta\mathbf{p}| = 2\left|\mathbf{p}_1\right|\sin\frac{\phi}{2}$. Substituting into equation 5.1.4, where the $\frac{1}{2}\Delta T^2$ term can be neglected assuming that $\Delta T \ll m_0c^2$, equation 5.1.4 can be rewritten as:

$$\Delta T(m_0c^2) = 2c^2\left|\mathbf{p}_1\right|^2\sin^2\frac{\phi}{2} - c^2\mathbf{p}_i \cdot \Delta\mathbf{p} - T_i\Delta T. \tag{5.1.5}$$

Setting both the initial kinetic energy of the target electron, $T_i$, and initial momentum, $\mathbf{p}_i$, to zero gives the energy transfer at the peak of the Compton profile, $\Delta T_p$, as a function of the scattering angle, $\phi$:

$$\Delta T_p = 2\sin^2\frac{\phi}{2}\left(2T_1 + \frac{T_1^2}{m_0c^2}\right). \tag{5.1.6}$$

Here, equation 5.1.3 was used to express $p_1$ in terms of the kinetic energy $T_1$ of the primary electron.

In order to express the energy transfer in terms of the momentum of a target electron projected along the scattering vector, $p_z$, one can substitute $\Delta T = \Delta T_p + \delta T$ into equation 5.1.4, where the term $T_i\Delta T$ can be neglected since $T_i \ll m_0c^2$. Considering that $\Delta T_p(m_0c^2) = \frac{1}{2}c^2\left|\Delta\mathbf{p}\right|^2 - \frac{1}{2}(\Delta T^2)$, we obtain:

$$p_z = \frac{-\delta T m_0}{|\Delta\ \mathbf{p}|} = -\delta T\sqrt{\frac{m_0}{2\Delta T_p}}. \tag{5.1.7}$$

Equation 5.1.7 is used to calculate the projected momentum $p_z$ at a given energy loss. Using this method the Compton peak in the energy loss spectrum can be transformed into a $J(p_z)$ curve representing projected momentum distribution of electrons in the solid.

## 5.2 Impulse approximation experiments

The validity of the impulse approximation was investigated by comparing the measured values of electron energy loss at the peaks of Compton spectra with the values predicted by equation 5.1.6. The Compton profiles were acquired in TEM mode with tilted illumination, so that only those electrons that are scattered along the optic axis of the microscope are collected by the EELS entrance aperture, as shown in Fig. 4.2. A holey carbon film was selected as a suitable test specimen having a number of benefits such as its thinness (which minimises multiple scattering artefacts), lack of anisotropy due to the amorphous nature of the sample and availability of several reports on Compton scattering in carbon-based materials which can be used as reference [28, 33].

The energy loss of the Compton peak as a function of the scattering angle for a holey carbon specimen is shown in Fig 5.2. The errors in the scattering angle are determined by the radius of the objective aperture and the errors in the energy loss were estimated at the limits of 95% of the Compton peak intensity. Generally, the impulse approximation is expected to break down in the low energy transfer regime [12]. However, Fig. 5.2 shows that the observed scattering behaviour is described by the impulse approximation even at low scattering angles,

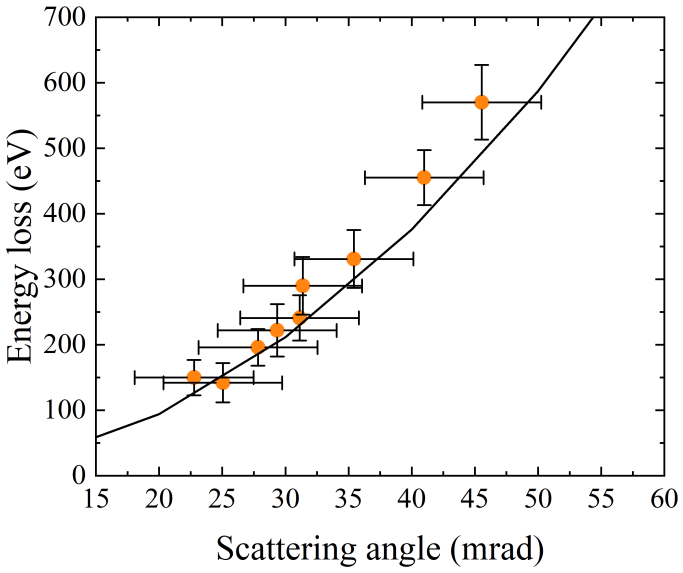


Figure 5.2: The measured values of energy loss at the peaks of Compton spectra across a range of beam tilt angles (points) compared with the predictions of the impulse approximation (solid line).

between 20-30 mrad, where the energy transfer is below the carbon $K$ shell binding energy. A core hole is an extreme example of change in potential during inelastic scattering and can introduce peak shifts of up to a few eV in EELS core loss edges [129, 130]. Assuming a 1 eV peak shift due to breakdown of the impulse approximation gives an uncertainty of only 0.01 atomic units in $p_z$ (equation 5.1.7) for the smallest scattering angle in Fig. 5.2. Therefore, Compton profiles in the low energy transfer regime are expected to still provide accurate measurements. Following appropriate plasmon subtraction methods discussed below, these spectra can be transformed into momentum density profiles (equation 5.1.7) containing the contributions only from the valence electrons. This is a significant improvement over the traditional method of acquiring Compton profiles at high energy loss, where both the core and valence electrons participate in scattering, requiring the contribution of the former to be removed via computational techniques [28, 33, 34]. Since the impulse approximation has been shown to be approximately valid even at low energies, Compton profiles due to only the valence electrons can be directly acquired, thereby avoiding the need for any computation-based data analysis. The shorter acquisition times for the low energy Compton profiles is a further advantage.

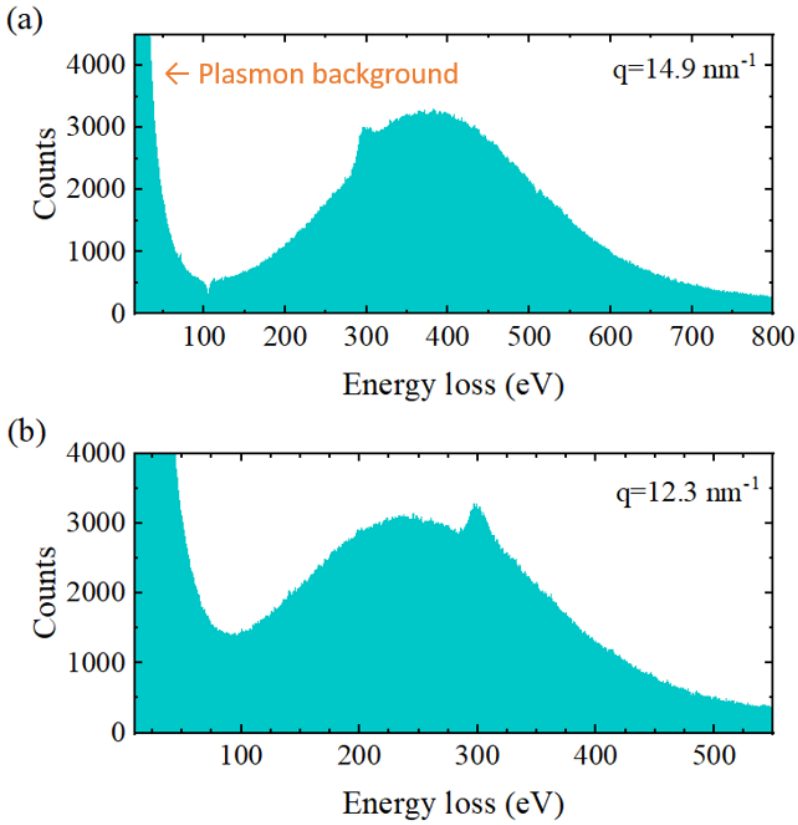


Figure 5.3: EELS spectra containing Compton profiles at high, (a), and low, (b), scattering angles. In the latter, plasmon background has to be subtracted in order extract the Compton profile.

## 5.3 Plasmon background subtraction and $J(p_z)$ profiles

In order to obtain and compare projected momentum density profiles, $J(p_z)$, of amorphous carbon films, the plasmon background has to be subtracted from the Compton spectra. At high electron scattering angles, the intensity contribution from plasmonic excitations in the range of the Compton profile is negligible; however, it becomes increasingly significant at lower scattering angles, where the energy transfer is below the binding energy of the carbon K-shell, as shown in Figs. 5.3 (a) and (b).

Potential plasmon background subtraction techniques were first examined by looking at the behaviour of plasmon spectra over a number of different scattering angles. As mentioned in Section 3.2.2, the cross-section for plasmon excitations is defined by a Lorentzian distribution, the peak of which is expected to be shifted to higher energy loss with an increasing scattering angle [31]. However, as shown in Fig. 5.4, a near constant plasmon shape and peak position is observed, which suggests that these spectra originate mainly from double scattering rather

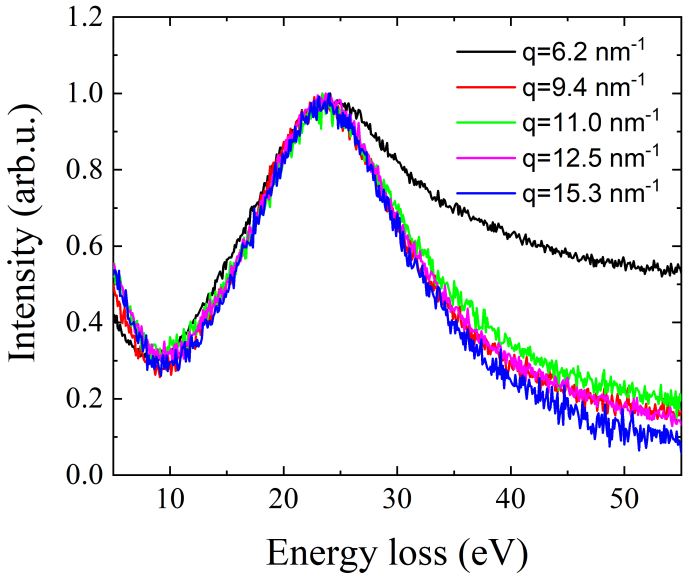


Figure 5.4: Plasmon peaks measured at a range of different energy and momentum transfer values. The increase in intensity at the high-energy tale at momentum transfer $q = 6.2$ nm$^{-1}$ is an artefact from a Compton peak located at a close proximity to the plasmon peak. Furthermore, the spectra for $q = 9.4$ nm$^{-1}$ and $q = 12.5$ nm$^{-1}$ strongly overlap.

than single inelastic scattering events. In other words, the (tilted) primary electron beam is elastically scattered towards the optic-axis and also undergoes low angle plasmon inelastic scattering. The single inelastic scattering contribution is expected to be negligible due to the narrow Lorentzian distribution for plasmon excitation. In this way, the plasmons measured at the relatively large beam tilt angles used for Compton scattering are essentially identical to plasmons measured at a zero tilt angle, suggesting that a spectrum of the latter could be subtracted as background from the former to extract the Compton profile. Nonetheless, the applicability of this method is highly dependent on the extent of beam damage to the sample, which causes widening and shifting of the plasmon peak to lower energy loss, as was observed in our experimental conditions and is shown in Fig. 5.5(a). Here, a highly damaged sample area (Fig. 5.5(b)) was analysed in order to amplify otherwise less prominent beam damage effects observed during the regular Compton scattering experiments. The widening of the plasmon peak during sputter damage is caused by a higher density of defects within the material, while the shift to lower energies is due to a reduction in the electron density (recall that for a free electron solid the plasmon peak energy varies as the square root of the electron density [31]). Therefore, the described background subtraction technique can only be used on more robust materials or with beam energies below the knock-on threshold.

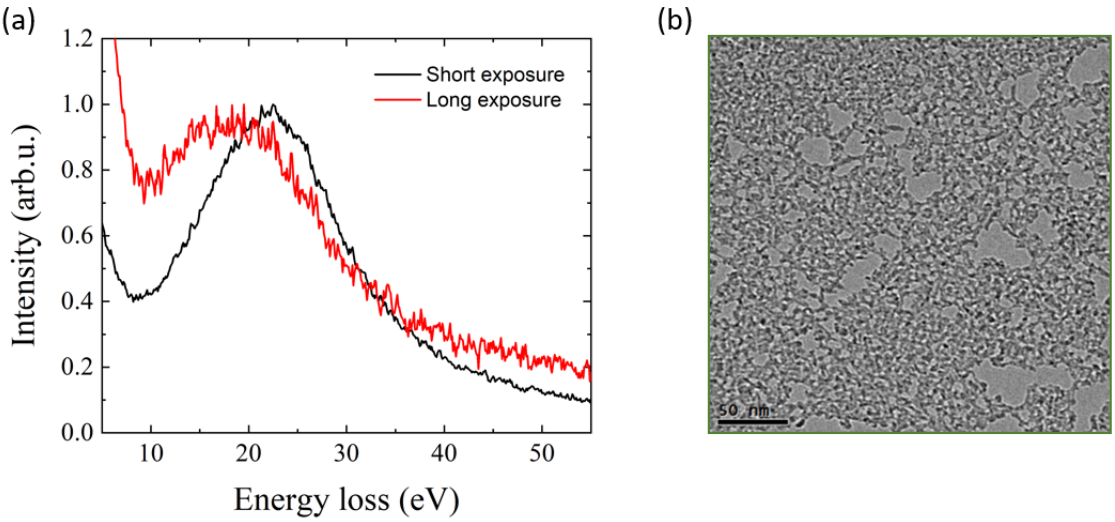


Figure 5.5: Sample damage caused by long exposure to electron beam causes widening and shifting of the plasmon peak, (a). (b) shows the corresponding highly damaged sample area.

Further, plasmon background subtraction using single analytical functions, such as a Gaussian or Lorentzian, was tested but did not produce satisfactory results: the extracted Compton spectrum and the resulting $J(p_z)$ profile contained a secondary peak at high $p_z$ values, as depicted in Figs. 5.6(a) and 5.6(b). This arises due to the fact that the plasmon has a longer tail compared to either a single Guassian or Lorentzian profile. A similar problem arises with the fitting of analytic functions to atom scattering factors. The solution adopted in the literature is to use either multiple Gaussians [131] or multiple Gaussians and Lorentzians [132]. Thus, a plasmon peak was also fitted to a function consisting of a linear combination of Gaussian and Lorentzian functions in order to obtain a more realistic approximation of the $J(p_z)$ profile. The functions and their respective reduced $\chi^2$ statistics are summarised in Table 5.1. The table also compares integrated areas[1] of the resulting Compton profiles, which are generally subject to a normalisation rule: the integral of the profile has to be equal to the number of electrons participating in scattering [12]. Since the peak of the Compton profile was below the carbon K-edge, only the valence (i.e. $2s^2$ and $2p^2$) electrons are scattered. Therefore, integration of half of the Compton profile should yield 2 valence electrons. Both the

[1]Note that in order to determine integrated areas correctly, axes conversion is necessary. While the conversion between energy loss and $p_z$ (i.e. x-axis) is well defined by equation 5.1.7, conversion between electron counts and $J(p_z)$ (i.e. y-axis) was carried out using the normalisation rule of the Compton profile and a previously outlined finding of near constant plasmon shape over a wide range of electron scattering angles. In particular, y-axis of the Compton profile in the high angle scattering regime was first scaled to give an integrated area of 3 (half of the Compton profile representing half of the 6 electrons in carbon was analysed). Then, representation of the plasmon height in the new scaling was established and used to scale spectra obtained at low electron scattering angles.

Lorentzian and Gaussian + Lorentzian fits produced reasonable $\chi^2$ values and an integrated area close to the expected result. A single Gaussian, on the other hand, was a poor fit to the data.

Table 5.1: Comparison of functions fitted to the plasmon peak.

| **Fitting function** | **Reduced $\chi^2$ statistics** | **Integrated area** |
|---|---|---|
| Gaussian | 4.50 | 2.74 |
| Lorentzian | 0.82 | 2.02 |
| Gaussian + Lorentzian | 0.53 | 2.00 |
| Power law | 1.13 | 1.81 |

Among the tested functions, those with Gaussian and Lorentzian components failed to produce the expected smooth slope of the Compton profile, with the Gaussian + Lorentzian fit minimising the secondary peak at high $p_z$ values but not completely eliminating it. Therefore, rather than fitting the entire plasmon shape, attention was focused on fitting only the tail region accurately. This approach results in large fitting errors close to the plasmon peak, but it is assumed that the intensity of the Compton profile is sufficiently small in that region. The power law function, commonly used for EELS background subtraction [31], was fitted to the plasmon tail region. The power law background subtraction method, on the other hand, produced both reasonable $J(p_z)$ profile lineshape and integrated area, as shown in Figs. 5.7(a) and 5.7(b). It should be noted that the improved result for power law background subtraction is likely to be due to the fact that fitting was carried out within the plasmon tail region only. It does not imply that the power law is a better description of the plasmon intensity than, say, Gaussian or Lorentzian functions. In Fig. 5.8, the Compton profile obtained via plasmon subtraction using power law is compared to the one measured in the high energy transfer regime. As expected, the decay length of the Compton profile obtained in the hard collision regime is longer due to the contribution from the core electrons. The Compton profiles for both all and valence-only electrons are also similar to those reported for graphite [28], depicted in Fig. 5.9.

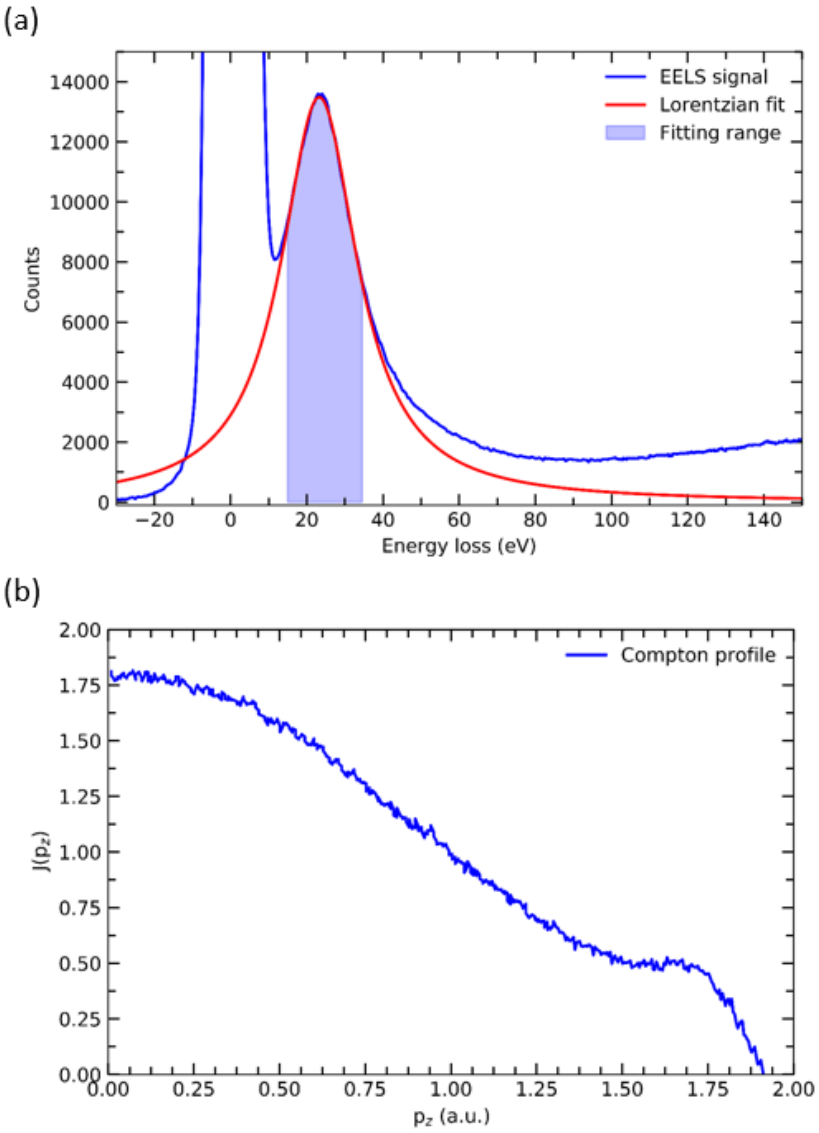


Figure 5.6: Plasmon fitting to a Lorentzian function, (a), and a resulting $J(p_z)$ profile containing a secondary peak at large $p_z$, (b).

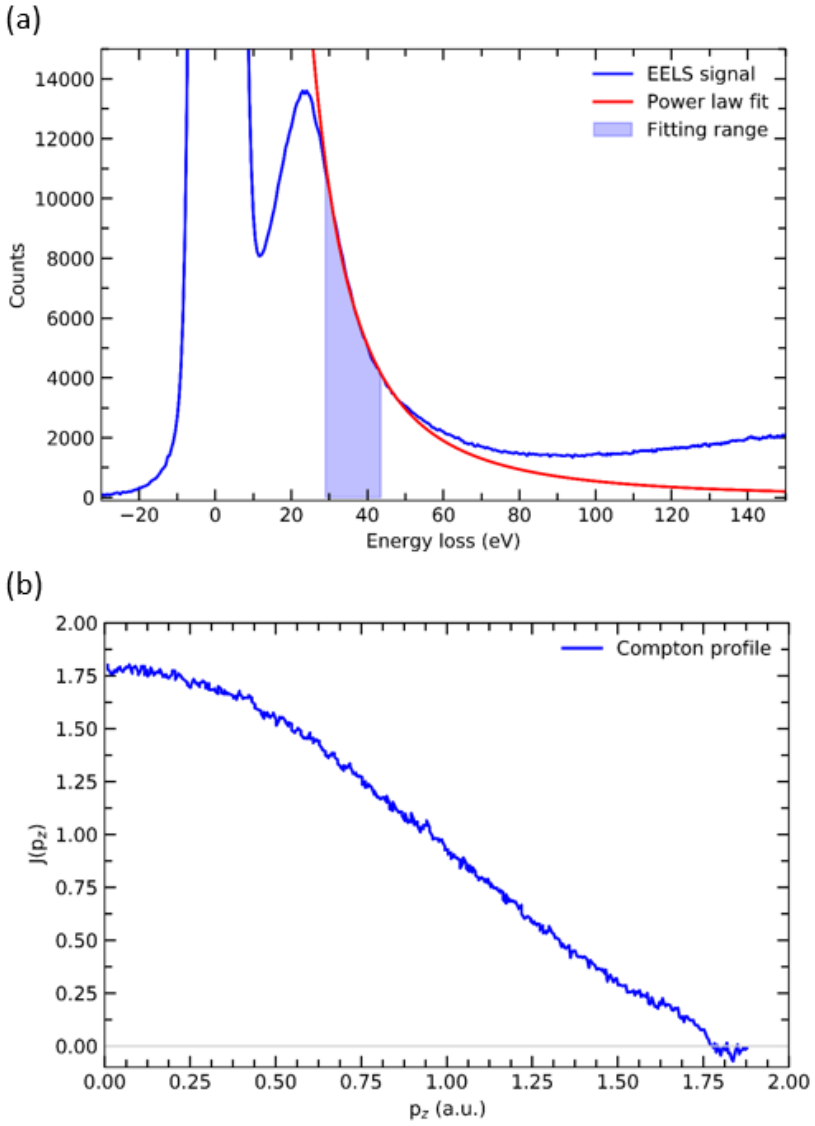


Figure 5.7: Plasmon tail fitting to power law function, (a), and a resulting $J(p_z)$ profile, (b).

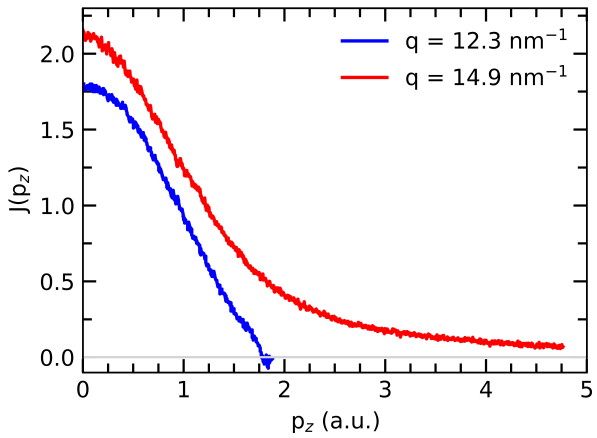


Figure 5.8: Compton profiles obtained at high (red) and low (blue) scattering angles.

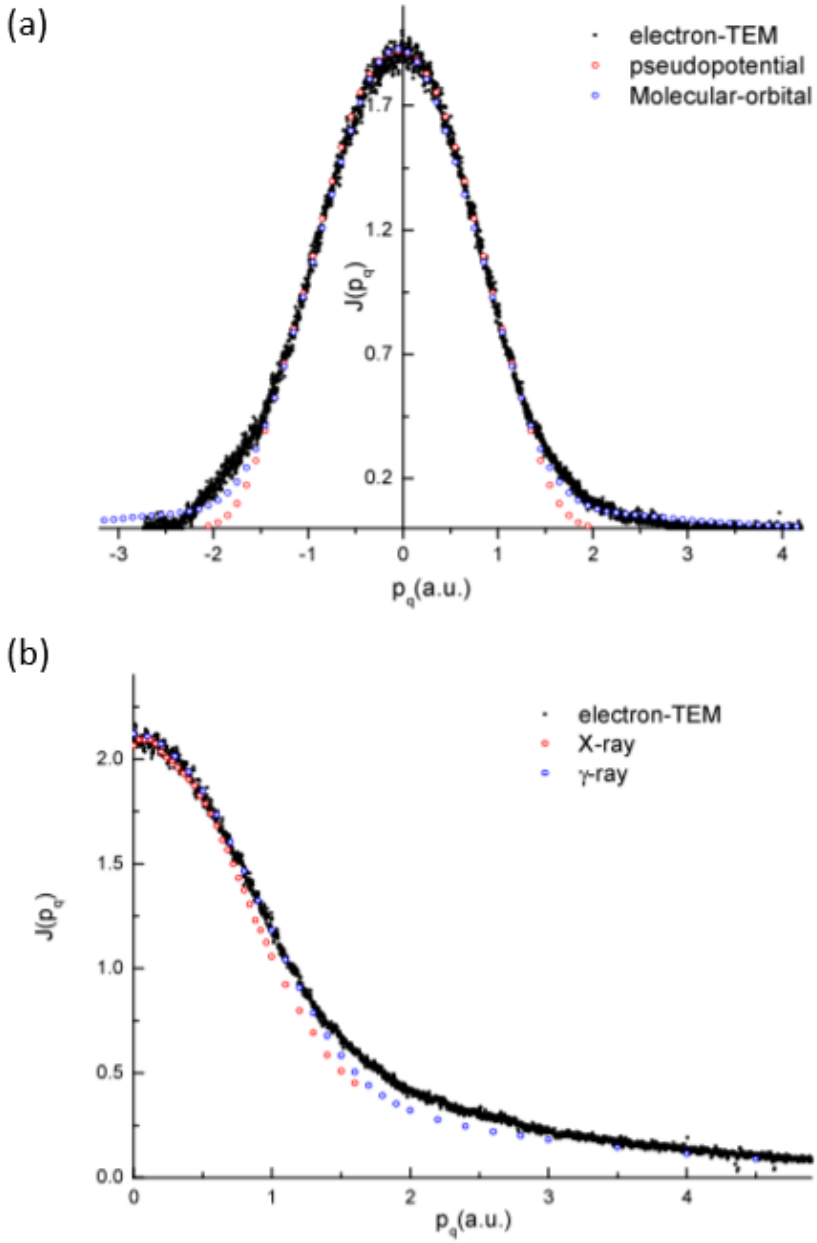


Figure 5.9: Valence, (a), and total, (b) Compton profiles of graphite obtained by Feng *et al.* [28] In (a), the TEM data is compared to theoretical calculations produced by Reed *et al.* [133] In (b), electron Compton profiles are compared to those obtained using X-rays (Bonse *et al.* [134]) and $\gamma$-rays (Tyk *et al.* [135]).

## 5.4 Compton spectra in STEM mode

Extraction of Compton profiles at high spatial resolution could, in principle, be possible using TEM in a scanning mode (STEM). Here, the electron beam can be focused to a spot, so that Compton scattering occurs from only a small region of the sample. With an aberration-corrected STEM the size of the electron beam is comparable to an individual atom, which enables element specific information. This is useful for analysing materials that contain more than one element, such as the transition metal dichalcogenides (TMDs) investigated in this thesis (Chapter 2). However, due to the convergence of the beam, a spread in primary electron momentum is obtained (as opposed to minimal momentum spread in a parallel electron beam used in previously described Compton scattering experiments). In order to study the effect of the momentum spread and feasibility of these measurements, Compton profiles representing electron scattering in an amorphous carbon film were modelled and compared to preliminary measurements carried out in a JEOL 2100F TEM using a convergent electron beam at 200 kV.

### 5.4.1 Modelling of the Compton profile obtained in STEM mode

First, consider a STEM electron beam at normal incidence to the specimen. Due to the spread in the primary electron momentum, the measured Compton profile can be thought of as a sum of component Compton profiles originating from distinct momentum transfer values. The spread of the electron momentum can be represented by a circle of radius R in diffraction space, as shown in Fig 5.10. In order to account for a range of scattering vectors contributing to the measured Compton profile, the following modelling method was applied:

1. A square grid filling a circular STEM probe was constructed. The grid points are spaced 0.3 $\text{nm}^{-1}$ apart and have coordinates $(x_i, y_i)$, measured from the centre of the probe.

2. Each grid point represents a distinct scattering vector $q_i$, the length of which is defined as $|q_i| = \sqrt{(q_c - x_i)^2 + y_i^2}$, where $q_c$ is the magnitude of the scattering vector measured from the centre of the STEM probe (see Fig. 5.10).

3. Using $\phi = q\lambda$ (where $\lambda$ is the electron wavelength) and equation 5.1.6, the energy loss of Compton profile peaks $\Delta T_p$ originating from distinct scattering vectors were found.

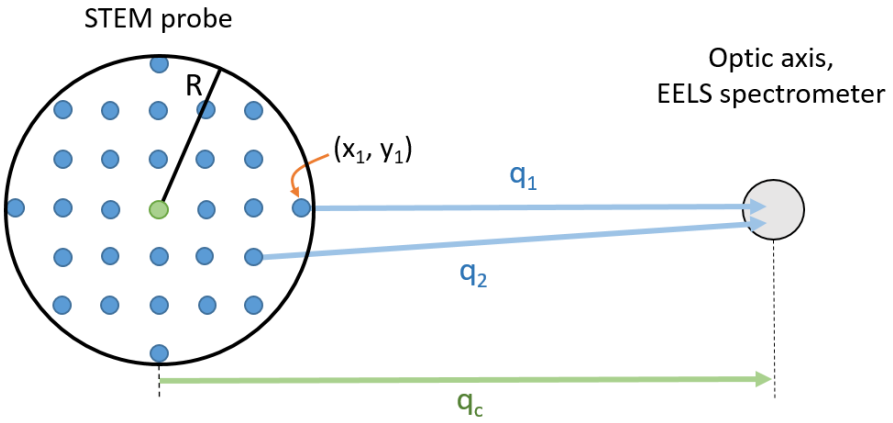


Figure 5.10: Schematic representation of Compton scattering in diffraction space in STEM mode. The circle of radius R defines the momentum spread of the STEM probe. It can be divided into a set of points, each of which corresponds to a distinct scattering vector, $q_i$, and creates a component Compton profile. The latter are then summed to create a lineshape of the full Compton profile.

4. Starting from the $J(p_z)$ curves obtained in previous experiments with a parallel electron beam in TEM mode (Section 5.3), the Compton lineshape for each grid point was generated using equation 5.1.7. In particular, for scattering vectors representing low and high momentum transfer regimes, the $J(p_z)$ profiles measured at $q = 12.3$ nm$^{-1}$ and $q = 14.9$ nm$^{-1}$ were used (see Figure 5.8).

5. The intensity contribution of each component Compton profile was considered to be proportional to $\frac{1}{q_i^4}$ [136].

6. Finally, the component Compton profiles were summed to give a lineshape of the full Compton profile.

Note that the algorithm assumes single Compton scattering events and ignores any potential contributions from diffracted and thermal diffuse-scattered electrons. The calculation was carried out using Python (Appendix A.1), testing two different STEM probe momentum spread values, 3.9 nm$^{-1}$ and 9.7 nm$^{-1}$. These correspond to STEM probe convergence semi-angles of 4.9 mrad and 12.3 mrad at 200 kV respectively. The models for the Compton spectra in both low and high momentum transfer regimes were obtained and are shown in the Figs. 5.11 and 5.12. At higher convergence angle, the Compton peaks decay slower on the high energy loss side and are more asymmetric than the peaks modelled at low convergence angles. This arises due to wider energy loss range spanned by the former and gradual stretching of the component Compton profiles representing increasing scattering vector.

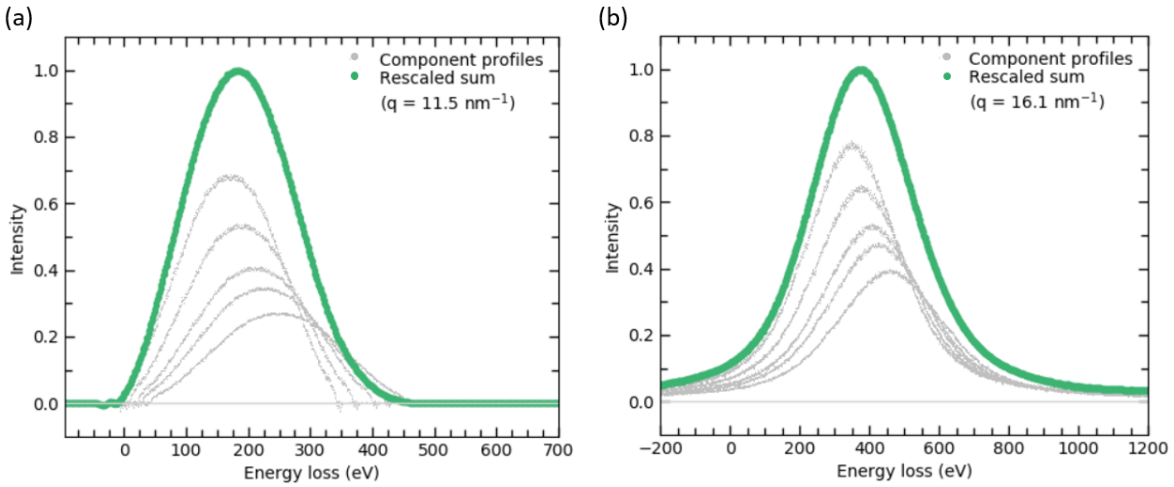


Figure 5.11: Full Compton profiles (in green, scaled down for clarity) in low and high momentum transfer regimes, (a) and (b) respectively. Modelling was carried out considering 4.9 mrad STEM probe convergence semi-angle and 3.9 nm$^{-1}$ momentum spread. 5 out of 109 component profiles considered in both regimes are represented in grey. Note non-zero intensity values in the negative energy loss range, which are unphysical and arrise due to imperfections in the model.

### 5.4.2 Model comparison with experimental data

The model described in section 5.4.1 was tested on a dataset obtained using a convergent electron beam in a JEOL 2100F at 200 kV. The dataset contains measurements representing Compton scattering at primary electron momentum spread values of 3.9 nm$^{-1}$ and 9.7 nm$^{-1}$ (i.e. 4.9 mrad and 12.3 mrad convergence semi-angles respectively) in both high and low momentum transfer regimes. The momentum spread values were controlled by changing the size of the condenser lens aperture.

The comparison between the measurements taken at a 4.9 mrad convergence semi-angle and the expected Compton lineshape is presented in Figs. 5.13(a) and 5.13(b). The peak intensity of the simulated and experimental Compton profiles were normalised for direct comparison. In both low and high momentum transfer regimes, the model Compton lineshapes show similar gross features to the ones measured experimentally. However, it consistently underestimates the Compton peak positions by approximately 25-35 eV. This could occur due to the breakdown in the small angle approximation (equation 5.1.6) and insufficient detail in the scattering process described in the model. For instance, it assumes a point-like EELS spectrometer aperture, while realistically its finite width could allow a wider range of scattering vectors, which could further modify the Compton peak position. Furthermore, the model only considers the STEM bright-field disc, and does not take into account the full details of the diffraction pattern, which includes the amorphous carbon 'halos' and thermal

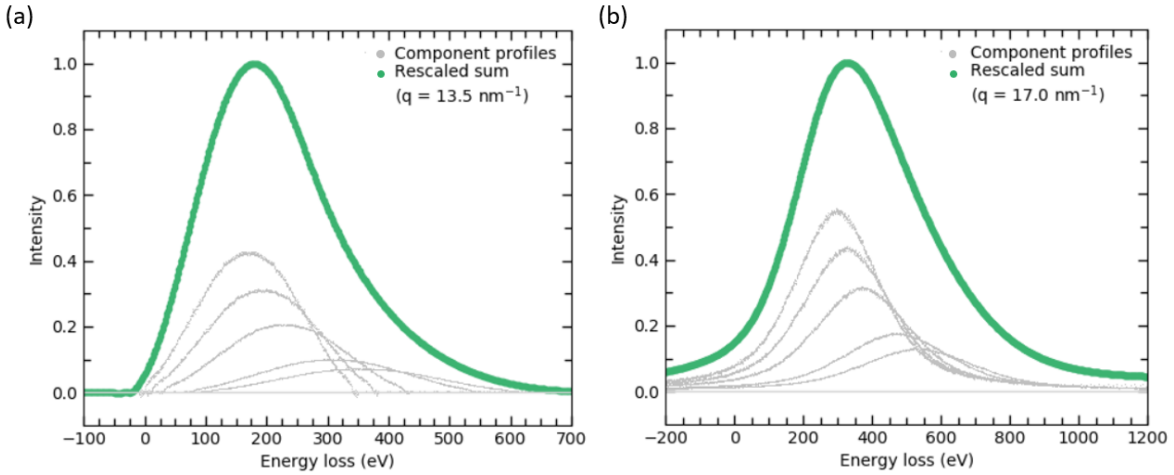


Figure 5.12: Full Compton profiles (in green, scaled down for clarity) in low and high momentum transfer regimes, (a) and (b) respectively. Modelling was carried out considering 12.3 mrad STEM probe convergence semi-angle and 9.7 nm$^{-1}$ momentum spread. 5 out of 740 component profiles considered in both regimes are represented in grey. Note non-zero intensity values in the negative energy loss range, which are unphysical and arrise due to imperfections in the model.

diffuse scattering. Also note that in the low momentum transfer regime (Fig. 5.13(a)), the inconsistencies beyond ≈283 eV energy loss arise due to the presence of the carbon K edge and Compton scattering contribution from core electrons which is not accounted for in the model. The opposite occurs in the high momentum transfer regime (Fig. 5.13(b)), i.e. the high energy loss side of the modelled Compton peak is a closer match to experimental data but the region up to the carbon K edge is overestimated. Here, the model assumes the contribution from core electrons, which experimentally is not present.

The measurements and modelled Compton peaks at 12.3 mrad probe convergence semi-angle are shown in Figs. 5.14(a) and 5.14(b). As in experiments at 4.9 mrad convergence semi-angle, there is a mismatch between the predicted and measured positions of the Compton peaks; however, it is more prominent at 12.3 mrad semi-angle and spans a range of approximately 30-90 eV.

Even though the modelled Compton spectra deviate from the experimental spectra (particularly with respect to their peak positions), feasibility of the Compton profile extraction at high spatial resolution via STEM can still be tested. Generally, for the technique to be useful, the experimental Compton profiles must be able to measure changes in the $J(p_z)$ profiles arising from bond anisotropy in a given crystal. This implies that for an amorphous carbon film, which represents an isotropic system, the difference between the $J(p_z)$ profiles obtained using both parallel and convergent electron beam has to be smaller (ideally neg-

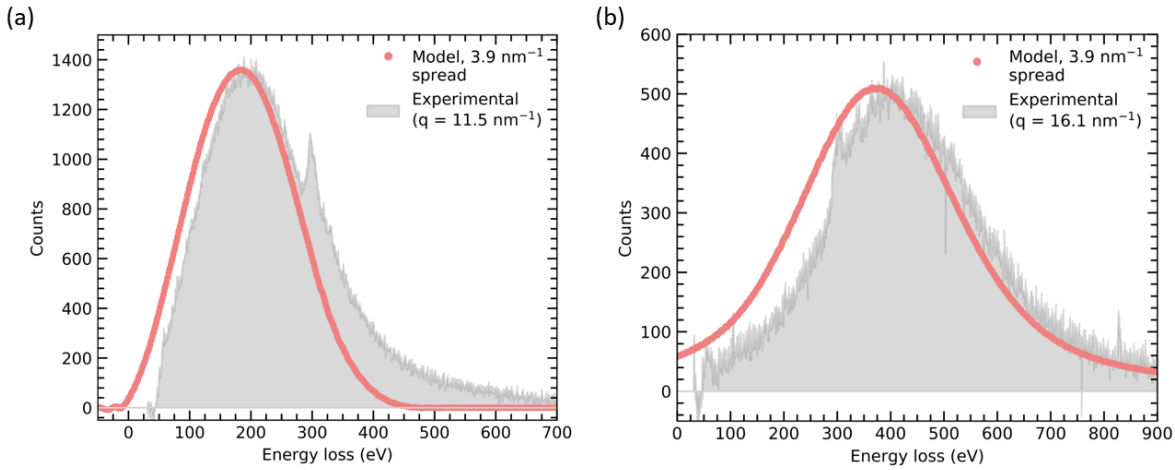


Figure 5.13: (a) compares the predicted (pink) and experimental (grey) Compton lineshape in the low momentum transfer regime (q=11.5 nm$^{-1}$, measured at the peak). (b) compares the lineshapes in the high momentum transfer regime (q=16.1 nm$^{-1}$, measured at the peak). The experiments and modelling were carried out considering a probe momentum spread of 3.9 nm$^{-1}$.

ligible) than the difference between the $J(p_z)$ profiles reflecting anisotropy in an equivalent crystalline system such as graphite. It is also important to note that 1 Å atomic resolution in aberration-corrected STEM is reached using an electron probe converging at 31 mrad semi-angle at 200 kV, giving a much higher momentum spread value than those studied in this section. Although this rules out element specific information, the modelled Compton profiles can sill give an indication whether extraction of the Compton profile at slightly coarser length scales can be pursued.

For this reason, the modelled Compton profiles in the energy loss and intensity scale were first converted into $J(p_z)$ profiles and compared to the initial $J(p_z)$ profiles used to model them. These are represented in Figs. 5.15(a) and 5.15(b), corresponding to low and high momentum transfer regimes respectively. The modelled Compton profiles resulting from a 9.7 nm$^{-1}$ STEM probe momentum spread do not fit the initial $J(p_z)$ curves, mostly due to their asymmetry and, therefore, cannot be considered, while those resulting from a 3.9 nm$^{-1}$ spread provide a closer match. However, further investigation of the difference profiles in Fig. 5.16(a) and 5.16(b) shows that for both momentum transfer regimes the difference between the Compton profiles at their peaks is $\approx 0.15 - 0.20$, which is substantially higher than the difference arising from bond anisotropy in graphite, as shown in Fig. 5.17 [34]. The diffraction limited resolution of the 3.9 nm$^{-1}$ probe is 6 Å; hence, the current state of the model indicates that sub-nm Compton profile extraction would not be possible using STEM microscope. A better model providing a more precise match to the experimental data could

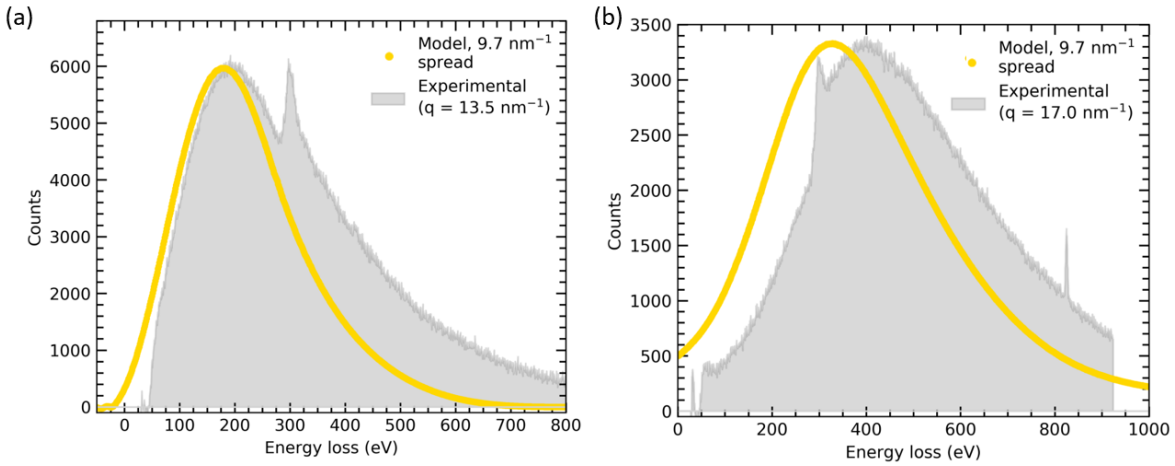


Figure 5.14: (a) compares the predicted (yellow) and experimental (grey) Compton lineshape in the low momentum transfer regime (q=13.5 nm$^{-1}$, measured at the peak). (b) compares the lineshapes in the high momentum transfer regime (q=17.0 nm$^{-1}$, measured at the peak). The experiments and modelling were carried out considering a probe momentum spread of 9.7 nm$^{-1}$.

potentially improve the results, but the changes are not expected to be significant enough to facilitate STEM measurements.

## 5.5 Conclusions

In this chapter, experimental conditions for improved data collection and analysis of electron Compton scattering were established using an amorphous carbon film. It has been shown that the impulse approximation is still appropriate in describing electron Compton scattering in the low energy transfer regime. Here, only valence electrons participate in scattering and provide momentum density profiles for which core electron background subtraction using computational techniques such as DFT are no longer required. It has also been demonstrated that even a crude plasmon background subtraction using a power law provides projected electron momentum density profiles that reasonably match the expected results. In addition, a method for plasmon background subtraction for samples resistant to electron beam damage has been outlined.

Further, possibility of the Compton profile extraction at high spatial resolution via STEM has been explored. Modelling of the Compton signal resulting from the primary electron momentum spread in a STEM probe has not provided a satisfactory match to experimental data. Also, further analysis has shown that the $J(p_z)$ curve extracted from the STEM Compton profile is not accurate enough for measuring bond anisotropy in a crystalline material

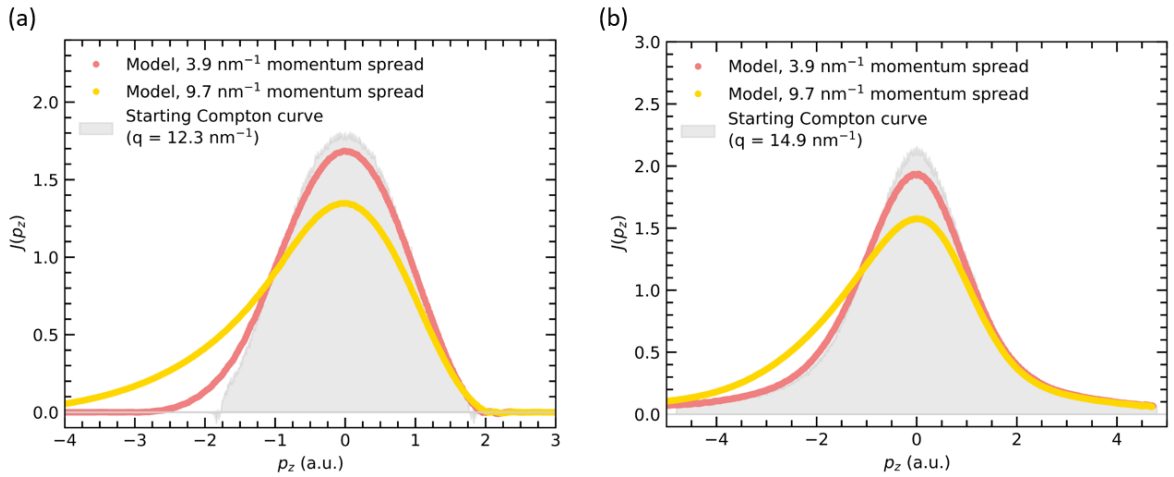


Figure 5.15: Comparison of the modelled Compton profiles to the initial Compton lineshape obtained experimentally using a parallel electron beam. (a) corresponds to the low momentum transfer regime and (b) to the high momentum transfer regime.

and extracting sub-nm Compton profiles.

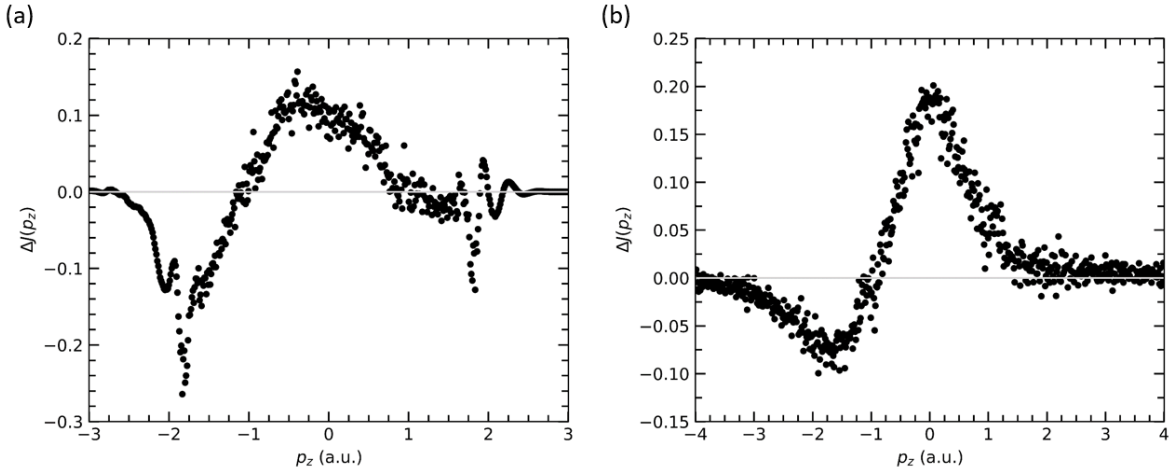


Figure 5.16: Difference profiles between the modelled $J(p_z)$ profiles using the 3.9 $nm^{-1}$ primary electron momentum spread and the original $J(p_z)$ profiles obtained using a parallel electron beam. (a) corresponds to the low momentum transfer regime and (b) to the high momentum transfer regime.

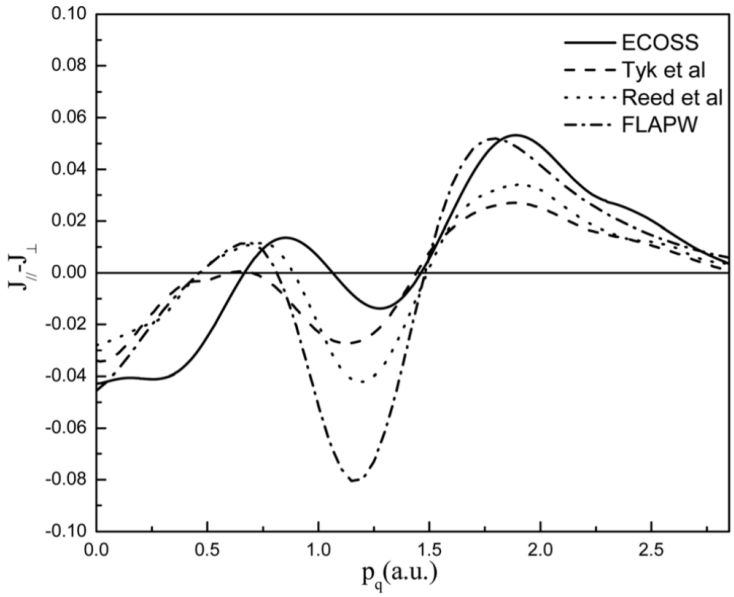


Figure 5.17: Difference $J(p_q)$ profiles reflecting bonding anisotropy along directions parallel and perpendicular to the basal plane in graphite. Experimental data (solid line) is compared to theoretical calculations (broken lines) [34, 133, 135]. Note that here $p_q \equiv p_z$.

# Chapter 6

# Electron Compton scattering in $WS_2$

Over the last 15 years, layered semiconducting transition metal dichalcogenides (e.g. $MoS_2$, $MoSe_2$, $WS_2$, $WSe_2$) have received a surge of attention due their interesting physical and chemical properties, which stem from their layer-dependent band structure. Bulk TMDs generally exhibit an indirect band gap, the magnitude of which increases with decreasing number of layers. However, crossover into the monolayer limit causes a band gap transition from indirect to direct. This band gap tunability together with excellent electrical transport properties make these materials attractive for applications in a wide range of devices such as transistors, light-emitters, gas sensors and photodetectors.

In this chapter, experimental electron Compton scattering measurements are carried out on monolayer, bilayer and bulk $WS_2$ samples with the aim to track changes in the projected electron momentum density as a function of the number of layers. Particular care is taken to establish optimal experimental conditions in order to preserve the sample integrity under the electron beam over the duration of a Compton measurement, as well as to determine any Compton artefacts arising from hydrocarbon contaminants on the sample surface.

## 6.1 Characterisation of $WS_2$

The chemical composition of the $WS_2$ sample was first confirmed via EDX, which shows peaks corresponding to tungsten and sulfur (Fig. 6.1). The spectrum also contains strong copper peaks from the TEM grid, as well as peaks from a number of contaminants – carbon, oxygen

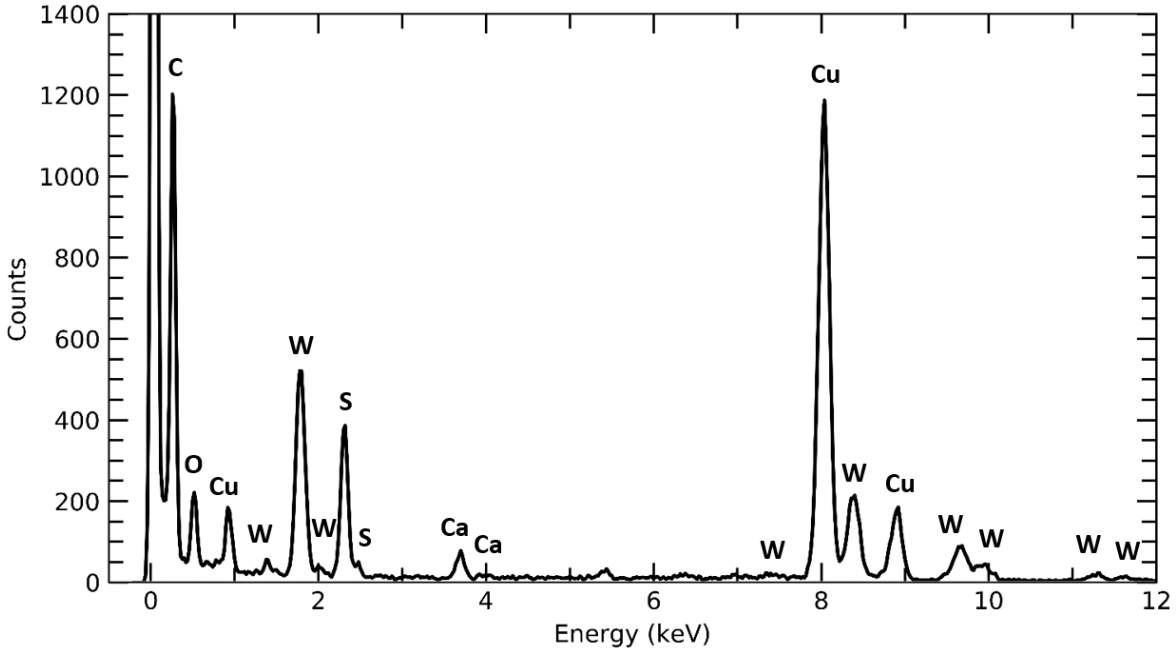


Figure 6.1: EDX spectrum of a $WS_2$ monolayer.

and calcium. The origin of calcium contamination (whether it is related to $WS_2$ growth, transfer, storage or handling) is not obvious; however, adsorption of carbon and oxygen species is expected. In particular, experimental investigations into long-term stability of TMD monolayers under ambient conditions have shown their tendency to adsorb hydrocarbons and susceptibility to oxidation due to presence of moisture in air (Fig. 6.2) [137]. Also note that a significant contribution to the carbon signal arises from the amorphous carbon support onto which $WS_2$ is deposited. The quality of $WS_2$ films was further investigated using HRTEM. Figs. 6.3(a) and 6.3(b) show high resolution micrographs of a monolayer $WS_2$ film reflecting its hexagonal atomic arrangement. The corresponding diffraction pattern for the domain is shown in Fig. 6.3(c). Due to the age of the sample, $WS_2$ surface contains a relatively high amount of carbon species; however, the diffuse halo expected from amorphous carbon is only weakly present (and can only be seen on adjusting the greyscale) in the diffraction pattern due to the stronger Bragg scattering from heavy tungsten atoms in $WS_2$. The measurement of the $WS_2$ lattice parameter from the diffraction pattern gives a value of 3.2 Å (the distance between the transmitted beam and the $(10\bar{1}0)$ reflection is 3.5 $nm^{-1}$), which closely matches the expected value of 3.16 Å for a monolayer [89]. Therefore, despite the age of the samples, the structure of $WS_2$ is well preserved. Analogous HRTEM images and a diffraction pattern for a $WS_2$ bilayer are shown in Fig. 6.4. Here, a moiré pattern forms due to a misalignment between the two layers of $WS_2$, which is indicated by the presence of 'pairs' of Bragg spots in the diffraction pattern (Fig. 6.4(c)). The angle between a pair of Bragg spots shows a 17°

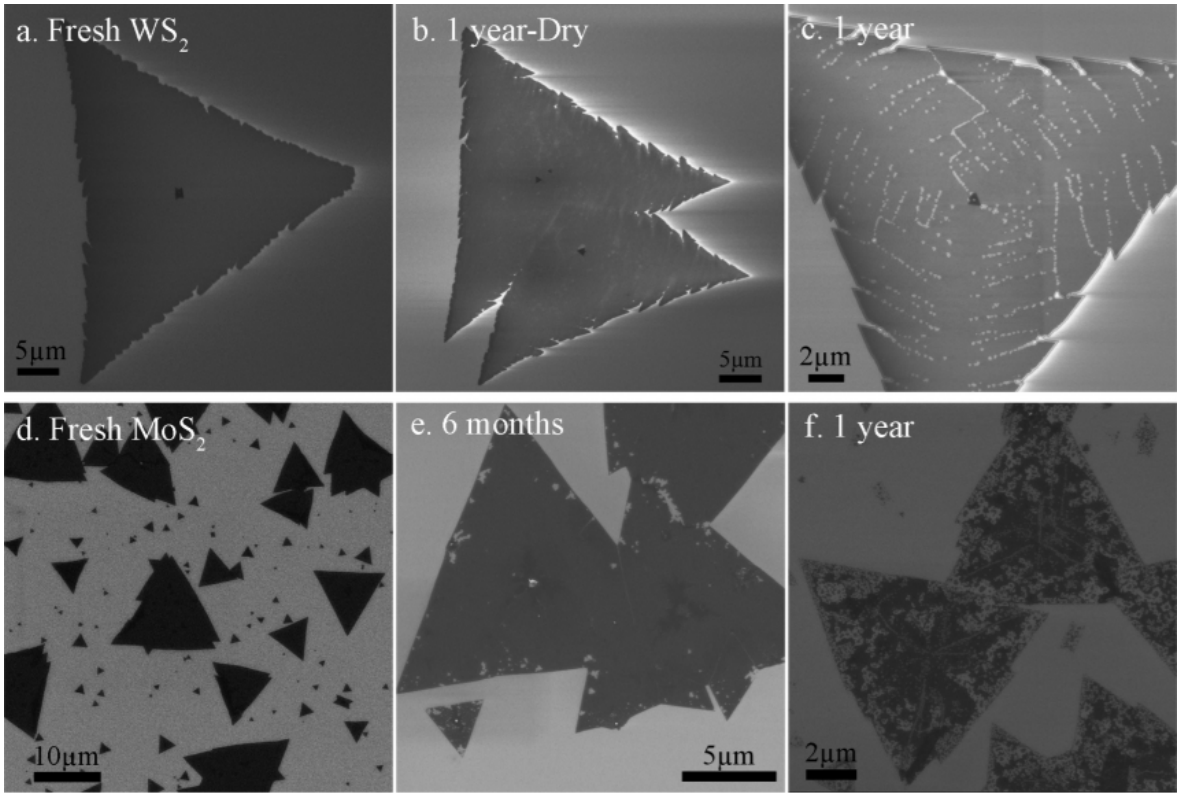


Figure 6.2: (a) Scanning electron micrographs of a fresh $WS_2$ grown on sapphire by MOCVD, (b) aged domain after 1 year storage in container with drying desiccant and (c) without desiccant, (d) fresh $MoS_2$ domains grown on $SiO_2$/Si substrate by MOCVD, and aged $MoS_2$ domains after (e) 6 months and (f) 1 year storage without drying desiccant respectively [137].

misalignment between the two $WS_2$ layers.

## 6.2 Electron beam damage studies in $WS_2$

One of the major factors affecting the quality of electron Compton scattering measurements is the sample's susceptibility to beam damage [32]. A range of unwanted electron irradiation artefacts such as defect formation, sputtering, sample heating and charging arise via two major direct damage-incurring mechanisms: (1) knock-on collisions between fast electrons and atoms, and (2) inelastic, predominantly electron-electron interactions [138]. The extent of the negative impact of these processes depends on a number of experimental parameters and sample properties such as primary beam energy, exposure time, current density, specimen chemical composition, thickness and local contamination levels. Hence, in order to preserve the sample's original condition, a lot of effort is put into optimisation of experimental methodology and, in some cases, development of protective coatings made of amorphous carbon or graphene [138–141].

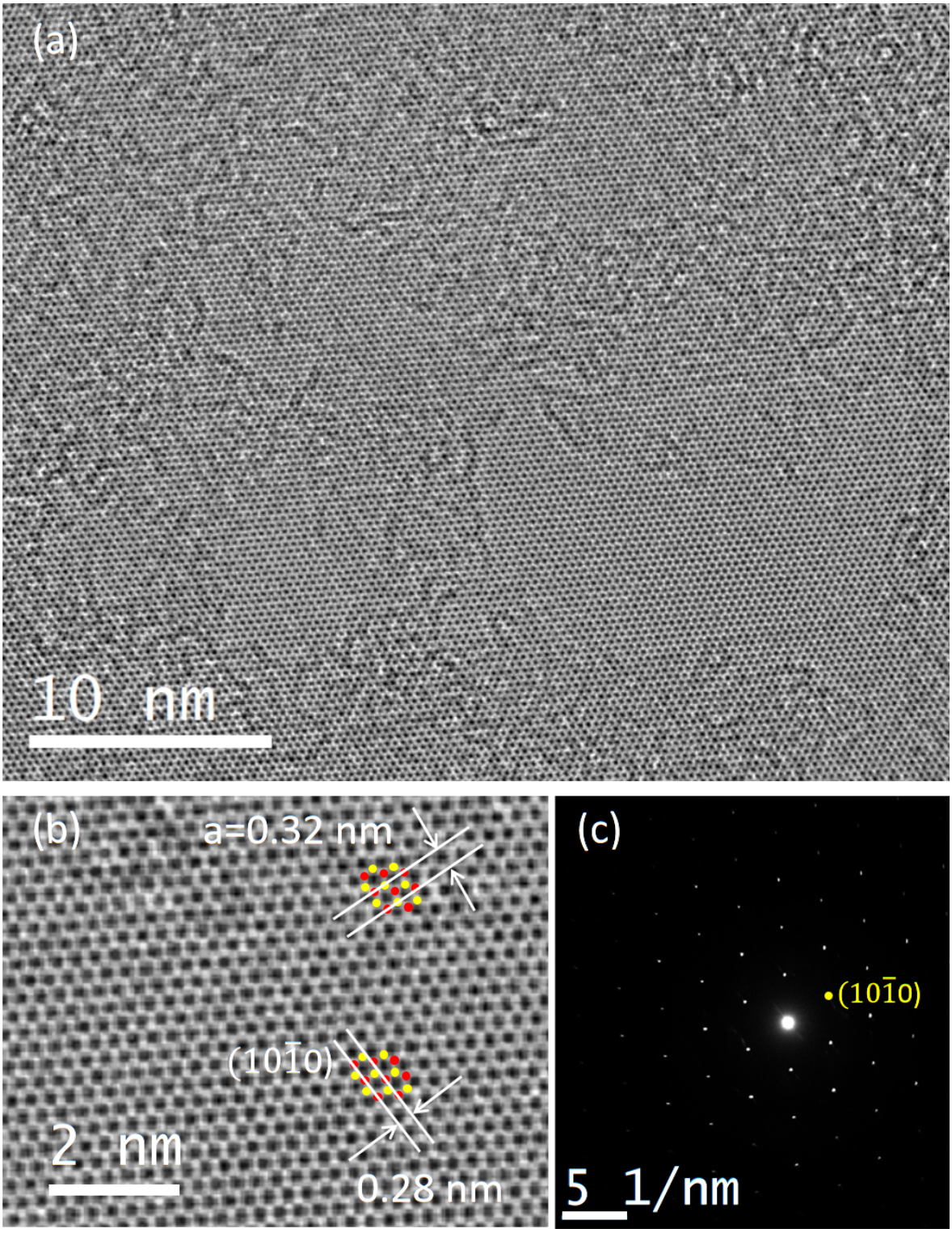


Figure 6.3: HRTEM images of a monolayer $WS_2$ domain under different magnifications in (a) and (b), and corresponding diffraction pattern in (c). The red and yellow dots in (b) are a guide to the eye for approximate atomic positions for tungsten and sulfur atoms.

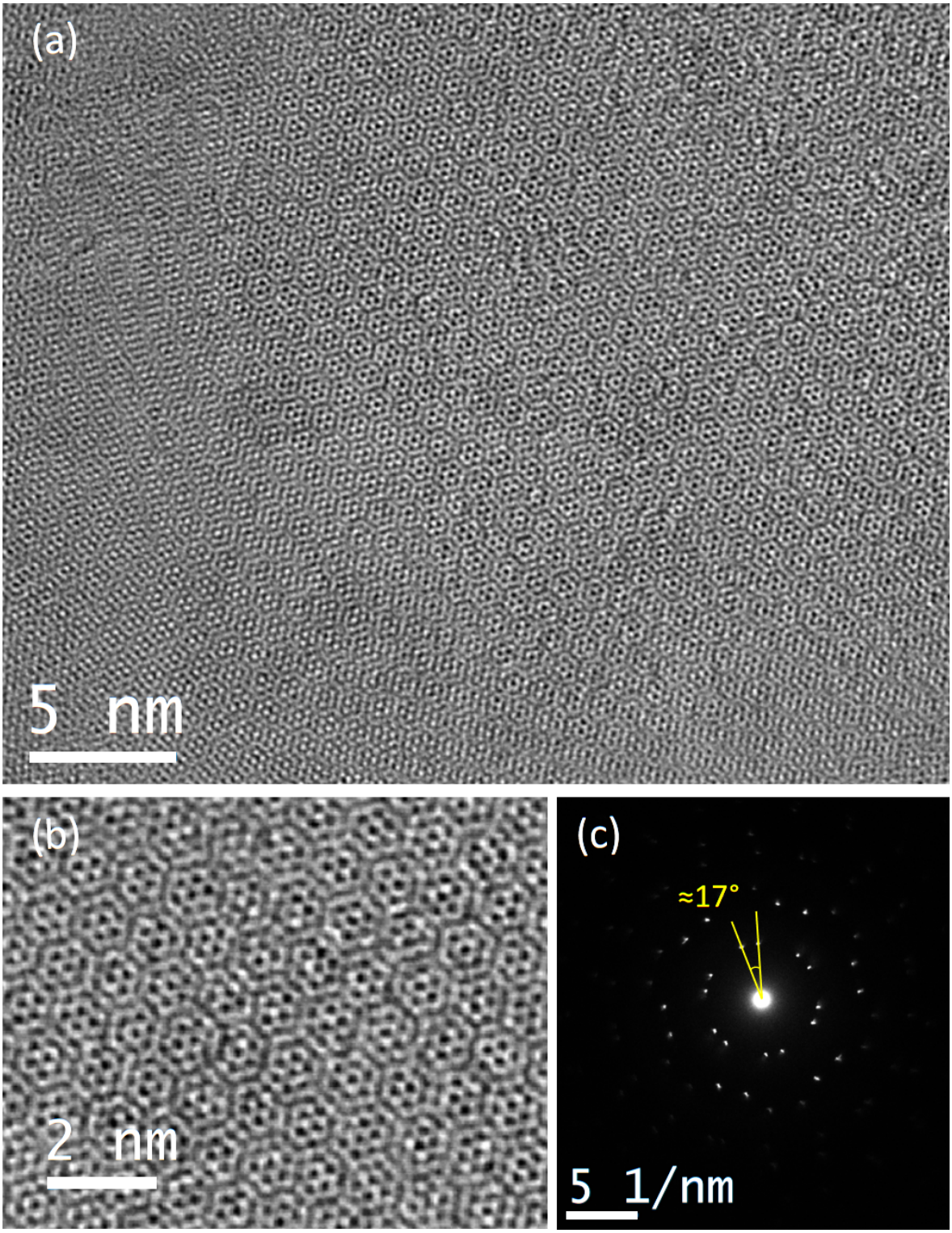


Figure 6.4: HRTEM images of a twisted bilayer $WS_2$ domain under different magnifications in (a) and (b), and corresponding diffraction pattern in (c).

In the 2D-TMD material family, electron irradiation damage mostly develops via knock-on collisions which generate vacancies. They occur predominantly in chalcogen sites due to a lower knock-on damage threshold compared to transition metal elements [142] and have the

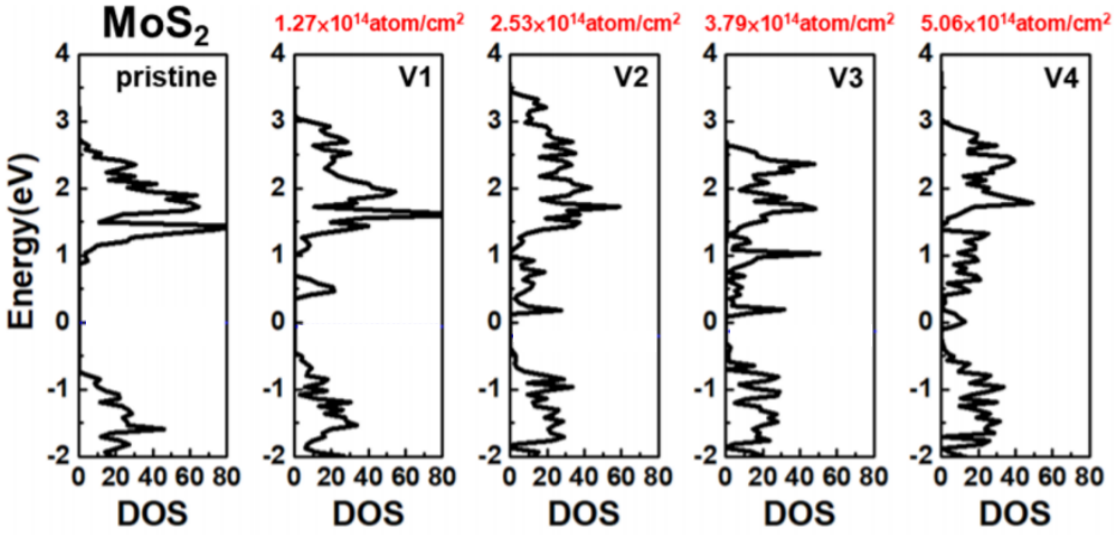


Figure 6.5: DFT calculations of DOS evolution with an increasing number of mono-sulfur vacancies in $MoS_2$ [142]. V1-V4 labels refer to 1-4 sulfur vacancies in a $3\times3\times1$ $MoS_2$ supercell respectively.

potential to alter the sample's mechanical, optical and electronic properties[1]. The impact of mono-sulfur vacancies on the DOS in 2D $MoS_2$ is illustrated in Fig. 6.5. Here, DFT calculations show that an increasing vacancy concentration reduces the band gap of the material and shifts its electronic behaviour from semiconducting to metallic. It can be assumed with reasonable confidence that similar effects would be present in $WS_2$ films; however, these changes would only occur at very high vacancy levels.

In order to preserve the sample structure to the highest level during Compton scattering measurements, establishment of the maximum measurement time at the available electron beam energy and current is of high importance. Hence, structural changes in $WS_2$ monolayer arising due to electron irradiation were tracked using HRTEM. The observed dynamics of defect formation is shown in Fig. 6.6, which consists of eight snapshots of the $WS_2$ flake taken over a duration of 105 seconds exposure. The beam voltage was 200 kV and both the condenser aperture size and beam spot size were identical to those used for Compton measurements. Fig. 6.6 shows that the first visible defects/defect clusters appear after 30 second exposure time; however, their density starts to increase only after a minute. Considering that the HRTEM images were acquired with a partially convergent electron beam, it can be inferred that Compton scattering experiments, which use parallel and therefore a less intense beam, can be safely carried out using 1 minute beam exposure time in addition to a few seconds

[1]Even though in this work electron irradiation artefacts are highly undesirable, defect generation in 2D materials via an electron beam can also be carried out deliberately in order to modulate their band gap, conductivity and carrier polarity for targeted applications [142, 143].

needed to set up the measurement.

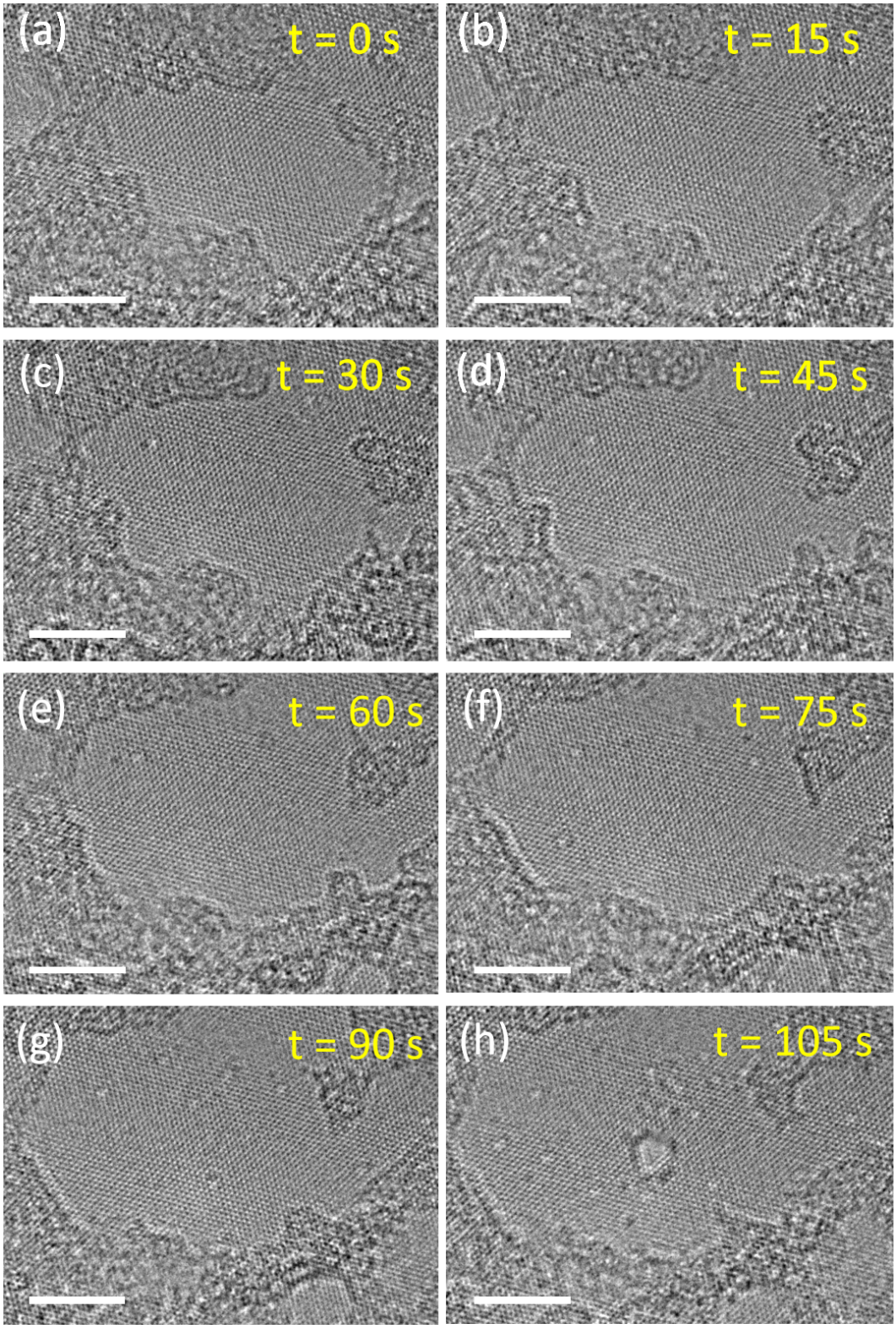


Figure 6.6: Defect formation in monolayer $WS_2$ as a function of electron beam irradiation time. Note the presence of hydrocarbon contamination on the sample. The scale bar represents 5 nm.

Deterioration of material structure can also be studied through electron diffraction, where the extent of irradiation damage is quantified by tracking the intensity decay of the diffraction spots or rings as a function of electron dose[2]. In the literature, it is typically measured by the critical electron fluence, at which the intensity of diffraction spots or rings is reduced to $1/e$ ($\approx 37\%$) of its initial value. Due to complications associated with the accurate measurement of electron fluence in the TEM used in this work, changes in the intensity of the diffraction spots were studied as a function of the beam exposure time. The electron beam settings were again matched to those used in the Compton measurements, and the resulting diffraction patterns together with the intensity decay are shown in Fig. 6.7. A $3\bar{3}00$ higher order diffraction spot, marked in Fig. 6.7(d), was selected for analysis in order to avoid artefacts from (i) variable intensity background from two major carbon contamination diffraction rings and (ii) any potential intensity afterglow of low order diffraction spots on the CMOS detector. Fig. 6.7(e) shows the intensity decay of the selected diffraction spot over the duration of 3 minutes. There is a slight increase in its value after 1 minute exposure, the cause of which is not obvious. Nonetheless, the measured intensity stays well above 37% of its initial value, which confirms the suitability of 1 minute-long Compton measurements (in fact Fig. 6.7(e) suggests that loss of long range crystallinity, as measured by selected area electron diffraction, only occurs after ≈2 minutes).

Finally, the integrity of the monolayer $WS_2$ sample over the duration of 1 minute beam exposure was studied via relative thickness measurement using EELS. The method uses the log-ratio algorithm, which measures the sample thickness $t$ in the units of local inelastic mean free path $\lambda$, using the zero-loss electron intensity $I_0$ and total transmitted intensity $I_t$ captured in the EELS spectrum, i.e.:

$$\frac{t}{\lambda} = \ln\left(\frac{I_t}{I_0}\right). \tag{6.2.1}$$

The output $(t/\lambda)$ of the relative log-ratio algorithm is therefore interpreted as the average number of scattering events per incident electron. Note that in practice $I_t$ can be replaced by the intensity of the low loss spectrum spanning an energy loss range of up to ≈100 eV, since this part of the EELS spectrum has the higher integrated intensity. Measurement of the relative $WS_2$ thickness before and after exposure to the electron beam for 1 minute yielded a decrease from 0.051 to 0.048. These values are larger than those expected for a

[2]Note that some materials are more sensitive to electron dose rate rather than accumulated dose [144]; however, the focus of this investigation is on damage under the experimental conditions used for Compton measurements, and therefore separate studies on the effect of dose rate on $WS_2$ damage were not carried out.

$WS_2$ monolayer due to carbon contamination. Hence, it can be inferred that the material is stable under the Compton measurement conditions, and the slight decrease in thickness can possibly be associated with contamination sputtering.

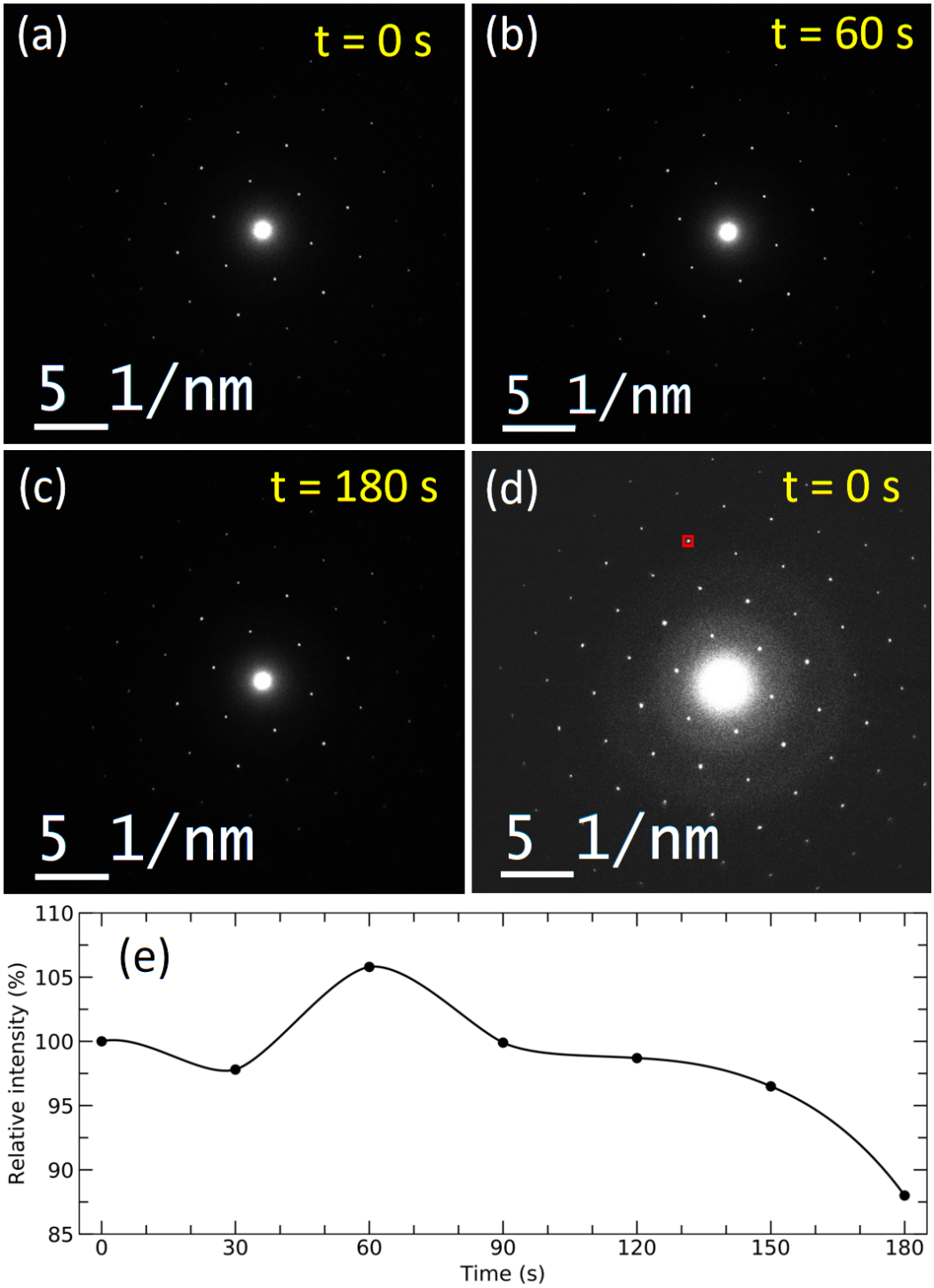


Figure 6.7: Diffraction patterns of $WS_2$ monolayer exposed to the electron beam for (a) 0 s, (b) 60 s and (c) 180 s. The diffraction spot used for damage analysis is marked on the pattern in (d), which is digitally enhanced in order to reveal the weaker intensity contribution from diffraction rings of amorphous carbon. The resulting intensity fluctuation of the selected spot over the duration of 3 minutes is shown in (e), where the black line is a guide to the eye.

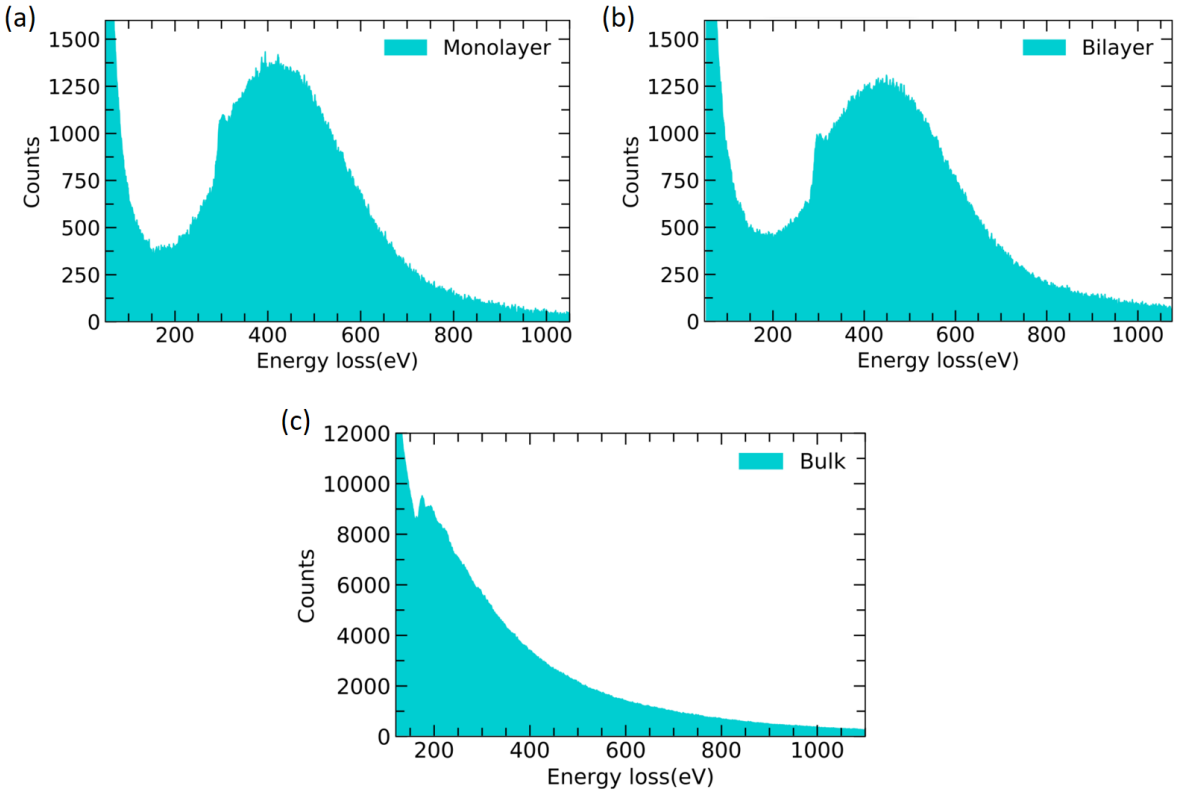


Figure 6.8: EELS spectra containing Compton peaks for monolayer (a) and twisted bilayer (b) $WS_2$ samples. The spectra also contain a carbon K-edge with an onset at 284 eV due to hydrocarbon contaminants on the sample surface. The Compton peak in the bulk $WS_2$ sample (c) is severely suppressed due to dynamical electron scattering. The small peak with an onset at 165 eV is the sulfur L-edge.

## 6.3 Electron Compton scattering in $WS_2$

Electron Compton scattering measurements in monolayer, 18° twisted bilayer and bulk $WS_2$ samples were carried out as per directions outlined in Section 4.3 with the aim to capture changes in the electronic band structure as a function of the number of layers (Sec. 2.2.1). In monolayer and bulk material, electron scattering along the Γ-K direction of the reciprocal lattice (i.e. $(10\bar{1}0)$ crystal planes) was measured, while in the twisted bilayer the scattering vector passed inbetween the two K-points of the individual $WS_2$ layers. The measured raw EELS spectra for the three crystals are shown in Fig. 6.8. Here, only the spectra for monolayer and bilayer samples contain prominent Compton peaks, while the Compton scattering signal in the bulk material is dramatically suppressed. This occurs due to dynamical electron scattering effects, which become more significant with an increasing sample thickness [106]. In particular, due to a short primary electron wavelength and small specimen thickness, the intersection between a fairly flat Ewald sphere and the broadened reciprocal lattice points, or "relrods", results in a large number of diffracted beams. In thicker samples, where electrons

can undergo diffraction multiple times, the Bragg beams become a potential source for further Compton scattering events and therefore produce a set of Compton peaks distributed along the energy loss axis in the EELS spectrum [136]. Collectively, they form a single Compton profile which can significantly deviate from the kinematical Compton profile in terms of its shape and position. Also, due to the inverse proportionality between the scattering cross-section and the fourth power of the scattering angle (or length of the scattering vector) [136], the contribution of the diffracted beams that are closer to the EELS aperture becomes increasingly higher. For this reason, multiple scattering effects will be more prominent on the low energy loss side of the measured Compton peak [136], introducing further deviations from its kinematical counterpart. Despite the efforts to reduce multiple scattering effects in bulk $WS_2$ by careful positioning of the primary electron beam and the EELS aperture with respect to the sample (described in Sec. 4.3), dynamical diffraction effects were unavoidable and the Compton profile remained concealed in the background of the EELS spectrum. Note that in principle diffracted beams in monolayer and bilayer $WS_2$ could also act as potential sources for Compton scattering; however, their intensity is at least two orders of magnitude lower than the intensity of the primary electron beam, and therefore their impact on the shape of the Compton profile can be considered negligible.

Furthermore, it is important to note that a significant fraction of the Compton signal in monolayer and bilayer $WS_2$ (Figs. 6.8(a) and 6.8(b)) may originate from amorphous hydrocarbon contaminants adsorbed on the surface of the material. Evidence for hydrocarbon contaminants can be seen in the HRTEM images in section 6.1 (Fig. 6.3), as well as the presence of a carbon K-edge in the EELS spectra. Their impact, however, can be minimised by looking at the difference in Compton profiles between samples (e.g. changes between mono- and bilayer $WS_2$), as shown further in this section.

Conversion of the Compton profiles, such as those in Fig. 6.8(a) and 6.8(b) into the projected electron momentum density of states $J(p_z)$ was carried out following similar methods as to those applied in the studies of amorphous carbon films (Chapter 5). In particular, the plasmon background was subtracted using a power law fit, and the contribution of the ZLP and the carbon K-edge was considered to be negligible across the high energy loss side of the Compton peak. The energy loss axis was then converted into the projected electron momentum scale using Eqn. 5.1.7. As mentioned in Sec. 1.2.1, conversion between electron counts and the projected electron momentum density scales is done indirectly by integrating the Compton profile to the number of electrons participating in scattering. In the case of $WS_2$, this becomes less well-defined due to the contribution of hydrocarbon contaminants

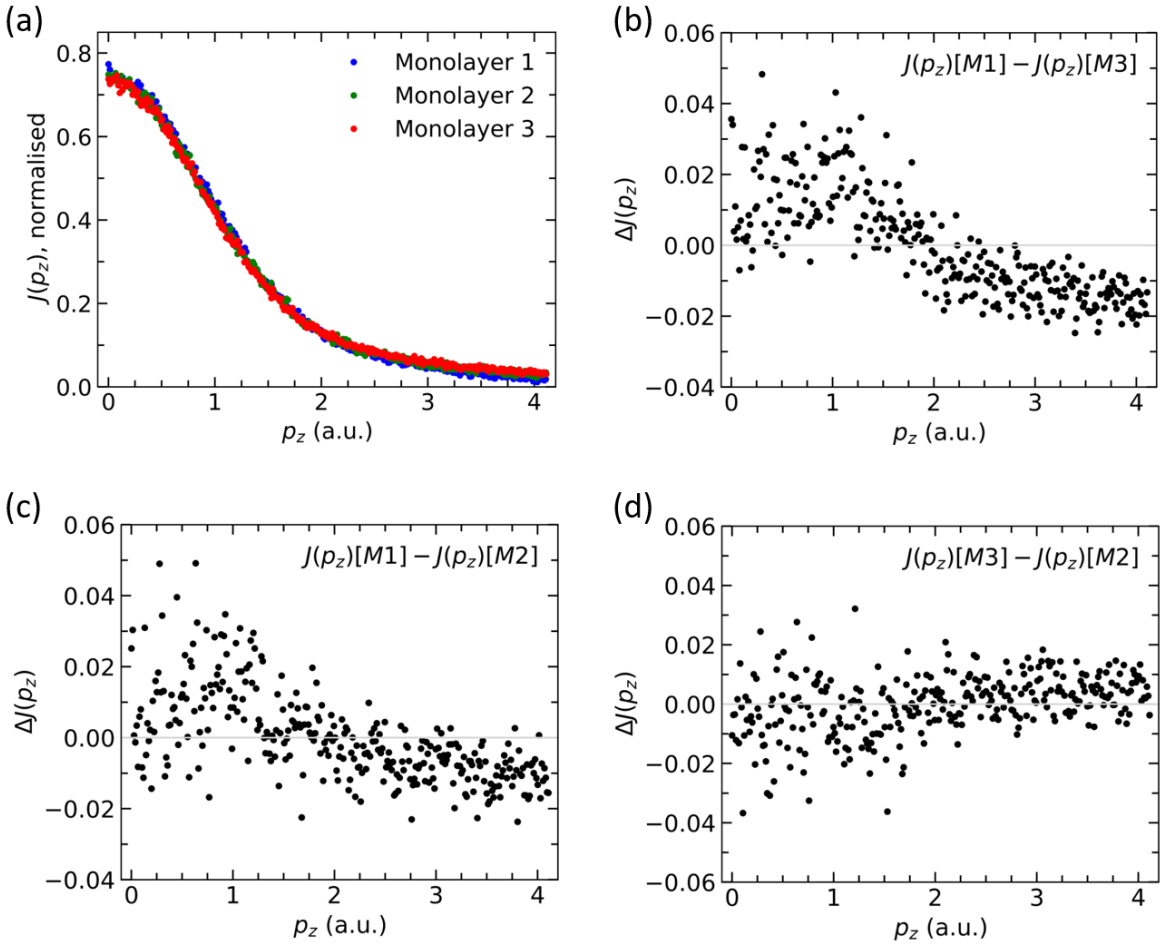


Figure 6.9: (a) Compton profiles J($p_z$) for different $WS_2$ monolayer flakes (M1-M3). The peak areas are normalised to 1. Their difference profiles are shown in (b), (c) and (d).

to the overall Compton scattering intensity. For this reason, the Compton profiles J($p_z$) for both monolayers and bilayers were integrated to 1.

In this work, three $WS_2$ monolayer flakes were studied via electron Compton scattering. Their corresponding J($p_z$) profiles are shown in Fig. 6.9(a). The curves strongly overlap, with the largest deviations occurring in the projected momentum range between 0 and 1 a.u. (Figs. 6.9 (b)-(d)). Here, the spectra are also the noisiest and the largest differences between them reach approximately 3% of the maximum Compton profile height. This value represents an upper limit of the systematic errors involved in the measurement for monolayers, which from Fig. 6.9(a) is seen to be highly reproducible. As for bilayers, two flakes were measured; however, the misalignment angles between them are different, i.e. in bilayer 1 it is 18°, while in bilayer 2 it is 12°. Also, due to non-ideal experimental setup procedures, the scattering vector in bilayer 2 is slightly off the optimal scattering direction, as shown in Fig. 6.10. The J($p_z$) profiles of both flakes and their difference are shown in Figs. 6.11(a) and 6.11(b) re-

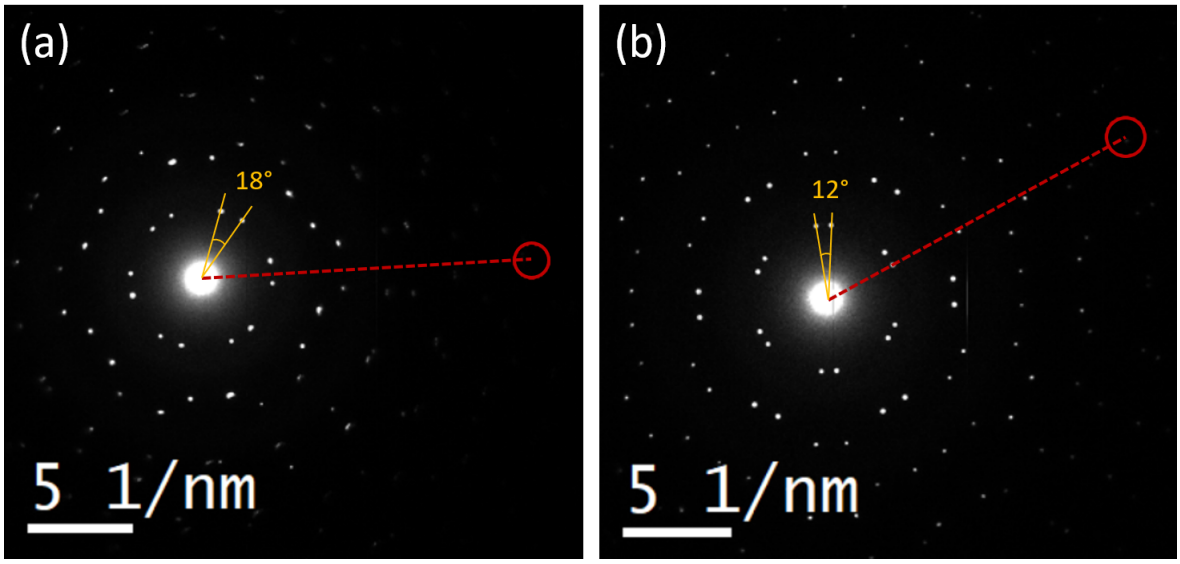


Figure 6.10: Diffraction patterns and Compton scattering setup for $WS_2$ bilayer flakes B1 and B2 in (a) and (b) respectively. The red circles mark the optic axis and the broken red lines indicate Compton scattering vectors.

spectively. The bilayers show slightly more pronounced differences around $p_z = 0$ compared to the monolayers. The differences are more systematic than random (cf. Fig. 6.9), which suggests it could be a real effect. This could occur not only due to inconsistencies with the scattering vector selection but also due to differences in interlayer coupling resulting from rotational misalignment. It is known that in bilayer van der Waals materials such misalignments create moiré superlattices, which can dramatically alter crystal properties due to the additional periodic potential felt by the electrons. For instance, in bilayer graphene with a twist angle of 1.05° and enhanced interlayer electron coupling, the usual linear dispersion of the Dirac cones of the two layers becomes flat leading to unconventional superconductiv-

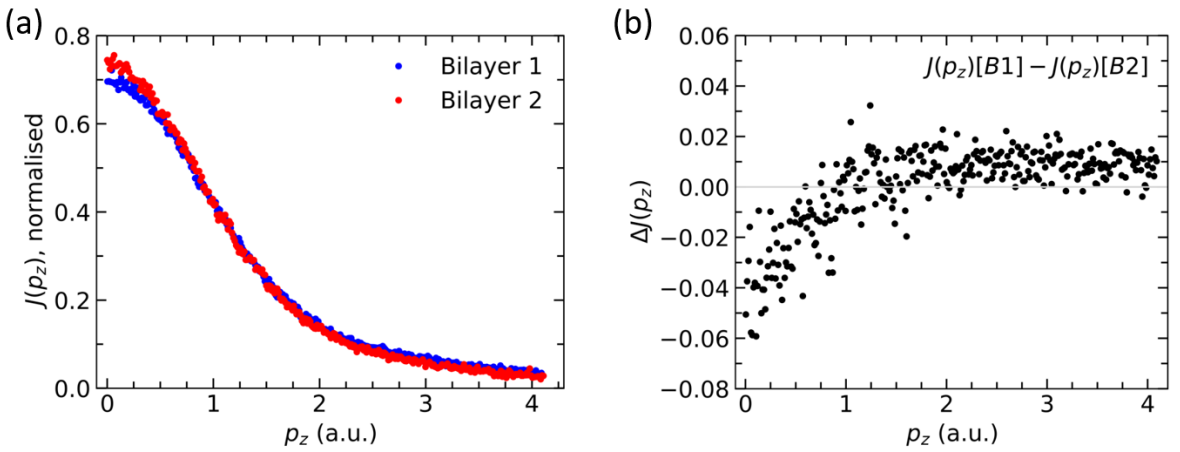


Figure 6.11: (a) Compton profiles $J(p_z)$ for two $WS_2$ bilayer flakes (B1, B2). The peak areas are normalised to 1. Their difference profile is shown in (b).

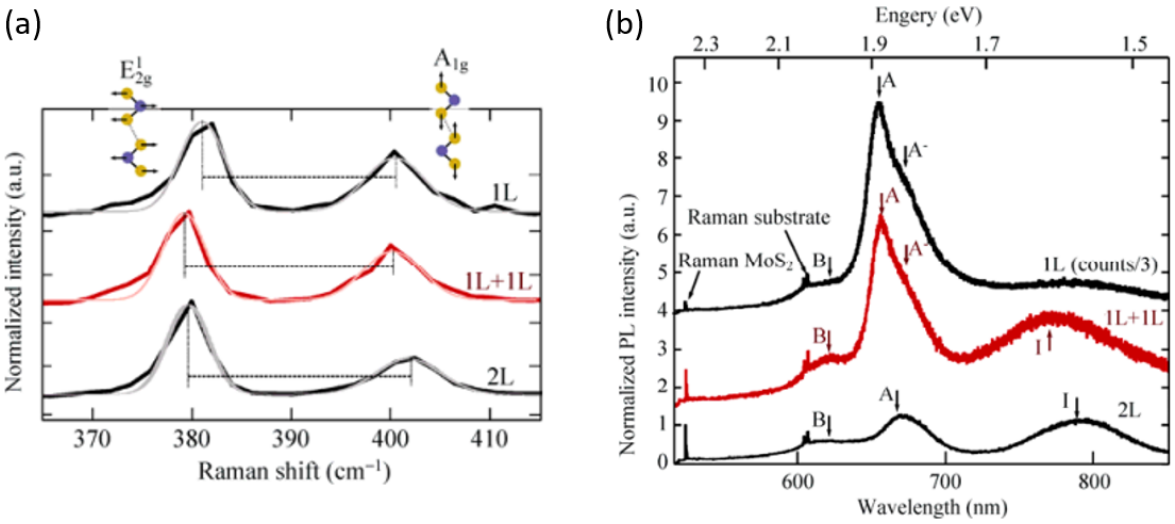


Figure 6.12: (a) Comparison of Raman spectra for monolayer (1L), bilayer (2L) and folded single-layer (1L+1L) $MoS_2$ samples. The thin lines superimposed on each spectrum represent Lorentzian fits to the experimental data, and the broken horizontal lines mark frequency differences between the $A_{1g}$ and $E^1_{2g}$ vibrational modes. (b) Comparison of PL spectra for monolayer (1L), bilayer (2L) and folded single-layer (1L+1L) $MoS_2$ samples. The arrows highlight the peaks associated with Raman emission in $MoS_2$ and the substrate, as well as B, A, $A^-$ and I excitons. Image adapted from [148].

ity in the material [145,146]. Similar electronic band structure distortions are predicted for TMD bilayers such as $WSe_2$, in which the top valence moiré band becomes almost flat at interlayer twist angles of up to about 5° [147]. However, these unusual physical phenomena occur when the material reaches extremely low temperatures (typically below 3 K). Also, it has been shown that interlayer rotational misalignment in bilayer TMDs may lead to weakened interlayer coupling, where the bilayer is formed by folding the monolayer [148]. Such structures can behave like single layer crystals. For instance, folded $MoS_2$ monolayer shows enhanced photoluminescence characteristic to single layer $MoS_2$, and the Raman spectrum with intermediate frequency difference between the $A_{1g}$ and $E^1_{2g}$ vibrational modes compared to the frequency differences corresponding to monolayer and perfectly stacked bilayer $MoS_2$ (Fig. 6.12). Due to the material growth and transfer methods applied in the production of $WS_2$ samples studied in this work, there is a significant amount of monolayer folding that is observed (Fig. 4.4(b)). Therefore, it could be assumed that certain bilayer flakes could suffer from reduced interlayer coupling and would produce Compton profiles similar to those of monolayers, as is observed in bilayer 2 in Fig. 6.11(a).

Further, the two $J(p_z)$ profiles corresponding to the M1 and B1 measurements of monolayer and bilayer $WS_2$ samples respectively are compared in Fig. 6.13(a). Their difference profile in Fig. 6.13(b) was expressed as a fraction of the monolayer Compton intensity at $p_z = 0$ in

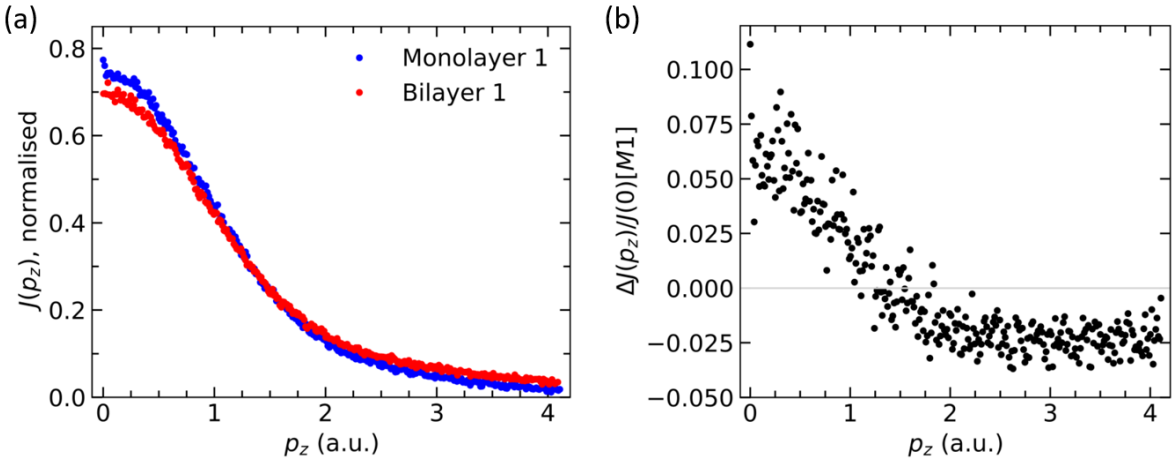


Figure 6.13: Compton profiles for monolayer and bilayer $WS_2$ (a) and their difference profile expressed as a fraction of the monolayer intensity at $p_z = 0$ (b).

order to eliminate scaling inaccuracies and facilitate easier comparison of the major profile features with subsequent theoretical calculations. Experimental data displayed in Fig. 6.13 shows that the Compton peak for the monolayer is taller and narrower than the one for the bilayer, with the largest deviations occurring in the $p_z$ range between 0 and 1 a.u. This implies that the electron density in the monolayer is more delocalised along the Γ-K direction.

In addition to the experimental measurements, electron momentum density profiles projected in the Γ-K direction for $WS_2$ monolayer, bilayer and bulk structures were also calculated using DFT by Prof S. Clark. The calculations were carried out using Castep electronic structure code, which uses a plane-wave pseudopotential method to solve a set of single-electron Kohn-Sham equations (Sec. 1.1) [149]. For $WS_2$, electron-ion interactions were described using an ultrasoft pseudopotential formalism, while the Perdew-Burke-Enzerhof (PBE) generalised-gradient approach was used to approximate electron exchange and correlation. The plane-wave basis set cut-off and k-point sampling for Brillouin zone integrations was converged to better than 1 meV/atom. Geometry optimisations were performed and considered converged when the forces were below 0.05 eV/Å. The calculated Compton profiles and the difference profiles are shown in Figs. 6.14(a) and 6.14(b) respectively. For ease of comparison with the experimental data, the calculated profiles were normalised to 1, while the difference profiles were expressed as a fraction of the monolayer and bilayer intensities at $p_z = 0$. Note that in the case of bilayer $WS_2$ the DFT calculations were carried out for an AB-stacked crystal, which does not have the interplanar rotational misalignment observed in the real sample.

DFT calculations show that the most significant changes in the projected electron momentum density of $WS_2$ crystals occur as the material transitions from monolayer to bilayer, in which

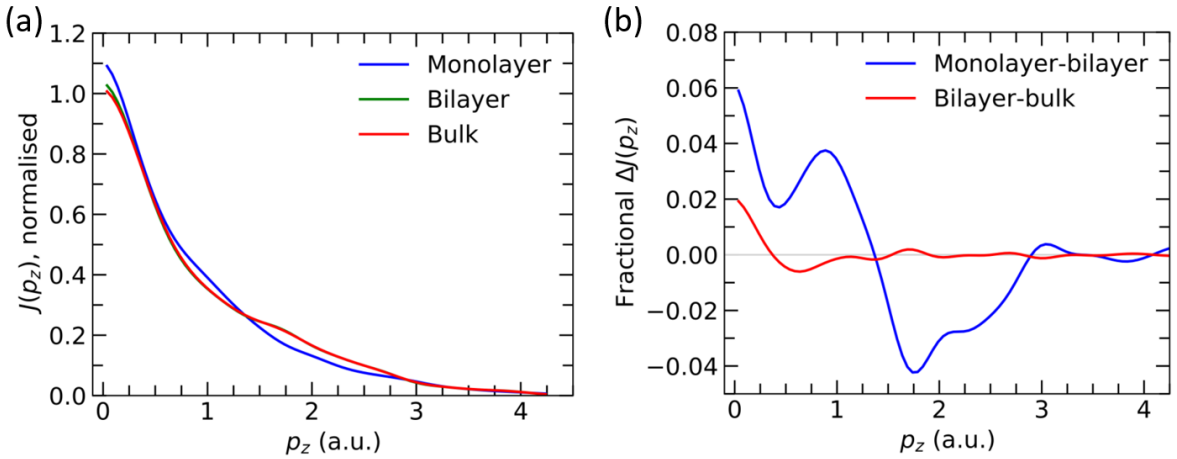


Figure 6.14: Compton profiles for monolayer, bilayer and bulk $WS_2$ calculated via DFT (PBE) (a) and their difference profiles (b). The latter are expressed in terms of fractions $(J(p_z)[M] - J(p_z)[B])/J(0)[M]$ and $(J(p_z)[B] - J(p_z)[Bk])/J(0)[B]$, where the markers M, B and Bk stand for monolayer, bilayer and bulk.

valence electrons become more localised. Further addition of $WS_2$ layers and a transition into the bulk state brings additional but less pronounced changes to the $J(p_z)$ profile at around $p_z = 0$. This implies a higher degree of electron localisation in bulk samples than in bilayers. As mentioned in Sec. 2.2.1 these layer-dependent changes in the electronic band structure are influenced by the chalcogen $p_z$ orbital contribution at the $\Gamma$ point.

Further comparisons of the experimental and theoretical data in Figs. 6.13(a) and 6.14(a) show that experimental profiles for both monolayer and bilayer $WS_2$ are considerably wider than predicted. Fractional $\Delta J(p_z)$ profiles in Figs. 6.13(b) and 6.14(b), on the other hand, show a fairly good match between the relative spectra intensities around $p_z = 0$, and the crossing point of the $p_z$ axis is at approximately 1.5 a.u. for both experiment and simulation. However, the simulation also predicts an intensity dip at ≈0.4 a.u., second crossing point at approximately 2.8 a.u. and a further levelling of the difference profile, which is not reproduced experimentally.

The differences between predicted and measured peak lineshapes could occur due to an additional Compton scattering contribution from amorphous hydrocarbon contamination on the surfaces of both samples that is not accounted for in the simulation. It can be approximately removed from the experimental data by taking the difference Compton profile, as in Fig. 6.13(b), which consequently shows a better match to the calculated difference profile. The impact of incomplete subtraction of the Compton signal originating from carbon contaminants can be further investigated by making appropriate adjustments to the theoretical difference Compton profiles. In particular, by adding or subtracting a small fraction

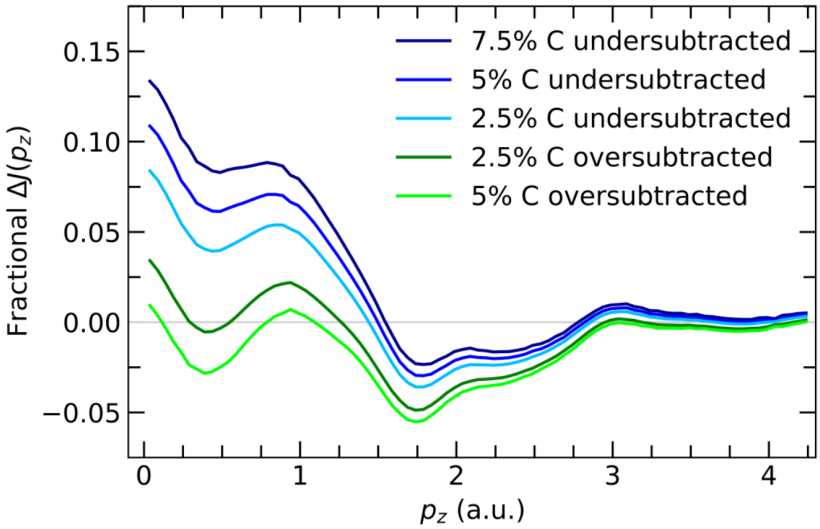


Figure 6.15: Theoretical difference Compton profiles adjusted for different levels of hydrocarbon contamination in monolayer and bilayer $WS_2$.

of the Compton profile measured for an amorphous carbon film (Fig. 5.8, $q = 14.9$ cm$^{-1}$), one can obtain difference profiles that reflect the experimental conditions more accurately. Such carbon-adjusted difference profiles are displayed in Fig. 6.15. Here, the blue-shaded profiles correspond to a fractionally higher carbon signal in monolayer $WS_2$ compared to the bilayer, which remains undersubtracted in the difference profile. The green shaded profiles represent the opposite situation, where the bilayers have a higher fraction of the Compton signal associated with carbon contamination. The adjusted difference profiles show a large intensity variation around $p_z = 0$, and an appearance of additional crossing points at low $p_z$ values for the profiles containing higher levels of carbon in the bilayer. The crossing point at $p_z \approx 1.5$ a.u. tends to move along the $p_z$ axis but stays within the random noise limit of the corresponding experimental data. At higher $p_z$ values, the differences between the $\Delta J(p_z)$ profiles gradually decrease.

In practice, it is not obvious how much carbon contaminants are accumulated on the surface of both monolayer and bilayer $WS_2$. However, it is reasonable to assume a uniform hydrocarbon accumulation rate with the progressive aging of the sample. This would imply that the Compton profile for monolayer $WS_2$ should contain a higher fraction of carbon-associated signal, and therefore a higher likelihood of Compton artefacts arising due to hydrocarbon profile undersubtraction. Comparing the adjusted difference Compton profiles in Fig. 6.15 with experimental data in Fig. 6.13(b), one can see a closer resemblance between theoretical predictions for the $\Delta J(p_z)$ curves corresponding to additional $\approx 2.5\% - 5\%$ hydrocarbon contribution in the monolayer, giving a good match of the profiles to the experimental data

in terms of intensity at $p_z = 0$, crossing point at $p_z \approx 1.5$ a.u. and the value of the minimum close to $p_z = 2$ a.u. The intensity dip at 0.4 a.u. is however largely unaffected at these levels of carbon contamination. Its absence in the experimental profile cannot therefore be explained by surface hydrocarbons.

## 6.4 Conclusions

In this chapter, experimental conditions for electron Compton scattering experiments in monolayer and bilayer $WS_2$ samples have been established, taking great care to avoid any sample damage associated with electron beam irradiation. The measured Compton profiles for a monolayer film have shown a high level of reproducibility, with an upper limit for systematic errors approximately 3% of the maximum Compton profile height. As for bilayers, slightly more prominent differences have been observed, which could have stemmed from imperfect experimental setup and reduced interlayer coupling in certain flakes.

Difference Compton profiles between monolayer and bilayer $WS_2$ flakes have been studied and compared to the corresponding theoretical calculations carried out via DFT. Experimental and theoretical difference profiles have shown a good match of the profile intensity close to $p_z = 0$ and the crossing point at $p_z \approx 1.5$ a.u.; however, the theoretical profile lineshape beyond 3 a.u. was not reproduced in the experiment. In addition, the effect of residual hydrocarbon contamination on the difference Compton profiles has been studied, showing quite significant changes in the difference profiles arising due to different fractional levels of carbon signal in monolayer and bilayer $WS_2$. An improved match to experimental data was found for difference profiles where the monolayer contained up to 5% excess carbon compared to the bilayer, which is consistent with the expected trends for our sample.

# Chapter 7

# Electron Compton scattering in $VO_2$

For over six decades, $VO_2$ has kept the attention of the scientific community due to its reversible metal-to-insulator transition, the mechanism of which is yet to be fully understood. The transition, which is also typically accompanied by tetragonal-to-monoclinic crystal lattice changes, occurs at approximately 68 °C and hence provides a lot of potential for applications in wide variety of optic and electronic devices.

In this chapter, experimental electron Compton scattering measurements are conducted on both metallic and insulating $VO_2$ phases with the aim to determine changes in the isotropic projected electron momentum density. Also, particular focus is placed on sample characterisation and establishment of optimal experimental conditions, under which the electron beam damage effects on the material throughout the Compton measurements are minimised.

## 7.1 Characterisation of $VO_2$

The chemical composition of the $VO_2$ sample was studied using EDX, which showed the expected peaks for vanadium and oxygen (Fig. 7.1). The spectrum also contains prominent peaks for copper and a weaker peak for carbon, which arise from the TEM grid bars and the amorphous carbon support. The spectrum further indicates presence of sodium, potassium and calcium contaminants. These elements are frequently found in ceramics and could have been introduced in the process of the $VO_2$ powder production. Furthermore, depending on the $VO_2$ powder production method, which is not known, the sample may also contain varying

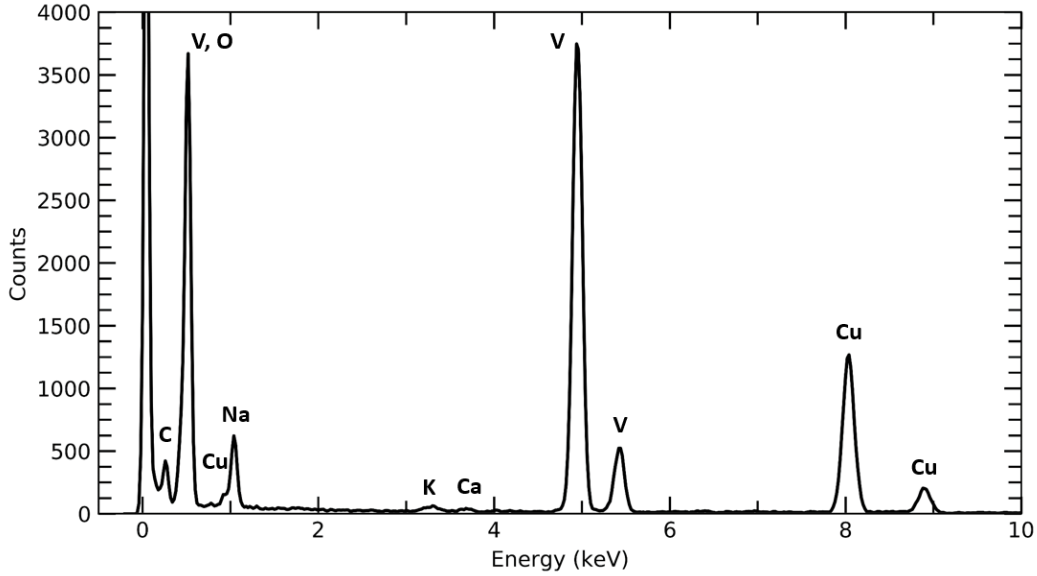


Figure 7.1: EDX spectrum of a $VO_2$ flake.

amounts of additional vanadium oxide phases such as $V_2O_3$ or $V_2O_5$. In order to establish the phase purity of the sample, the as-received powder was studied via X-ray diffraction using Bruker D8 ADVANCE diffractometer equipped with Oxford Cryosystems Cryostream 800 Plus cooler. The measurements carried out by Sam Thompson (Dept. of Chemistry, Durham University) are presented in Figs. 7.2(a) and 7.2(b). The measured spectrum of the sample displayed in black largely matches the library spectrum of the $VO_2$(M1) phase, which is displayed in blue in Fig. 7.2(a). However, Fig. 7.2(b) shows that the sample also contains a significant amount of $V_2O_3$, which is a low-temperature MIT material undergoing a trigonal-to-monoclinic phase transition at -113 °C (160 K) upon cooling [150]. It constitutes approximately 15% of the sample, but it is only a rough estimate as not all phases in the powder were characterised and the fits to data were not perfect.

Next, $VO_2$ flakes deposited onto a TEM grid (Sec. 4.4) were studied via HRTEM and electron diffraction, which revealed their highly polycrystalline nature, as shown in Fig. 7.3(a). It can be seen that the grains in the flake are of relatively small (nanometre) size and strongly overlap, thereby preventing momentum resolved electron Compton scattering measurements on single crystals. The diffracted beams in Fig. 7.3(b) almost form a ring pattern, from which the crystal structure of the $VO_2$ flake can be confirmed. At room temperature, $VO_2$ has a low-symmetry monoclinic lattice structure (M1) in which interplanar distances are defined by the equation:

$$\frac{1}{d^2} = \frac{1}{\sin^2\beta}\left(\frac{h^2}{a^2} + \frac{k^2\sin^2\beta}{b^2} + \frac{l^2}{c^2} - \frac{2hl\cos\beta}{ac}\right), \tag{7.1.1}$$

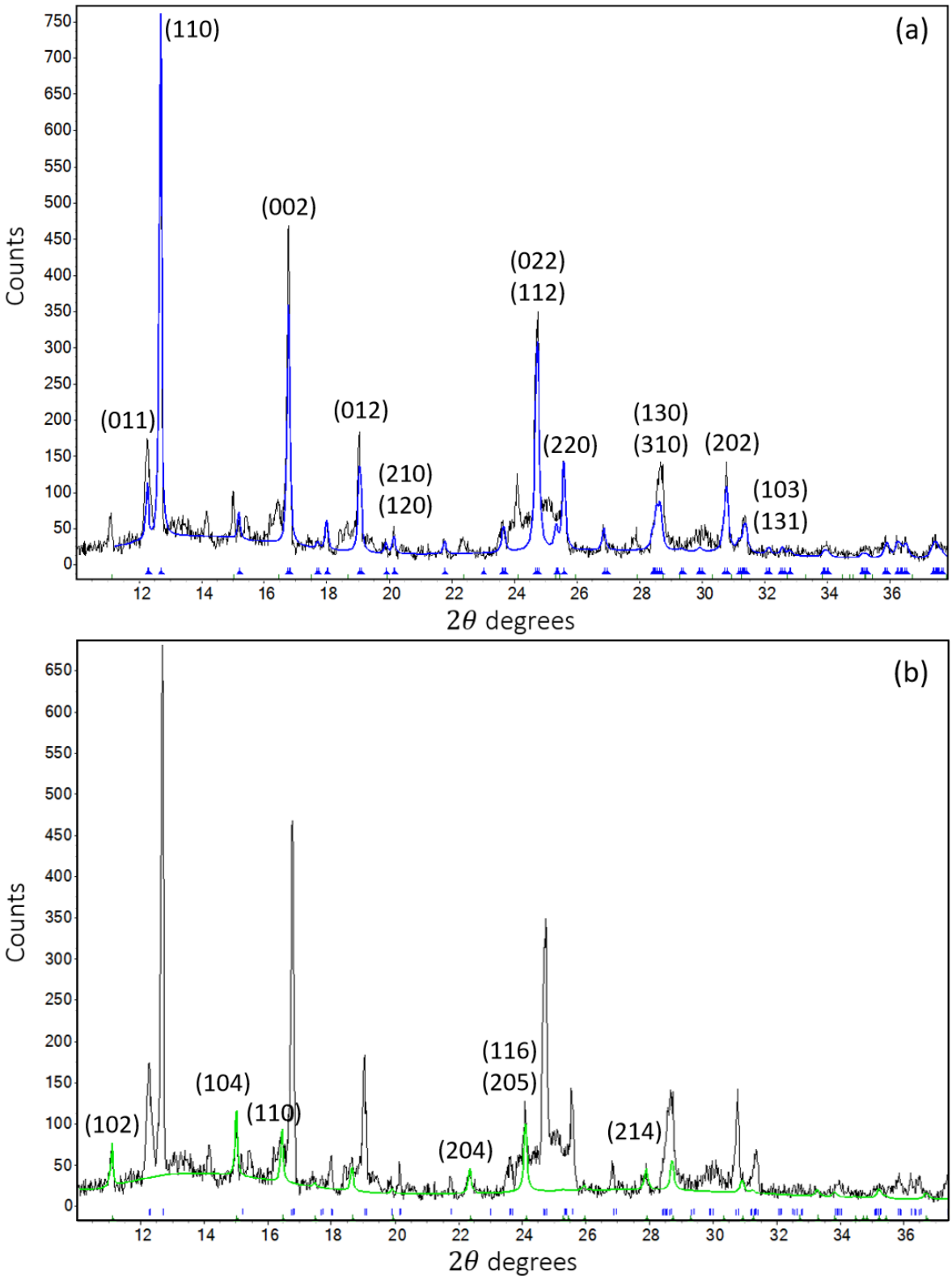


Figure 7.2: Room temperature XRD spectra for the $VO_2$ sample obtained from *Sigma Aldrich*. The measured data is displayed in black in both (a) and (b). The overlaid blue spectrum in (a) confirms that the sample is mostly composed of $VO_2$(M1) phase, which undergoes MIT at approximately 68 °C. The overlaid green spectrum in (b) corresponds to an impurity phase $V_2O_3$.

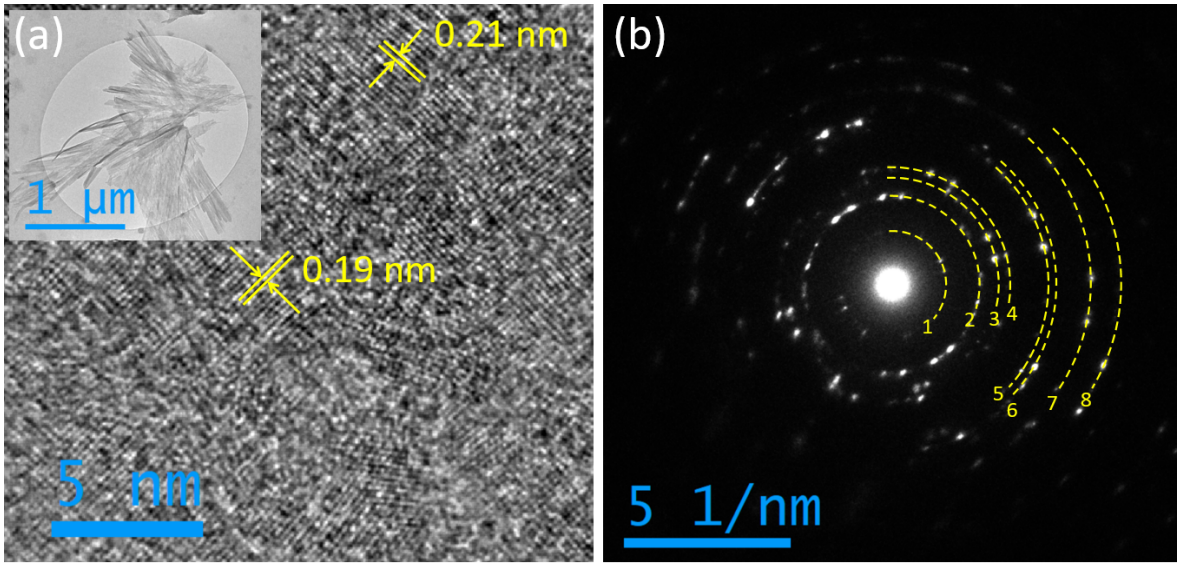


Figure 7.3: HRTEM image (a) and an electron diffraction pattern (b) of a $VO_2$ flake(s). The inset in (a) shows the morphology of several $VO_2$ flakes.

where $d$ is the spacing between crystal planes defined by (hkl) Miller indices. Lattice parameters are denoted by $a$, $b$, $c$ indices and $\beta$ is the angle between $a$ and $c$ vectors. For $V_2O_3$, which has trigonal lattice symmetry with lattice parameters $a = b = 4.95$ Å, $c = 14.00$ Å, $\alpha = \beta = 90°$, and $\gamma = 120°$, interplanar distances are defined as those for the hexagonal lattice[1], i.e.:

$$\frac{1}{d^2} = \frac{4}{3}\left(\frac{h^2 + hk + k^2}{a^2}\right) + \frac{l^2}{c^2}. \tag{7.1.2}$$

Equations 7.1.1 and 7.1.2 can be used to calculate interplanar distances for the given $VO_2$ and $V_2O_3$ unit cells. These can then be compared and matched to experimental values derived from the diffraction pattern. As usual, the distance $q$ between the transmitted and diffracted electron beams is an inverse of the interplanar distance $d$. The calculated and measured values of the $d$-spacings together with the corresponding crystallographic planes and phases are represented in Table 7.1. Here, majority of experimental interplanar distances (diffraction rings 2-8) are found to correspond to the predicted distances in $VO_2$ and $V_2O_3$ crystals, which also confirms that crystalline $V_2O_3$ impurities are imbedded in $VO_2$ matrix. The 1$^{st}$ diffraction ring, on the other hand, could not be indexed. As shorter lengths of the scattering vector imply larger unit cells, similar calculations were carried out for $V_2O_5$, $V_3O_7$, $V_4O_7$, $V_5O_9$ and $V_6O_{13}$ crystals but they did not provide satisfactory results.

[1]This applies to simple trigonal unit cells that share the same primitive vectors as the hexagonal lattice.

Table 7.1: Experimental interplanar distances measured from the diffraction pattern for the $VO_2$ flake in Fig. 7.3(b). These are matched to the corresponding crystallographic planes of $VO_2$ and $V_2O_3$ crystals.

| Experimental | | Calculation | | |
|---|---|---|---|---|
| Ring number | $d_{hkl}$ (Å) | Phase | hlk | $d_{hkl}$ (Å) |
| 1 | 6.2(1) | - | - | - |
| 2 | 3.7(3) | $V_2O_3$ | 102, 012 | 3.66 |
| 3 | 3.2(0) | $VO_2$ | 110 | 3.20 |
| 4 | 2.8(4) | $V_2O_3$ | 104 | 2.71 |
| 5 | 2.1(5) | $VO_2$ | 012 | 2.13 |
| 6 | 2.0(3) | $VO_2$ | 210, 120 | 2.03, 2.02 |
| 7 | 1.6(9) | $V_2O_3$<br>$VO_2$ | 116, 205<br>112, 022 | 1.70<br>1.65 |
| 8 | 1.4(9) | $VO_2$ | 130, 310 | 1.43 |

## 7.2 Confirmation of the MIT in $VO_2$ sample

As mentioned in Sec. 2.1.1, a reversible insulator-to-metal phase transition occurs in the monoclinic $VO_2$ phase (M1), which changes into tetragonal (R) at 68 °C upon heating. Due to a very short electron wavelength, the subtle structural changes in the lattice associated with MIT are difficult to confirm from electron diffraction patterns; hence, they were tracked via XRD measurements. A spectrum of the bulk powder taken at ≈177 °C (450 K) is shown in Figs. 7.4(a) and 7.4(b) in black. In Fig. 7.4(a) it is overlaid with the expected spectrum for the tetragonal $VO_2$(R) phase, which shows a good match to the data. The crystalline $V_2O_3$ phase represented by the green spectrum in Fig. 7.4(b) remains stable at high temperatures.

Further, the change in the $VO_2$ peak positions across a heating and cooling cycle spanning the temperature range between -73 °C and 177 °C (200 K – 450 K) is shown in Fig. 7.5. It represents a 'top-down' view of the diffraction patterns, where the "heat" of the colour corresponds to peak intensity in XRD spectra. The phase transitions, indicated by an abrupt shift of certain peaks, occur at approximately 65 °C (≈338 K) upon heating and at approximately 67 °C (≈340 K) upon cooling. The deviation between the two temperatures is a result of hysteresis in the different phase transition paths caused by strain or lattice defects [52].

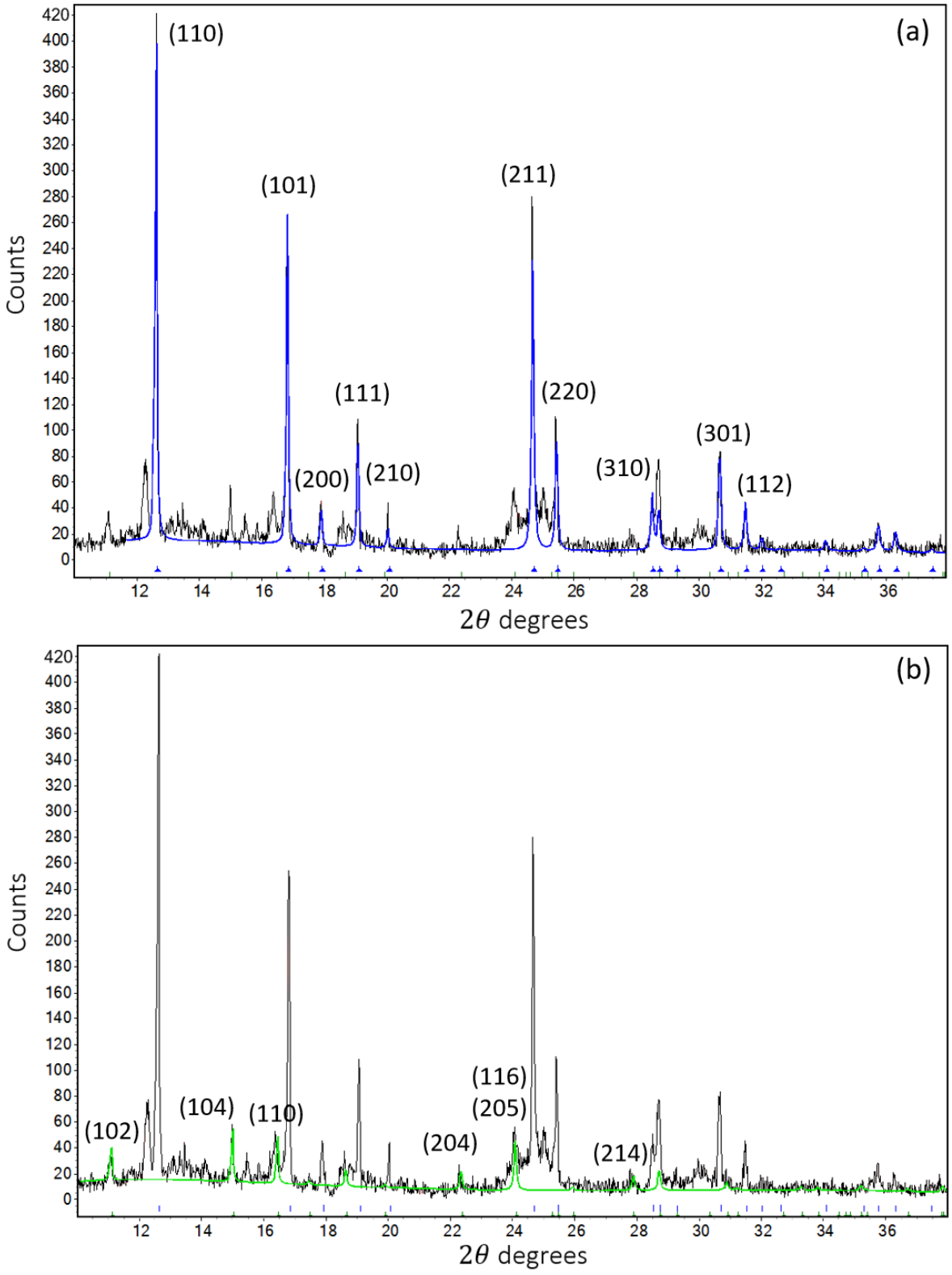


Figure 7.4: XRD spectra for the $VO_2$ sample obtained from Sigma Aldrich. The data measured at 450 K is displayed in black in both (a) and (b). The overlaid blue spectrum for $VO_2$(R) in (a) confirms that the sample undergoes the expected phase transition. The green spectrum in (b) corresponds to crystalline $V_2O_3$ impurity.

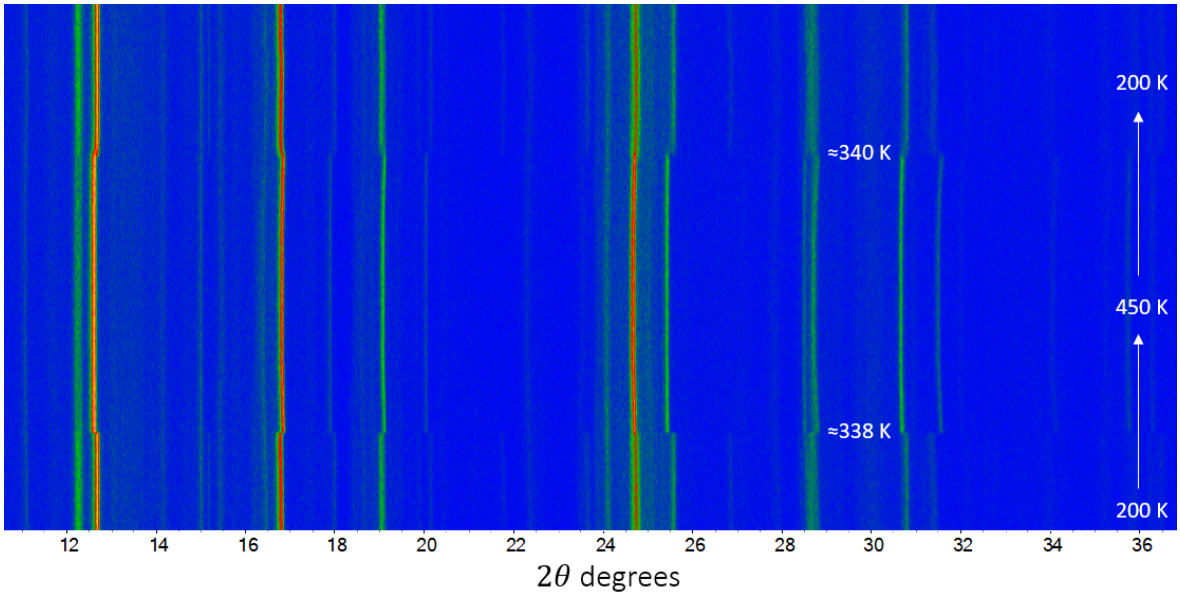


Figure 7.5: 'Top-down' view of the diffraction patterns for $VO_2$ sample across a heating and cooling cycle. The phase transition is indicated by sudden changes in the position of certain peaks.

## 7.3 Electron beam damage studies in $VO_2$

As in previous experiments with $WS_2$, electron Compton scattering experiments in $VO_2$ are limited by the electron flux, beyond which the material reaches an undesirable level of damage incurred by electron beam irradiation. Generally, transition metal oxides are susceptible to radiolysis, which results in reduction of metal ions [151]. For instance, $V_2O_5$ gradually transforms into VO [151,152], which is confirmed by changes in EELS and electron diffraction patterns as a function of electron irradiation time in Fig. 7.6. At low electron flux, reduction typically occurs at the sample surface and gradually extends into the bulk, while at high flux, structural changes occur in both surface and bulk of the material [151]. Also, reduction to the base metal together with amorphisation and sputtering of the metal oxide has been observed, although that typically requires STEM probes of very high current density [151]. Furthermore, exposure of vanadium oxides to the electron beam may also lead to an increase in sample crystallinity, which is explained by both an increase in temperature of the irradiated sample surface and its oxidation with beam-generated ozone. Such reactions have been studied in a $V_2O_5$ system irradiated by a 1 MeV electron beam [153].

Similar electron irradiation effects as observed in $V_2O_5$ are likely to occur in $VO_2$ samples studied in this work. Hence, in order to establish the maximum Compton measurement time whilst preserving the sample's high structural integrity, $VO_2$ flakes were first studied via HRTEM, as shown in Fig. 7.7. It consists of eight snapshots of the $VO_2$ domain taken

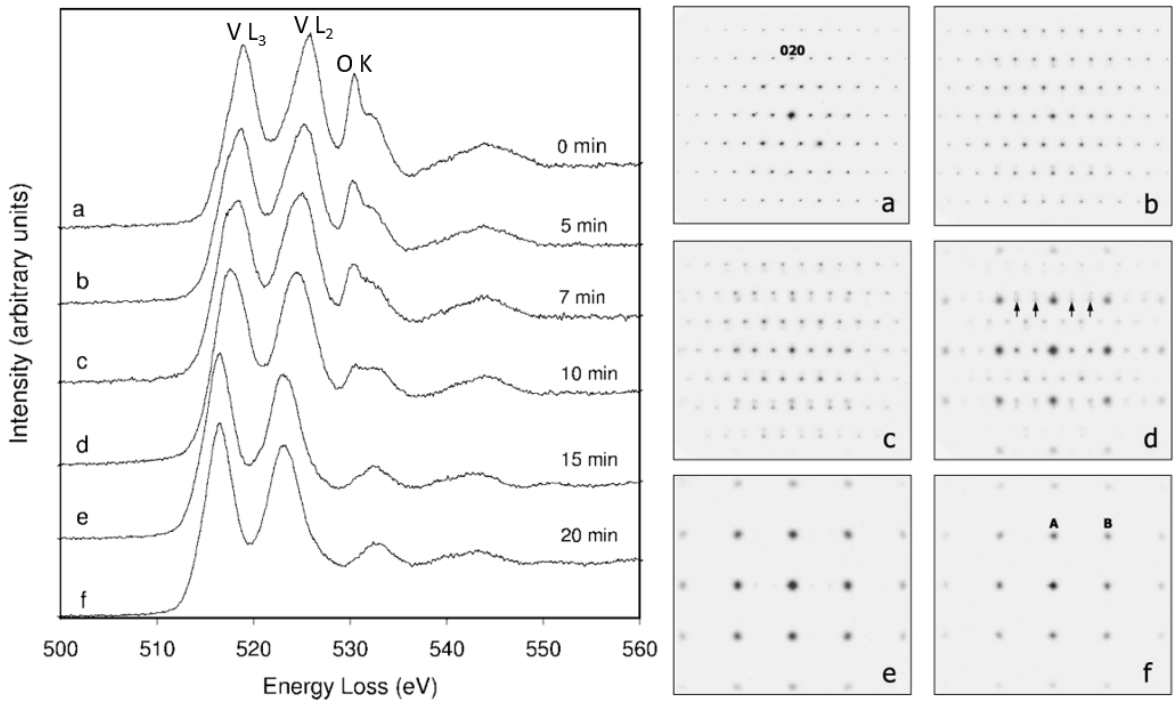


Figure 7.6: EELS spectra (left) capturing vanadium 2p and oxygen 1s energy loss near edge structure (ELNES) of a (001) oriented $V_2O_5$ sample over 20 minutes of 200 keV electron beam irradion time, (a)-(f). Decrease in the O K-edge intensity indicates loss of oxygen from the crystal lattice and the shift of the V $L_3$ peak to lower energy loss values implies a change in the vanadium oxidation state from $V^{5+}$ to $V^{2+}$. The electron diffraction patterns of the sample (right) corresponding to the same beam exposure times (a)-(f) show a structural change from $V_2O_5$ to VO. Image adapted from [152].

over 240 seconds of electron beam irradiation. The beam accelerating voltage was 200 kV and both the condenser aperture size and beam spot size were identical to those used for Compton measurements. Due to the highly polycrystalline nature of the flake, rigorous tracking of the early stages of defect formation via HRTEM turned out to be quite difficult, although higher image contrast fluctuations can be observed at later stages of the measurement. Nonetheless, fast Fourier transform (FFT) of the images shown in the corresponding insets in Fig. 7.7 show a slight increase in flake crystallinity with an increasing measurement time. Considering that the HRTEM images were acquired with a partially convergent electron beam, it is important to note that the extent of these effects would be lower in Compton scattering experiments, which use parallel and therefore a less intense beam.

The state of lattice crystallinity can also be observed via changes in diffracted beam intensity in the sample. Generally, it is quantified as a function of electron fluence; however, an accurate measurement of the fluence in the TEM used in this work was not possible. For this reason, the changes in intensity of diffraction patterns were studied as a function of the beam exposure time, as depicted in Fig. 7.8. It captures six electron diffraction patterns and

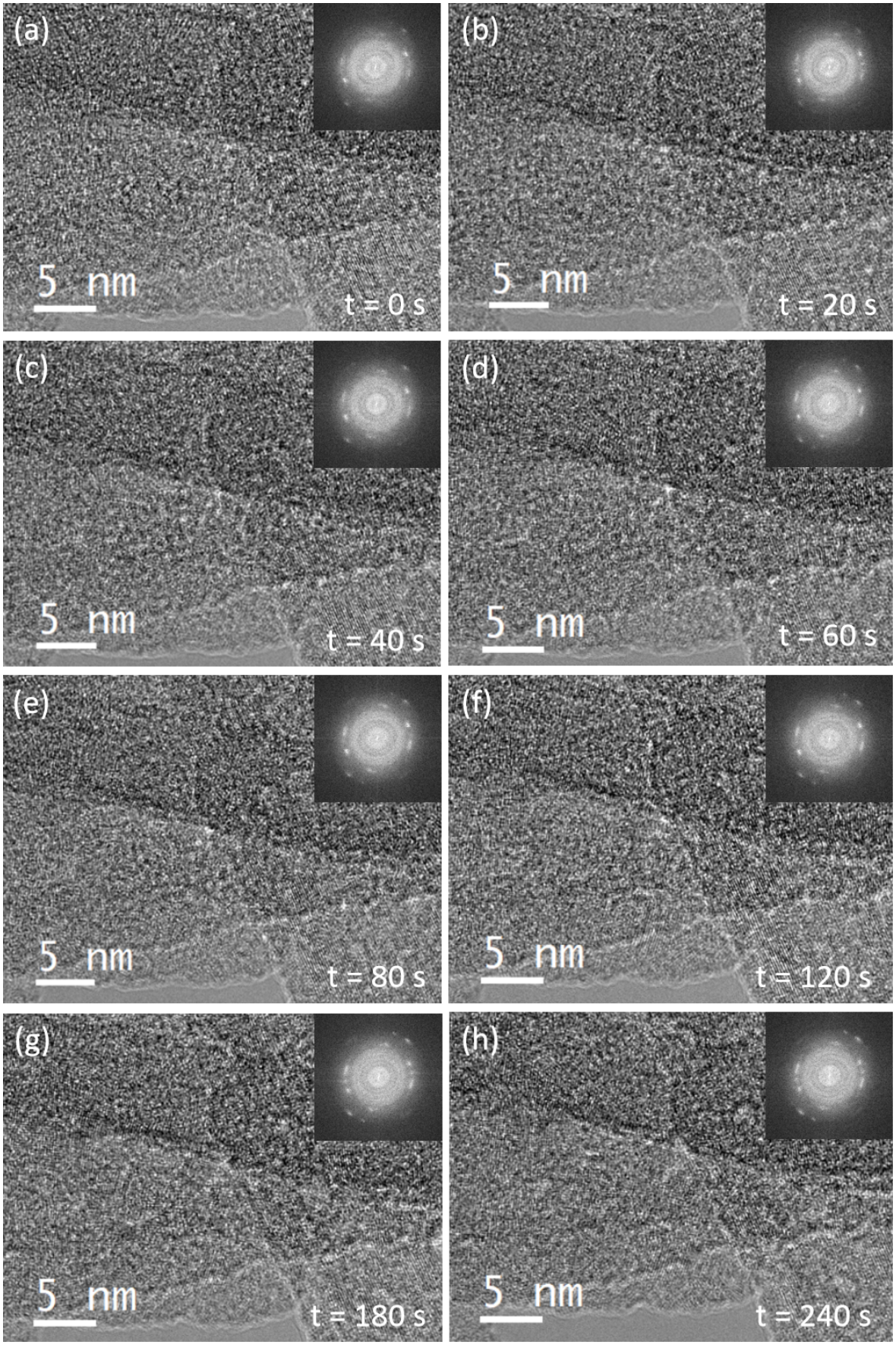


Figure 7.7: HRTEM images of a $VO_2$ flake taken over 240 s of electron beam irradiation.

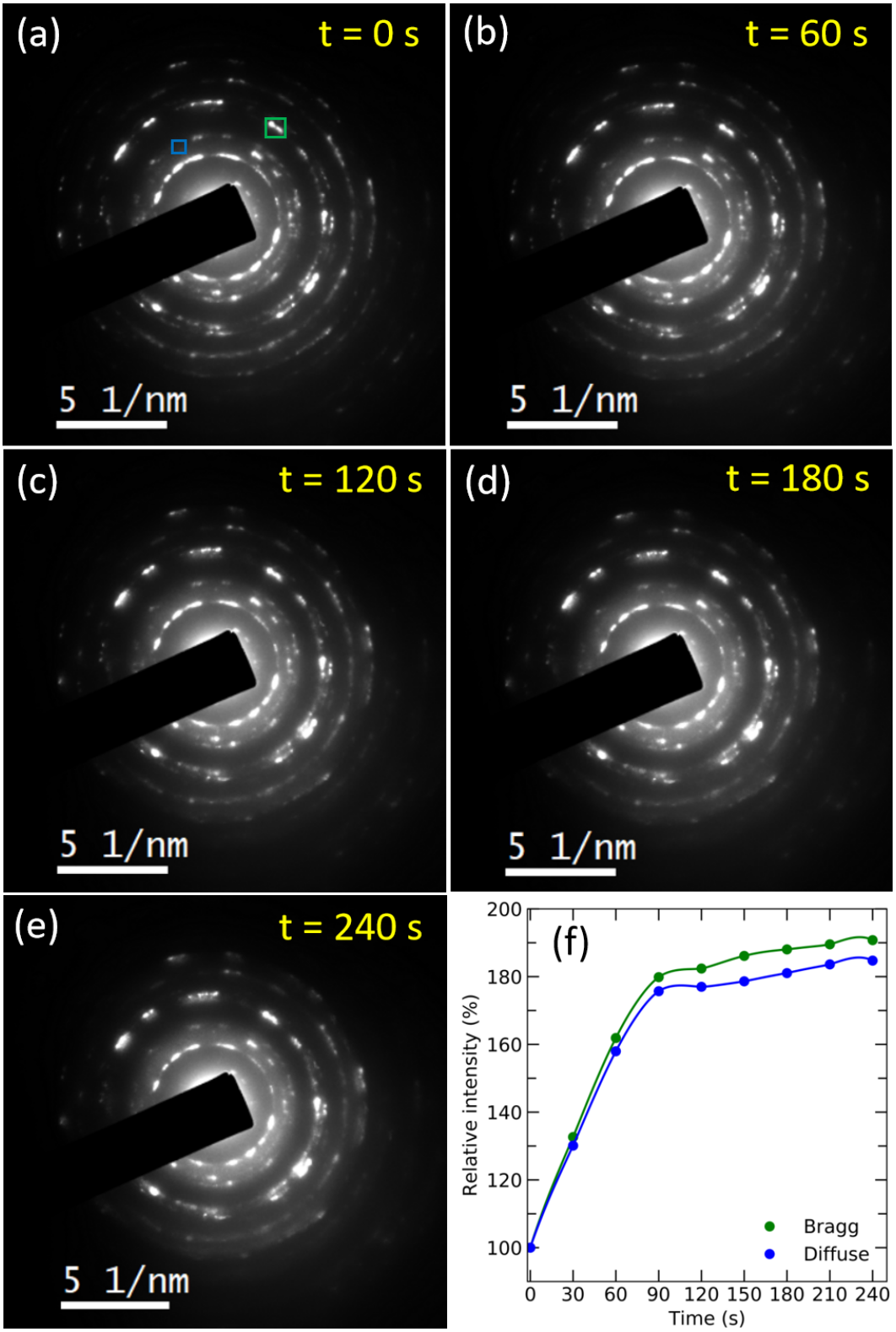


Figure 7.8: Electron diffraction patterns of a $VO_2$ flake taken over 240 s of electron beam irradiation. The exposure time for each electron diffraction pattern was kept the same. The diffraction spots representing [012] planes in $VO_2$(M1) (Table 7.1) and the diffuse scattering background used for damage analysis are marked by the green and blue squares in the pattern (a) respectively. The resulting intensity fluctuations of the selected areas are shown in (f), where the solid lines are a guide to the eye.

temporal intensity profiles of the diffracted beams and diffuse scattering background marked by green and blue squares in Fig. 7.8(a) respectively. Overall, the figure shows a gradual increase of the diffracted beam intensity with time, which could indicate improving sample crystallinity (for instance, an improvement in stoichiometric ratio due to oxidation). On the other hand, loss of sharpness of the diffraction spots can be observed throughout the duration of the measurement, as well as an increase in the intensity of the diffuse scattering. This could possibly be associated with tilting of oxygen octahedra, lattice deformations or a reduction in grain size.

Further, electron beam damage effects in the $VO_2$ sample were studied using EELS, in particular vanadium $L_3$, $L_2$ and oxygen K-edges. Due to the presence of the $V_2O_3$ phase, which constitutes roughly 15% of the sample, the features of the core loss edges will be somewhat distorted compared to the pure $VO_2$ phase. Nonetheless, due to the dependence of the vanadium L-edge position on its oxidation state, as well as direct proportionality between the intensity of the oxygen edge and the number of oxygen atoms within the irradiated sample area, EELS spectra can still provide information about potential oxygen sputtering and overall stability of the sample under the electron beam. Both reference spectra [154] and measured EELS spectra showing the relevant core loss edges of the samples studied in this work are displayed in Fig. 7.9. Over 4 minutes of beam exposure time, the measured vanadium $L_3$ and $L_2$ white lines (Fig. 7.9 (c)) show high stability in terms of their shape and relative intensity. Their positions fluctuate by up to 0.8 eV with respect to the initial positions at 517.0 eV and 523.4 eV respectively, while maintaining the inter-peak distance of 6.4 eV (for reference, the chemical shifts of the V-$L_3$ white line between $V^{+5}$, $V^{+4}$ and $V^{+3}$ oxidation states have been measured to be 1.5 eV and 0.5 eV [154]). The position fluctuation seems to be random and could be caused by the shift in the ZLP. As for the oxygen K-edge in Fig. 7.9 (c), no significant changes occur in its shape throughout the measurement time and its position moves very slightly in sync with the V-$L_3$ and V-$L_2$ white lines. Note that the suspected lattice deformations and tilting of oxygen octahedra (see previous paragraph) may still occur, but any resulting changes to the $L_3$, $L_2$ white line fine structure in the vanadium core loss edge may be too subtle to detect within the energy resolution ($\approx$2 eV) of the EELS measurement.

Considering the electron beam damage data obtained by HRTEM, electron diffraction and EELS of the core loss edges for the $VO_2$ flakes, it is difficult to determine the exact dynamical processes occurring in the sample under electron beam illumination. While both HRTEM imaging and core loss edge spectroscopy show a certain degree of sample stability with a potential increase in its crystallinity, diffraction patterns reveal an increase in diffuse scattering

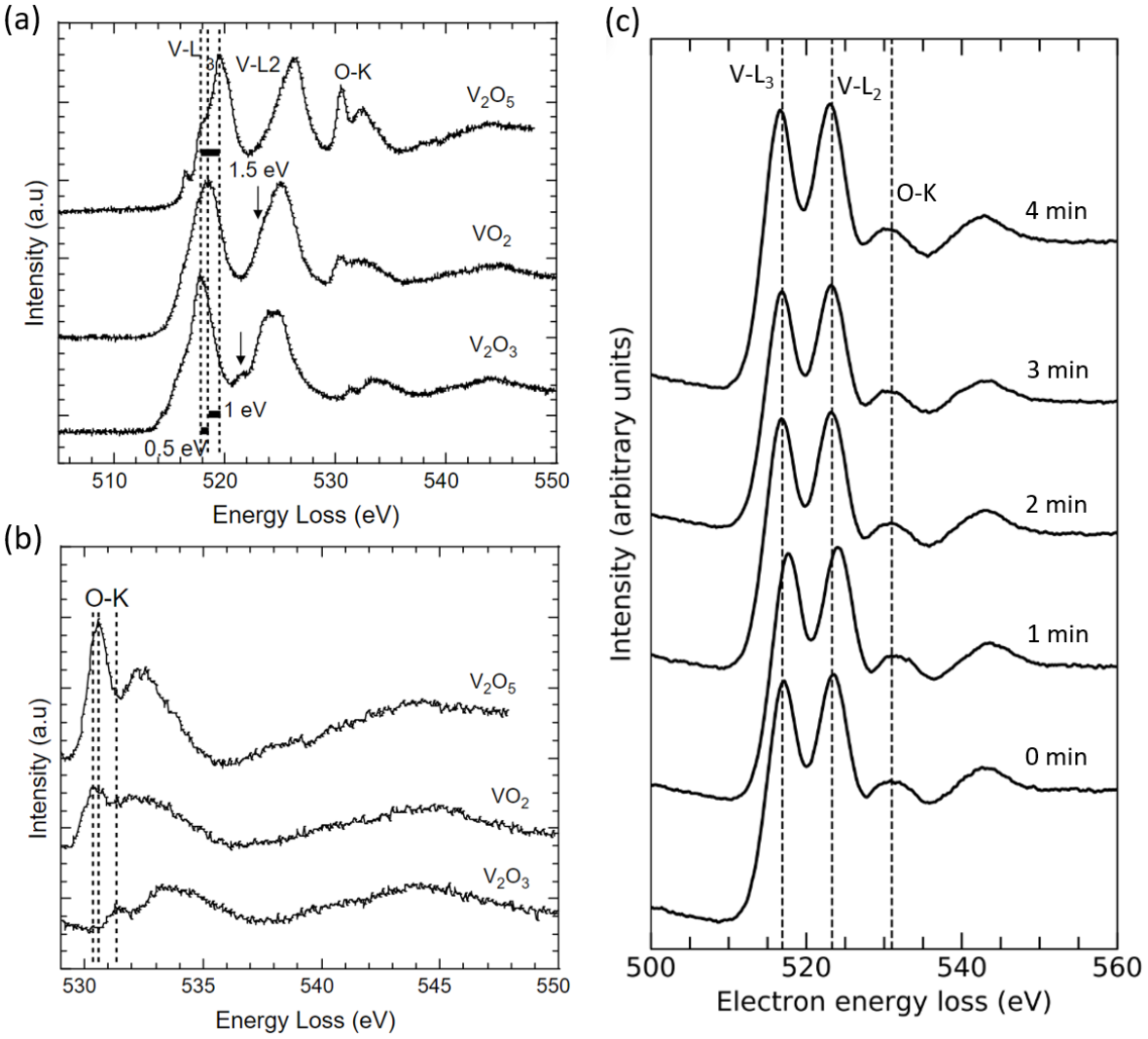


Figure 7.9: (a), (b) Reference EELS spectra showing vanadium L and oxygen K-edges in $V_2O_3$, $VO_2$ and $V_2O_5$ [154]. In these oxides, vanadium is in $V^{+3}$, $V^{+4}$ and $V^{+5}$ oxidation states respectively. (c) Measured EELS spectra of the $VO_2$ sample capturing vanadium L and oxygen K-edges. In (c), the spectra are scaled for clarity and the broken lines are placed at 517.0 eV, 523.4 eV and 531.0 eV.

throughout the measurement time. Hence, as a precaution, two sets of electron Compton scattering data representing 1 min and 2 min measurements were obtained and compared.

## 7.4 Electron Compton scattering in $VO_2$

Electron Compton scattering measurements in insulating $VO_2$(M1) and metallic $VO_2$(R) phases were carried out as per methodology outlined in Section 4.4 with the aim to capture changes in the electronic band structure resulting from the phase transition at ≈68 °C. Due to a certain degree of uncertainty in determining the optimal measurement time (Sec. 7.3), two data sets representing 1 min and 2 min long measurements were collected. An example

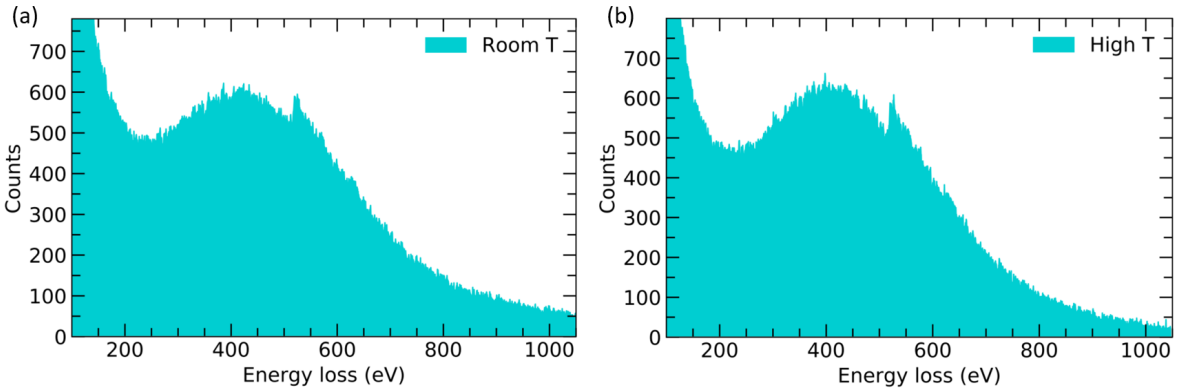


Figure 7.10: EELS spectra containing Compton peaks for insulating $VO_2$(M1) (a) and metallic $VO_2$(R) (b) phases. The spectra also contain vanadium $L_{3,2}$ edges with an onset at 513 eV.

of raw EELS spectra measured along an arbitrary electron scattering direction for $VO_2$(M1) and $VO_2$(R) phases are shown in Fig. 7.10. Besides the plasmon peak background on the low energy loss side of the Compton peak, the spectra also display vanadium L-edges at approximately 513 eV.

In order to compare electron Compton data with existing photon Compton measurements and corresponding theoretical predictions (Sec. 2.1.3), isotropic electron Compton profiles were obtained for both metallic and insulating phases of $VO_2$ by summing seven EELS spectra, such as those displayed in Fig. 7.10, from different flakes. Due to the inconvenient position of the vanadium L-edge, the low energy loss sides of the Compton peaks were analysed (note that by increasing the scattering angle, the Compton peak could be shifted to energy loss values beyond the vanadium L-edges; however, that would result in a significant decrease of the scattering cross-section). The resulting isotropic electron Compton profiles from which the plasmon background is subtracted via the power law fit are shown in Fig. 7.11. As in previous experiments with amorphous carbon films and $WS_2$ (Chapters 5 and 6), they were subsequently converted into projected electron momentum density profiles $J(p_z)$, i.e. the energy loss axis was converted into projected momentum scale $p_z$ using Eqn. 5.1.7 and the electron count axis was converted into $J(p_z)$ scale by integrating the Compton profile to the number of electrons participating in scattering. In the case of $VO_2$ under the given experimental conditions, half of the Compton profile represented 12.5 electrons. The resulting $J(p_z)$ profiles for the $VO_2$(M1) and $VO_2$(R) phases and their differences are displayed in Fig. 7.12. The difference profiles are normalised to the $J(p_z)$ value at $p_z$=0 for the high temperature (R) phase. As shown in Fig. 2.12 and Fig. 2.13, the expected changes in the isotropic projected electron momentum density profiles are of the order of 0.1%; however,

random noise in both sets of data is significantly higher and, in principle, would conceal any of the predicted changes. Furthermore, there are quite significant differences between the $J(p_z)$ profiles corresponding to 1 min and 2 min measurements of the component electron Compton profiles. Considering current random noise levels, the difference profiles should fluctuate around zero, yet systematic deviations occur across the entire $p_z$ range. This could potentially be an artefact of the plasmon background subtraction via the power law. While the method worked reasonably well in the experiments with amorphous carbon, its application in systems displaying very subtle changes in the projected electron momentum density might lack in accuracy. Under these circumstances, data analysis techniques would benefit from more rigorous plasmon background modelling and subtraction (Chapter 8). Also, in order to reduce the experimental error of the measurements and capture the relevant changes in the isotropic projected electron momentum density, the count number at the peak maximum should reach approximately $10^7$. This gives a Poisson fractional noise of $\frac{1}{\sqrt{10^7}}$, below the 0.1% error required to detect the expected changes in $J(p_z)$. From Fig. 7.11 it is clear that the counts in the current measurements are smaller than the required value by a factor of at least three orders of magnitude. While substantial increase of the measurement time of the component spectra could be detrimental to the $VO_2$ flakes due to the beam damage effects, increasing the number of measured flakes is also not quite realistic. In this case, the required count number could possibly be reached by making Compton measurements at lower scattering angles where the scattering cross-section is larger. This would in turn further stress the necessity of very accurate plasmon background subtraction.

## 7.5 Conclusions

In this chapter, a $VO_2$ powder purchased from *Sigma-Aldrich* was characterised via XRD measurements, confirming that it consists predominantly of a $VO_2$(M1) phase, which undergoes a structural monoclinic-to-tetragonal crystal lattice transition (and hence an insulator-to-metal transition) at ≈65 °C upon heating. An impurity phase $V_2O_3$ was also detected and confirmed to constitute approximately 15% of the sample. Further, $VO_2$ flakes were studied via HRTEM imaging, electron diffraction and EELS, establishing optimal experimental conditions for electron Compton scattering experiments and taking care to avoid undesirable levels of sample damage due to prolonged exposure to the electron beam. The subsequent Compton experiments, however, did not produce satisfactory results, i.e. isotropic $J(p_z)$ profiles measured for both low and high temperature $VO_2$ phases and different cumulative times

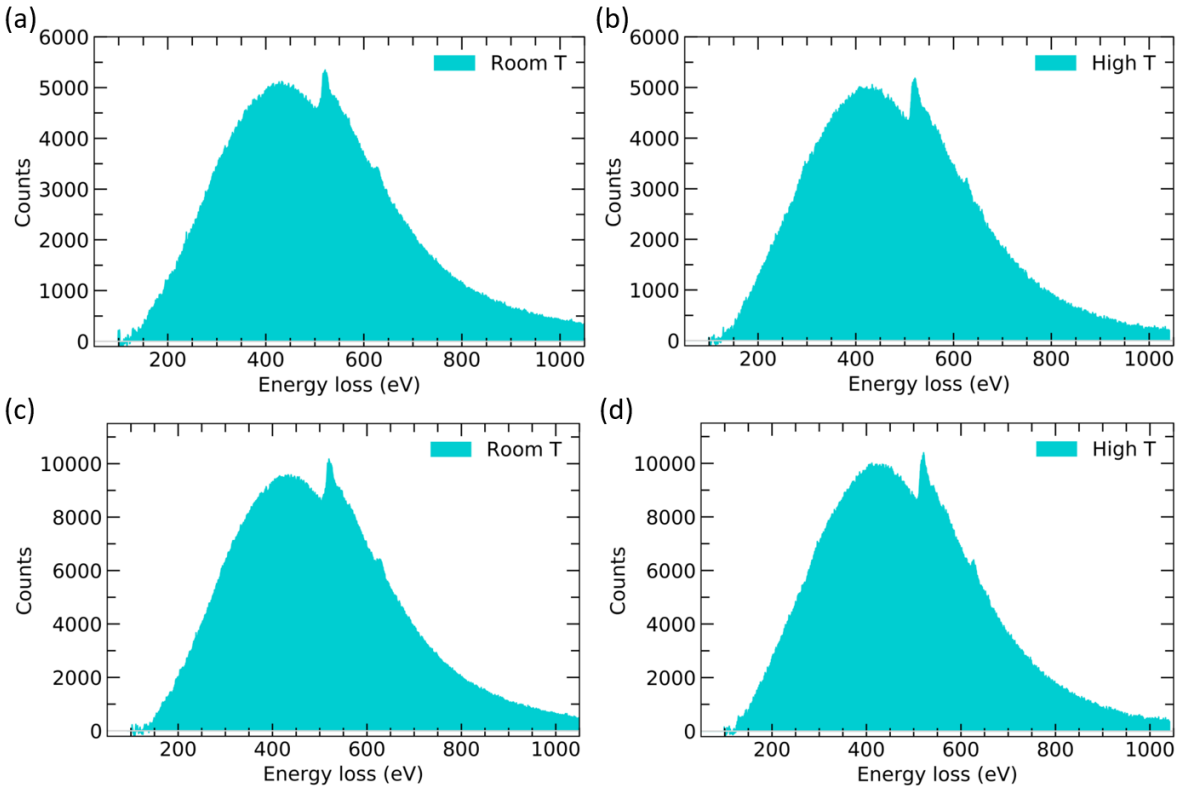


Figure 7.11: Sum of the component EELS spectra measured for 1 min, representing isotropic Compton peaks for insulating $VO_2$(M1) (a) and metallic $VO_2$(R) (b) phases. Analogous spectra representing 2 min component measurements are in (c) and (d) respectively. The small peak at approximately 628 eV is the vanadium L1 edge.

were subject to systematic errors associated with insufficiently accurate plasmon background subtraction. Furthermore, high noise levels with a potential to conceal any predicted differences in J($p_z$) profiles between the two phases were observed. Nonetheless, a few changes to the experimental methodology and data analysis techniques were suggested, which would likely improve the quality and accuracy of experimental results.

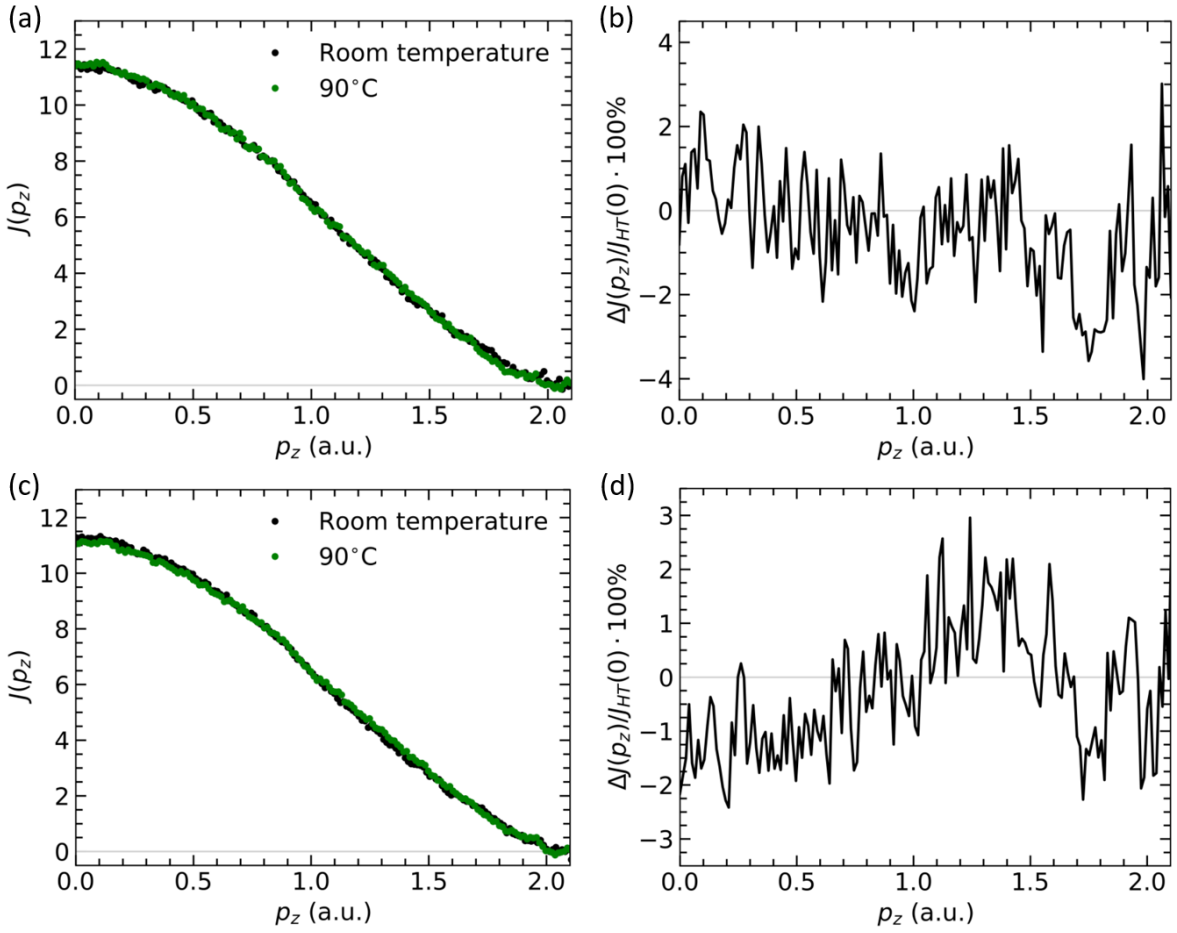


Figure 7.12: Isotropic projected electron momentum density profiles for metallic $VO_2$ (high temperature, 90 °C) and insulating $VO_2$ (room temperature) phases corresponding to 1 min (a) and 2 min (b) component measurements. The profiles were generated from EELS spectra binned at 2 eV resolution. Their (normalised) difference profile is shown in (b) and (d) respectively.

# Chapter 8

# Outlook

The electron Compton scattering experiments carried out in this work to study various condensed matter phenomena provide an interesting perspective for further developments of the technique. Hence, this chapter briefly outlines potential avenues for further improvements of the Compton experimental methodology, which could provide measurements at higher sensitivity, resulting in eventual expansion of the range of materials that could be studied by this technique.

## 8.1 Strategies to optimise electron Compton scattering measurements

Investigations of the projected electron momentum densities in amorphous carbons films, monolayers and bilayers of $WS_2$, and MIT in $VO_2$ flakes have shown a variable degree of success with a very prominent trade-back between Compton-scattered electron count number and radiation damage induced by the beam. However, an improvement in the counting statistics in electron Compton measurements (or EELS more broadly) can be achieved by employing novel direct electron detectors. The usual EELS detector design, shown schematically in Fig. 8.1(a), relies on scintillator-coupled CCD detectors, which typically use an yttrium aluminium garnet (YAG) single crystal to convert impinging electrons into photons [155]. These are subsequently transferred via fibre optics to a CCD sensor placed in the dispersion plane of the spectrometer. However, the electron-to-photon conversion together with the photon transfer to the CCD reduce its detector quantum efficiency and hence the signal-to-noise ratio (SNR) of the resulting Compton or EELS spectrum. The direct electron detectors, on

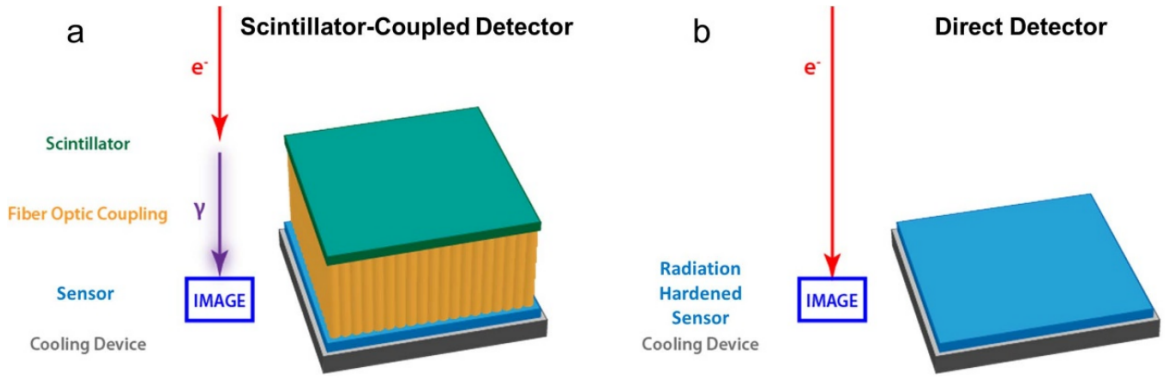


Figure 8.1: Comparison between indirect (a) and direct (b) electron detectors. Image adapted from [155].

the other hand, are designed to withstand the direct exposure of the sensor to the incident electrons and therefore preserve the level of efficiency that is otherwise lost in the scintilllator and fibre optic components of the indirect electron detectors (Fig. 8.1(b)). Furthermore, direct electron detectors offer a higher degree of signal localisation and shorter acquisition times, which is important in the studies of materials that are sensitive to the electron beam exposure [155, 156].

Further improvements in the Compton-scattered electron count rate can be achieved by conducting experiments at lower electron scattering angles, where the scattering cross-section is higher (provided that probe-matter interactions are still described well by the impulse approximation). This places the Compton profile on the 'tail' of an intense plasmon peak, which has to be subtracted in order to obtain the projected electron momentum density profile of the sample. As was seen in Compton experiments with amorphous carbon (Chapter 5, sometimes simple subtraction routines provide reasonable results, but they may fail when Compton scattering is used to track very subtle changes in the electronic structure, such as the MIT phase transformation in $VO_2$. Under these circumstances, DFT may be employed in order to model and subtract the plasmon background. This is typically carried out by simulating the macroscopic dielectric function of a given material $\epsilon$, which is related to the double differential inelastic scattering cross section, i.e.:

$$\frac{d^2\sigma}{d\Omega dE} = -\frac{1}{(q\pi e a_0)^2}\mathrm{Im}[\epsilon^{-1}(\mathbf{q},\omega)], \tag{8.1.1}$$

where $dE$ is the energy transfer of electrons scattered in the solid angle $d\Omega$, $a_0$ is the Bohr radius, $e$ is the electron charge, $m_0$ is the free-electron mass and $\mathbf{q}$ is the momentum transfer [157].

As for experiments with $WS_2$, several modifications of the experimental and computational

methodology could be made in order to obtain both better quality data and theoretical predictions. Firstly, the measurements carried out at 200 keV electron beam energy showed the material's susceptibility to sputter damage. This could be avoided using a lower energy electron beam, for instance at 80 keV as seen in the Compton experiments with few-layer graphene [35]. It would in turn facilitate longer Compton measurement time and therefore yield improved counting statistics. Further, in order to produce DFT theoretical predictions that are a better reflection of the experimental conditions, simulation of a $WS_2$ bilayer could include a rotational interlayer misalignment via construction of a supercell. However, satisfying periodic boundary conditions for such a supercell is challenging and inevitably results in a large number of atoms (>100) that increases the computation time considerably.

# Appendix A

## A.1 Python code for modelling Compton profile in STEM mode

```
import numpy as np
from matplotlib import pyplot as plt

######################################################################

# R=1.95    #radius of a STEM probe in units of q (nm-1) CL3
R=4.85    #radius of a STEM probe in units of q (nm-1) CL2
q_c=17.0    #variable scattering vector measured from the centres of STEM
        probes

l=2.53*10**-3  #electron wavelength at 197 kV in nm
T_1=197000 #primary electron energy in eV
m0c2=511000 #in eV
m0_SI=9.1*10**(-31) #electron rest mass in kg

######################################################################

## Division of the STEM probe into dots
t = np.linspace(0,2*np.pi,100);
x = R*np.sin(t);
```

```
y = R*np.cos(t);
#now create uniform mesh over square with some given cell size cs
cs = 0.3;
nm=int(2*R/cs)
xm = np.linspace(-R,R,nm);
ym = np.linspace(-R,R,nm);
[X,Y] = np.meshgrid(xm,ym);
#check for points inside the circle
inside = X**2+Y**2<R**2
plt.plot(x,y,'r',X[inside],Y[inside],'.b')
#the coordinates you are looking for are given in (X(inside),Y(inside))
plt.show()

# ## Finding scattering vectors of each point

q=np.empty(shape=(len(X[inside])))
for i in range(len(q)):
    q[i]=np.sqrt((q_c-X[inside][i])**2+(Y[inside][i])**2)

two_theta=q*l   #Find the electron scattering angle two_theta
            (small angle approximation applied) in rad

T_p=2*np.sin(two_theta/2.0)**2*(2*T_1+(T_1**2/m0c2)) #Assign the energy
transfer at the peaks of CPs defined by the angles above

print np.shape(T_p)
######################################################################

#Generation of component Compton profiles
data=np.loadtxt('pz_q149_full.txt')    #import a generic J(pz) curve
# data=np.loadtxt('pz_q123_full_final.txt')    #import a generic J(pz) curve:
pz=data[:,0]
intensity=data[:,1]
plt.plot(pz,intensity)
```

```
plt.show()

#create empty arrays of the length of [T_p x (length of pz)] for be filled in
by for-loops --- for SI units and eV
delta_T_SI=np.empty(shape=(len(T_p),len(pz)))
eloss=np.empty(shape=(len(T_p),len(pz)))

#create separate x-axes for every T_p based on the generic curve
for i in range(len(T_p)):   #creates a list of integers up to of value of the
length of T_p
    delta_T_SI[i]=-pz*1.99*10**(-24)*np.sqrt(2*T_p[i]*1.6*10**(-19)/m0_SI)
    #redefines pz according to different T_p values
    eloss[i]=T_p[i]+delta_T_SI[i]/(1.6*10**(-19))



#create an empty array where replicas of a generic y-axis will go
intensity2=np.empty(shape=(len(T_p),len(intensity)))

#create y-axes for every x-axis above.
for i in range(len(T_p)):
    intensity2[i]=intensity

#calculate areas of the set of the peaks
area=np.empty(shape=(len(T_p)))
for i in range(len(T_p)):
    area[i]=np.trapz(intensity2[i],-eloss[i,:])

# #turn the areas above into unit areas
# intensity_unit=np.empty(shape=(len(T_p),len(intensity2[1,:])))
# for i in range(len(T_p)):
#     intensity_unit[i]=intensity2[i,:]/area[i]

#turn the areas above into unit areas+adjusted by scattering x-section.
intensity_unit=np.empty(shape=(len(T_p),len(intensity2[1,:])))
```

```
for i in range(len(T_p)):
    intensity_unit[i]=1/((q[i])**4)*intensity2[i,:]/area[i]
#     intensity_unit[i]=intensity2[i,:]/area[i]

#check if the intensities above indeed give unit+adjusted areas
area_unit=np.empty(shape=(len(T_p)))
for i in range(len(T_p)):
    area_unit[i]=np.trapz(intensity_unit[i],-eloss[i,:])
print area_unit



for i in range(len(T_p)):
    #plt.plot(eloss[i,:],intensity_corr[i,:]/np.max(intensity_corr),'r,')
     plt.plot(eloss[i,:],intensity_unit[i,:],'r,')
plt.show()
######################################################################

#sum the component CPs via interpolation
from scipy import interpolate

tck=np.zeros(shape=(len(T_p)),dtype=tuple)
for i in range(len(T_p)):
    tck[i] = interpolate.splrep(np.flip(eloss[i,:],0), np.flip(intensity_unit
    [i,:],0), s=0)

xnew=np.linspace(-300,1400,num=1400)

ynew = np.zeros(shape=(len(T_p),len(xnew)))
for i in range(len(T_p)):
    ynew[i]= interpolate.splev(xnew, tck[i], der=0)

for i in range(len(T_p)):
    plt.plot(xnew,ynew[i])
```

```
yfinal= np.zeros(shape=(len(xnew)))
for i in range(len(T_p)):
    yfinal=yfinal+ynew[i,:]

for i in range(len(T_p)):
    plt.plot(eloss[i,:],intensity_unit[i,:]/np.max(intensity_unit),'r,')



plt.plot(xnew,yfinal/np.max(yfinal),'b.')
plt.show()

#data export
beam_sum=np.array([xnew,yfinal/np.max(yfinal)])
np.savetxt('HLbeamCP_CL2_new.txt',np.column_stack(beam_sum),fmt='%f')
```

# Bibliography


[1] X Liu and MC Hersam. 2D materials for quantum information science. *Nature Reviews Materials*, 4(10):669–684, 2019.

[2] S Kumar, R Rani, N Dilbaghi, K Tankeshwar, and KH Kim. Carbon nanotubes: a novel material for multifaceted applications in human healthcare. *Chemical Society Reviews*, 46(1):158–196, 2017.

[3] L Zhou, J Mao, Y Ren, ST Han, VA Roy, and Y Zhou. Recent advances of flexible data storage devices based on organic nanoscaled materials. *Small*, 14(10):1703126, 2018.

[4] D Andre, SJ Kim, P Lamp, SF Lux, F Maglia, O Paschos, and B Stiaszny. Future generations of cathode materials: an automotive industry perspective. *Journal of Materials Chemistry A*, 3(13):6709–6732, 2015.

[5] J Azadmanjiri, J Wang, CC Berndt, and A Yu. 2D layered organic–inorganic heterostructures for clean energy applications. *Journal of Materials Chemistry A*, 6(9):3824–3849, 2018.

[6] RM Martin. *Electronic Structure: Basic Theory and Practical Methods*. Cambridge University Press, 2004.

[7] P Hohenberg and W Kohn. Inhomogeneous electron gas. *Physical review*, 136(3B):B864, 1964.

[8] W Kohn and LJ Sham. Self-consistent equations including exchange and correlation effects. *Physical review*, 140(4A):A1133, 1965.

[9] P Schwerdtfeger. The pseudopotential approximation in electronic structure theory. *ChemPhysChem*, 12(17):3143–3155, 2011.

[10] MC Payne, MP Teter, DC Allan, TA Arias, and JD Joannopoulos. Iterative minimization techniques for ab initio total-energy calculations: molecular dynamics and conjugate gradients. *Reviews of modern physics*, 64(4):1045, 1992.

[11] M Cooper, P Mijnarends, N Shiotani, N Sakai, and A Bansil. *X-ray Compton scattering*, volume 5. OUP Oxford, 2004.

[12] MJ Cooper. Compton scattering and electron momentum determination. *Reports on Progress in Physics*, 48(4):415, 1985.

[13] B Williams. Compton scattering: the investigation of electron momentum distributions. 1977.

[14] AH Compton. A quantum theory of the scattering of X-rays by light elements. *Physical review*, 21(5):483, 1923.

[15] AH Compton. The spectrum of scattered X-rays. *Physical Review*, 22(5):409, 1923.

[16] JWM DuMond. Compton modified line structure and its relation to the electron theory of solid bodies. *Physical Review*, 33(5):643, 1929.

[17] G Grosso and GP Parravicini. *Solid state physics*. Academic press, 2013.

[18] JT Okada, PH-L Sit, Y Watanabe, YJ Wang, B Barbiellini, T Ishikawa, M Itou, Y Sakurai, A Bansil, R Ishikawa, et al. Persistence of covalent bonding in liquid silicon probed by inelastic x-ray scattering. *Physical Review Letters*, 108(6):067402, 2012.

[19] JA Duffy. What we can learn from magnetic Compton scattering: application to the determination of spin polarization. In *Journal of Physics: Conference Series*, volume 443, page 012011. IOP Publishing, 2013.

[20] P Carra, M Fabrizio, G Santoro, and BT Thole. Magnetic x-ray Compton scattering. *Physical Review B*, 53(10):R5994, 1996.

[21] MJ Cooper, E Zukowski, SP Collins, DN Timms, F Itoh, and H Sakurai. Does magnetic compton scattering only measure spin magnetization? *Journal of Physics: Condensed Matter*, 4(29):L399, 1992.

[22] P Schattschneider, P Pongratz, and H Hohenegger. Compton scattering in electron energy loss spectrometry. *Scanning Microscopy*, 1990(4):4, 1990.

[23] AL Hughes and Marvin M Mann Jr. A new method for investigating atomic electron velocities. *Physical Review*, 53(1):50, 1938.

[24] AL Hughes and Merle A Starr. Atomic electron velocities in nitrogen and methane. *Physical Review*, 55(4):343, 1939.

[25] TC Wong, JS Lee, HF Wellenstein, and RA Bonham. Experimental definition of valence-shell and cumulative-shell compton profiles from 25-keV electron-impact studies on $N_2$, Ne, and Ar. *Physical Review A*, 12(5):1846, 1975.

[26] RC Ulsh, HF Wellenstein, and RA Bonham. Bethe surface, elastic and inelastic differential cross sections, Compton profile, and binding effects for $H_2$ obtained by electron scattering with 25 keV incident electrons. *The Journal of Chemical Physics*, 60(1):103–111, 1974.

[27] BG Williams, GM Parkinson, CJ Eckhardt, JM Thomas, and T Sparrow. A new approach to the measurement of the momentum densities in solids using an electron microscope. *Chemical Physics Letters*, 78(3):434–438, 1981.

[28] Z Feng, S Löffler, F Eder, D Su, JC Meyer, and P Schattschneider. Combined study of the ground and unoccupied electronic states of graphite by electron energy-loss spectroscopy. *Journal of Applied Physics*, 114(18):183716, 2013.

[29] P Schattschneider, P Jonas, and M Mändl. Electron Compton scattering on solids-a feasibility experiment on a PEELS system. *Microscopy Microanalysis Microstructures*, 2(2-3):367–375, 1991.

[30] P Schattschneider and A Exner. Progress in electron compton scattering. *Ultramicroscopy*, 59(1-4):241–253, 1995.

[31] RF Egerton. *Electron Energy-Loss Spectroscopy in the Electron Microscope*. Plenum Press, 1996.

[32] BG Williams, TG Sparrow, and RF Egerton. Electron Compton scattering from solids. *Proceedings of the Royal Society of London. A. Mathematical and Physical Sciences*, 393(1805):409–422, 1984.

[33] Z Feng, B Yang, Y Lin, and D Su. Communication: Investigation of the electron momentum density distribution of nanodiamonds by electron energy-loss spectroscopy. *The Journal of Chemical Physics*, 143(21):211102, 2015.

[34] Z Feng, Y Sakurai, J Liu, D Su, and P Schattschneider. Anisotropy of electron Compton profiles of graphite investigated by electron energy-loss spectroscopy. *Applied Physics Letters*, 108(9):093108, 2016.

[35] Z Feng, X Zhang, Y Sakurai, Z Wang, H Li, and H Hu. Compton profile of few-layer graphene investigated by electron energy-loss spectroscopy. *Scientific Reports*, 9(1):1–5, 2019.

[36] A Damascelli. Probing the electronic structure of complex systems by ARPES. *Physica Scripta*, 2004(T109):61, 2004.

[37] H Iwasawa. High-resolution angle-resolved photoemission spectroscopy and microscopy. *Electronic Structure*, 2(4):043001, 2020.

[38] M Cattelan and NA Fox. A perspective on the application of spatially resolved ARPES for 2D materials. *Nanomaterials*, 8(5):284, 2018.

[39] VN Strocov, R Claessen, G Nicolay, S Hüfner, A Kimura, A Harasawa, S Shin, A Kakizaki, PO Nilsson, HI Starnberg, and P Blaha. Absolute band mapping by combined angle-dependent very-low-energy electron diffraction and photoemission: Application to Cu. *Physical Review Letters*, 81(22):4943, 1998.

[40] C Ernandes, L Khalil, H Henck, MQ Zhao, J Chaste, F Oehler, ATC Johnson, MC Asensio, D Pierucci, M Pala, J Avila, and A Ouerghi. Strain and spin-orbit coupling engineering in twisted $WS_2$/graphene heterobilayer. *Nanomaterials*, 11(11):2921, 2021.

[41] RW Siegel. Positron annihilation spectroscopy. *Annual Review of Materials Research*, 10:393–425, 1980.

[42] N Ida and N Meyendorf. *Handbook of advanced nondestructive evaluation*. Springer International Publishing Cham, Switzerland, 2019.

[43] R Suzuki, M Osawa, S Tanigawa, M Matsumoto, and N Shiotani. Positron study of electron momentum density and Fermi surface in titanium and zirconium. *Journal of the Physical Society of Japan*, 58(9):3251–3263, 1989.

[44] TD Haynes, RJ Watts, J Laverock, Z Major, MA Alam, JW Taylor, JA Duffy, and SB Dugdale. Positron annihilation study of the Fermi surface of $Ni_2MnGa$. *New Journal of Physics*, 14(3):035020, 2012.

[45] H Ceeh, JA Weber, M Leitner, P Böni, and C Hugenschmidt. The source-sample stage of the new two-dimensional angular correlation of annihilation radiation spectrometer at Technische Universität München. *Review of Scientific Instruments*, 84(4):043905, 2013.

[46] J Ketels, D Billington, SB Dugdale, M Leitner, and CP Hugenschmidt. Momentum density spectroscopy of Pd: Comparison of 2D-ACAR and Compton scattering using a 1D-to-2D reconstruction method. *Physical Review B*, 104(7):075160, 2021.

[47] F Tuomisto and I Makkonen. Defect identification in semiconductors with positron annihilation: experiment and theory. *Reviews of Modern Physics*, 85(4):1583, 2013.

[48] FJ Morin. Oxides which show a metal-to-insulator transition at the Neel temperature. *Phys. Rev. Lett.*, 3:34–36, 1959.

[49] V Eyert. The metal-insulator transitions of $VO_2$: A band theoretical approach. *Annalen der Physik*, 11(9):650–704, 2002.

[50] Z Shao, X Cao, H Luo, and P Jin. Recent progress in the phase-transition mechanism and modulation of vanadium dioxide materials. *NPG Asia Materials*, 10(7):581–605, 2018.

[51] C Ko and S Ramanathan. Observation of electric field-assisted phase transition in thin film vanadium oxide in a metal-oxide-semiconductor device geometry. *Applied Physics Letters*, 93(25):252101, 2008.

[52] Y Zhang, W Xiong, W Chen, and Y Zheng. Recent progress on vanadium dioxide nanostructures and devices: Fabrication, properties, applications and perspectives. *Nanomaterials*, 11(2), 2021.

[53] D Wegkamp and J Stähler. Ultrafast dynamics during the photoinduced phase transition in $VO_2$. *Progress in Surface Science*, 90(4):464–502, 2015.

[54] S Lee, IN Ivanov, JK Keum, and HN Lee. Epitaxial stabilization and phase instability of $VO_2$ polymorphs. *Scientific reports*, 6(1):1–7, 2016.

[55] A Srivastava, H Rotella, S Saha, B Pal, G Kalon, S Mathew, M Motapothula, M Dykas, P Yang, E Okunishi, DD Sarma, and T Venkatesan. Selective growth of single phase $VO_2$(A, B, and M) polymorph thin films. *APL Materials*, 3(2):026101, 2015.

[56] MF Jager, C Ott, PM Kraus, CJ Kaplan, W Pouse, RE Marvel, RF Haglund, DM Neumark, and SR Leone. Tracking the insulator-to-metal phase transition in $VO_2$ with few-femtosecond extreme UV transient absorption spectroscopy. *Proceedings of the National Academy of Sciences*, 114(36):9558–9563, 2017.

[57] JB Goodenough. The two components of the crystallographic transition in $VO_2$. *Journal of Solid State Chemistry*, 3(4):490–500, 1971.

[58] M Imada, A Fujimori, and Y Tokura. Metal-insulator transitions. *Rev. Mod. Phys.*, 70:1039–1263, Oct 1998.

[59] V Eyert. $VO_2$: A novel view from band theory. *Phys. Rev. Lett.*, 107:016401, 2011.

[60] Y Tokura and N Nagaosa. Orbital physics in transition-metal oxides. *Science*, 288(5465):462–468, 2000.

[61] JM Atkin, S Berweger, EK Chavez, MB Raschke, J Cao, W Fan, and J Wu. Strain and temperature dependence of the insulating phases of $VO_2$ near the metal-insulator transition. *Phys. Rev. B*, 85:020101, Jan 2012.

[62] A Zylbersztejn and NF Mott. Metal-insulator transition in vanadium dioxide. *Phys. Rev. B*, 11:4383–4395, 1975.

[63] Y Wang, KM Kang, M Kim, HS Lee, R Waser, D Wouters, R Dittmann, JJ Yang, and HH Park. Mott-transition-based RRAM. *Materials Today*, 28:63–80, 2019.

[64] Y Ke, S Wang, G Liu, M Li, TJ White, and Y Long. Vanadium dioxide: The multistimuli responsive material and its applications. *Small*, 14(39):1802025, 2018.

[65] X Cao, T Chang, Z Shao, F Xu, H Luo, and P Jin. Challenges and opportunities toward real application of $VO_2$-based smart glazing. *Matter*, 2(4):862–881, 2020.

[66] JM Wu and LB Liou. Room temperature photo-induced phase transitions of $VO_2$ nanodevices. *Journal of Materials Chemistry*, 21(14):5499–5504, 2011.

[67] JM Wu and WE Chang. Ultrahigh responsivity and external quantum efficiency of an ultraviolet-light photodetector based on a single $VO_2$ microwire. *ACS Applied Materials & Interfaces*, 6(16):14286–14292, 2014.

[68] H Lu, S Clark, Y Guo, and J Robertson. The metal–insulator phase change in vanadium dioxide and its applications. *Journal of Applied Physics*, 129(24):240902, 2021.

[69] AA Sabouri-Dodaran, C Bellin, G Loupias, M Marangolo, S Rabii, F Rachdi, T Buslaps, and M Mezouar. In situ pressure study of $Rb_4C_{60}$ insulator to metal transition by Compton scattering. *Phys. Rev. B*, 72:085412, 2005.

[70] Y Kobayashi, Y Sakurai, N Tsuji, K Sato, and K Asai. Symmetry change of Co $3d$ orbital associated with the 500-K spin crossover accompanied by insulator-to-metal transition in $LaCoO_3$. *Phys. Rev. B*, 98:115154, 2018.

[71] B Barbiellini, A Koizumi, PE Mijnarends, W Al-Sawai, H Lin, T Nagao, K Hirota, M Itou, Y Sakurai, and A Bansil. Role of oxygen electrons in the metal-insulator transition in the magnetoresistive oxide $La_{2-2x}Sr_{1+2x}Mn_2O_7$ probed by Compton scattering. *Phys. Rev. Lett.*, 102:206402, 2009.

[72] N Hiraoka, T Buslaps, V Honkimäki, H Minami, and H Uwe. Fermi surface nesting in $Ba_{1-x}K_xBiO_3$ observed by Compton profile measurement. *Phys. Rev. B*, 71:205106, 2005.

[73] M Gupta and DE Ellis. Cluster model for lattice distortion effects on electronic structure: VO and $VO_2$. *Phys. Rev. B*, 13:3405–3418, 1976.

[74] CN Chang, CC Chen, and HF Liu. The Compton profiles of vanadium oxides. *Journal of Physics: Condensed Matter*, 4(50):10445–10452, 1992.

[75] M Vashistha, DR Phalaswal, K Kabra, R Kumar, BK Sharma, and G Sharma. Electronic structure of $VO_2$ using Compton spectroscopy. *Materials Focus*, 5(6):517–523, 2016.

[76] KO Ruotsalainen, J Inkinen, T Pylkkänen, T Buslaps, M Hakala, K Hämäläinen, and S Huotari. The isotropic Compton profile difference across the phase transition of $VO_2$. *The European Physical Journal B*, 91(10):1–6, 2018.

[77] I Kylänpää, Y Luo, O Heinonen, PRC Kent, and JT Krogel. Compton profile of $VO_2$ across the metal-insulator transition: Evidence of a non-Fermi liquid metal. *Phys. Rev. B*, 99:075154, 2019.

[78] ND Mermin. Crystalline order in two dimensions. *Physical Review*, 176(1):250, 1968.

[79] KS Novoselov, AK Geim, SV Morozov, D Jiang, Y Zhang, Sergey V Dubonos, IV Grigorieva, and AA Firsov. Electric field effect in atomically thin carbon films. *Science*, 306(5696):666–669, 2004.

[80] AK Geim and KS Novoselov. The rise of graphene. *Nature Materials*, 6:183–191, 2007.

[81] A Khandelwal, K Mani, MH Karigerasi, and I Lahiri. Phosphorene–the two-dimensional black phosphorous: Properties, synthesis and applications. *Materials Science and Engineering: B*, 221:17–34, 2017.

[82] ME Dávila, L Xian, S Cahangirov, A Rubio, and G Le Lay. Germanene: a novel two-dimensional germanium allotrope akin to graphene and silicene. *New Journal of Physics*, 16(9):095002, 2014.

[83] B Anasori, MR Lukatskaya, and Y Gogotsi. 2D metal carbides and nitrides (MXenes) for energy storage. *Nature Reviews Materials*, 2(2):16098, 2017.

[84] JV Barth, G Costantini, and K Kern. Engineering atomic and molecular nanostructures at surfaces. *Nature*, 437:29, 2005.

[85] N Zhang, T Wang, X Wu, C Jiang, T Zhang, B Jin, H Ji, W Bai, and R Bai. From 1D polymers to 2D polymers: Preparation of free-standing single-monomer-thick two-dimensional conjugated polymers in water. *ACS Nano*, 11(7):7223–7229, 2017.

[86] M Chhowalla, HS Shin, G Eda, LJ Li, KP Loh, and H Zhang. The chemistry of two-dimensional layered transition metal dichalcogenide nanosheets. *Nature Chemistry*, 5(4):263, 2013.

[87] D Pasquier and OV Yazyev. Crystal field, ligand field, and interorbital effects in two-dimensional transition metal dichalcogenides across the periodic table. *2D Materials*, 6(2):025015, feb 2019.

[88] WJ Schutte, JL De Boer, and F Jellinek. Crystal structures of tungsten disulfide and diselenide. *Journal of Solid State Chemistry*, 70(2):207–209, 1987.

[89] Q Wang, P Wu, G Cao, and M Huang. First-principles study of the structural and electronic properties of $MoS_2$–$WS_2$ and $MoS_2$–$MoTe_2$ monolayer heterostructures. *Journal of Physics D: Applied Physics*, 46(50):505308, 2013.

[90] H Zeng, GB Liu, J Dai, Y Yan, B Zhu, R He, L Xie, S Xu, X Chen, W Yao, and X Cui. Optical signature of symmetry variations and spin-valley coupling in atomically thin tungsten dichalcogenides. *Scientific reports*, 3(1):1–5, 2013.

[91] QH Wang, K Kalantar-Zadeh, A Kis, JN Coleman, and MS Strano. Electronics and optoelectronics of two-dimensional transition metal dichalcogenides. *Nature Nanotechnology*, 7(11):699, 2012.

[92] W Choi, N Choudhary, GH Han, J Park, D Akinwande, and YH Lee. Recent development of two-dimensional transition metal dichalcogenides and their applications. *Materials Today*, 20(3):116–130, 2017.

[93] KF Mak and J Shan. Photonics and optoelectronics of 2D semiconductor transition metal dichalcogenides. *Nature Photonics*, 10(4):216–226, 2016.

[94] Q Zhao, Z Xie, YP Peng, K Wang, H Wang, X Li, H Wang, J Chen, H Zhang, and X Yan. Current status and prospects of memristors based on novel 2D materials. *Mater. Horiz.*, 7:1495–1518, 2020.

[95] X Yan, Q Zhao, AP Chen, J Zhao, Z Zhou, J Wang, H Wang, L Zhang, X Li, Z Xiao, K Wang, C Qin, G Wang, Y Pei, H Li, D Ren, J Chen, and Q Liu. Vacancy-induced synaptic behavior in 2D $WS_2$ nanosheet–based memristor for low-power neuromorphic computing. *Small*, 15(24):1901423, 2019.

[96] C Palacios-Berraquero, DM Kara, ARP Montblanch, M Barbone, P Latawiec, D Yoon, AK Ott, M Loncar, AC Ferrari, and M Atatüre. Large-scale quantum-emitter arrays in atomically thin semiconductors. *Nature communications*, 8(1):1–6, 2017.

[97] I Aharonovich, D Englund, and M Toth. Solid-state single-photon emitters. *Nature Photonics*, 10(10):631–641, 2016.

[98] C Androulidakis, K Zhang, M Robertson, and S Tawfick. Tailoring the mechanical properties of 2D materials and heterostructures. *2D Materials*, 5(3):032005, jun 2018.

[99] Y Liu, S Zhang, J He, ZM Wang, and Z Liu. Recent progress in the fabrication, properties, and devices of heterostructures based on 2D materials. *Nano-Micro Letters*, 11(1):1–24, 2019.

[100] YF Xiong, JH Chen, YQ Lu, and F Xu. Broadband optical-fiber-compatible photodetector based on a graphene-$MoS_2$-$WS_2$ heterostructure with a synergetic photogenerating mechanism. *Advanced Electronic Materials*, 5(1):1800562, 2019.

[101] G Arora, Y Sharma, V Sharma, G Ahmed, SK Srivastava, and BL Ahuja. Electronic structure of layer type tungsten metal dichalcogenides $WX_2$ (X=S, Se) using Compton

spectroscopy: Theory and experiment. *Journal of Alloys and Compounds*, 470(1):452–460, 2009.

[102] G Arora and BL Ahuja. Compton scattering and electronic properties of tungsten ditelluride. In *Advances in Materials Science and Technology (AMST)*, volume 209 of *Solid State Phenomena*, pages 107–110. Trans Tech Publications Ltd, 2 2014.

[103] L Vadkhiya and BL Ahuja. Electronic and optical properties of iron pyrite. *Journal of Alloys and Compounds*, 509(6):3042–3047, 2011.

[104] D Mali, K Kumar, PK Jangid, G Arora, and BL Ahuja. Electronic structure of tantalum dichalcogenide using Compton scattering technique and density functional theory. *Radiation Physics and Chemistry*, 182:109379, 2021.

[105] U Ahuja, K Kumar, R Joshi, DN Bhavsar, and NL Heda. Electronic properties of mixed molybdenum dichalcogenide MoTeSe: LCAO calculations and Compton spectroscopy. *Physica B: Condensed Matter*, 492:16–22, 2016.

[106] DB Williams and CB Carter. *Transmission Electron Microscopy: A Textbook for Materials Science*. Cambridge library collection. Springer, 2009.

[107] JC Meyer, AK Geim, MI Katsnelson, KP Novoselov, TJ Booth, and SC Roth. The structure of suspended graphene sheets. *Nature*, 446:60–63, 2007.

[108] AM van der Zande, PY Huang, DA Chenet, TC Berkelbach, Y You, GH Lee, TF Heinz, DR Reichman, DA Muller, and JC Hone. Grains and grain boundaries in highly crystalline monolayer molybdenum disulphide. *Nature Materials*, 12(6), 2013.

[109] C Jin, F Lin, K Suenaga, and S Iijima. Fabrication of a freestanding boron nitride single layer and its defect assignments. *Physical Review Letters*, 102:195505, 2009.

[110] A Béché, JL Rouvière, JP Barnes, and D Cooper. Strain measurement at the nanoscale: Comparison between convergent beam electron diffraction, nano-beam electron diffraction, high resolution imaging and dark field electron holography. *Ultramicroscopy*, 131:10–23, 2013.

[111] O Stéphan, D Taverna, M Kociak, K Suenaga, L Henrard, and C Colliex. Dielectric response of isolated carbon nanotubes investigated by spatially resolved electron energy-loss spectroscopy: From multiwalled to single-walled nanotubes. *Phys. Rev. B*, 66:155422, 2002.

[112] RF Egerton. Electron energy-loss spectroscopy in the TEM. *Reports on Progress in Physics*, 72(1):016502, 2008.

[113] W Zhou and ZL Wang. *Scanning Microscopy for Nanotechnology: Techniques and Applications*. Springer ebook collection / Chemistry and Materials Science 2005-2008. Springer New York, 2007.

[114] C Luo, C Wang, X Wu, J Zhang, and J Chu. In situ transmission electron microscopy characterization and manipulation of two-dimensional layered materials beyond graphene. *Small*, 13(35):1604259, 2017.

[115] RF Egerton and M Malac. EELS in the TEM. *Journal of Electron Spectroscopy and Related Phenomena*, 143(2-3):43–50, 2005.

[116] JEOL Ltd. *Diffraction aberration in TEM*, accessed 2020-08-25. `https://www.jeol.co.jp/en/words/semterms/glossary_file/file/diffraction-aberration_01.jpg`.

[117] Eric Kvaalen. *Schematic view of imaging and diffraction modes in TEM*. Licensed by Creative Commons Attribution-Share Alike 4.0 International.

[118] M Varela, Andrew R Lupini, K van Benthem, Albina Y Borisevich, Matthew F Chisholm, Naoya Shibata, E Abe, and Stephen J Pennycook. Materials characterization in the aberration-corrected scanning transmission electron microscope. *Annu. Rev. Mater. Res.*, 35:539–569, 2005.

[119] James P Buban, Quentin Ramasse, Bryant Gipson, Nigel D Browning, and Henning Stahlberg. High-resolution low-dose scanning transmission electron microscopy. *Journal of Electron Microscopy*, 59(2):103–112, 2010.

[120] Stephen J Pennycook and Peter D Nellist. *Scanning transmission electron microscopy: imaging and analysis*. Springer Science & Business Media, 2011.

[121] Rik Brydson. *Aberration-corrected analytical transmission electron microscopy*, volume 3. John Wiley & Sons, 2011.

[122] David J Smith, SJ Pennycook, Martin Castell, Rik Brydson, Rafal Dunin-Borkowski, Paul Midgley, D Bell, E Stach, and Paul O'Brien. *Nanocharacterisation*. Royal Society of Chemistry, 2015.

[123] A Bleloch and A Lupini. Imaging at the picoscale. *Materials Today*, 7(12):42–48, 2004.

[124] Z Cheng, B He, and L Zhou. A general one-step approach for in situ decoration of $MoS_2$ nanosheets with inorganic nanoparticles. *J. Mater. Chem. A*, 3:1042–1048, 2015.

[125] *https://www.jeol.co.jp/en/products/detail/JEM-2100F.html*. September, 2019.

[126] A Cohen, A Patsha, PK Mohapatra, M Kazes, K Ranganathan, L Houben, D Oron, and A Ismach. Growth-etch metal–organic chemical vapor deposition approach of $WS_2$ atomic layers. *ACS Nano*, 15(1):526–538, 2021.

[127] A Gurarslan, Y Yu, L Su, Y Yu, F Suarez, S Yao, Y Zhu, M Ozturk, Y Zhang, and L Cao. Surface-energy-assisted perfect transfer of centimeter-scale monolayer and few-layer $MoS_2$ films onto arbitrary substrates. *ACS Nano*, 8(11):11522–11528, 2014.

[128] Th Carlson. *Photoelectron and Auger spectroscopy*. Springer Science & Business Media, 2013.

[129] G Duscher, R Buczko, SJ Pennycook, and ST Pantelides. Core-hole effects on energy-loss near-edge structure. *Ultramicroscopy*, 86(3-4):355–362, 2001.

[130] AJ Scott, R Brydson, M MacKenzie, and AJ Craven. Theoretical investigation of the ELNES of transition metal carbides for the extraction of structural and bonding information. *Phys. Rev. B*, 63:245105, 2001.

[131] PA Doyle and PS Turner. Relativistic Hartree-Fock X-ray and electron scattering factors. *Acta Crystallographica Section A*, 24(3):390–397, May 1968.

[132] E Kirkland. *Advanced Computing in Electron Microscopy*. Springer US, 01 2010.

[133] WA Reed, P Eisenberger, KC Pandey, and LC Snyder. Electron momentum distributions in graphite and diamond and carbon-carbon bonding. *Phys. Rev. B*, 10:1507–1515, 1974.

[134] U Bonse and W Schröder. Compton profile of graphite measured with 22.1 keV photons and solid state detector. *Physica Status Solidi (a)*, 23(1):297–301, 1974.

[135] R Tyk, J Felsteiner, I Gertner, and R Moreh. Compton-profile anisotropies in graphite and hexagonal boron nitride. *Phys. Rev. B*, 32:2625–2627, Aug 1985.

[136] BG Williams, MK Uppal, and RD Brydson. Dynamical scattering effects in electron scattering measurements of the Compton profiles of solids. *Proceedings of the Royal Society of London. A. Mathematical and Physical Sciences*, 409(1836):161–176, 1987.

[137] J Gao, B Li, J Tan, P Chow, TM Lu, and N Koratkar. Aging of transition metal dichalcogenide monolayers. *ACS Nano*, 10(2):2628–2635, 2016.

[138] RF Egerton. Control of radiation damage in the TEM. *Ultramicroscopy*, 127:100–108, 2013. Frontiers of Electron Microscopy in Materials Science.

[139] R Zan, QM Ramasse, R Jalil, T Georgiou, U Bangert, and KS Novoselov. Control of radiation damage in $MoS_2$ by graphene encapsulation. *ACS Nano*, 7(11):10167–10174, 2013. PMID: 24116975.

[140] DA Muller and J Silcox. Radiation damage of $Ni_3Al$ by 100 keV electrons. *Philosophical Magazine A*, 71(6):1375–1387, 1995.

[141] S Keskin and N de Jonge. Reduced radiation damage in transmission electron microscopy of proteins in graphene liquid cells. *Nano Letters*, 18(12):7435–7440, 2018.

[142] CP Lin, PC Chen, JH Huang, CT Lin, D Wang, WT Lin, CC Cheng, CJ Su, YW Lan, and TH Hou. Local modulation of electrical transport in 2D layered materials induced by electron beam irradiation. *ACS Applied Electronic Materials*, 1(5):684–691, 2019.

[143] X Zhao, J Kotakoski, JC Meyer, E Sutter, P Sutter, AV Krasheninnikov, U Kaiser, and W Zhou. Engineering and modifying two-dimensional materials by electron beams. *MRS Bulletin*, 42(9):667–676, 2017.

[144] Q Chen, C Dwyer, G Sheng, C Zhu, X Li, C Zheng, and Y Zhu. Imaging beam-sensitive materials by electron microscopy. *Advanced Materials*, 32(16):1907619, 2020.

[145] Y Cao, V Fatemi, S Fang, K Watanabe, T Taniguchi, E Kaxiras, and P Jarillo-Herrero. Unconventional superconductivity in magic-angle graphene superlattices. *Nature*, 556(7699):43–50, 2018.

[146] R Bistritzer and AH MacDonald. Moiré bands in twisted double-layer graphene. *Proceedings of the National Academy of Sciences*, 108(30):12233–12237, 2011.

[147] L Wang, EM Shih, A Ghiotto, L Xian, DA Rhodes, C Tan, M Claassen, DM Kennes, Y Bai, B Kim, K Watanabe, T Taniguchi, X Zhu, J Hone, A Rubio, AN Pasupa-

thy, and CR Dean. Correlated electronic phases in twisted bilayer transition metal dichalcogenides. *Nature materials*, 19(8):861–866, 2020.

[148] A Castellanos-Gomez, HSJ van der Zant, and GA Steele. Folded $MoS_2$ layers with reduced interlayer coupling. *Nano Research*, 7(4):572–578, 2014.

[149] SJ Clark, MD Segall, CJ Pickard, PJ Hasnip, MIJ Probert, Ke Refson, and MC Payne. First principles methods using castep. *Zeitschrift für kristallographie-crystalline materials*, 220(5-6):567–570, 2005.

[150] P Homm, M Menghini, JW Seo, S Peters, and JP Locquet. Room temperature Mott metal–insulator transition in $V_2O_3$ compounds induced via strain-engineering. *APL Materials*, 9(2):021116, 2021.

[151] N Jiang. Electron beam damage in oxides: a review. *Reports on Progress in Physics*, 79(1):016501, 2015.

[152] DS Su, M Wieske, E Beckmann, A Blume, G Mestl, and R Schlögl. Electron beam induced reduction of $V_2O_5$ studied by analytical electron microscopy. *Catalysis letters*, 75(1):81–86, 2001.

[153] KH Kim, DK Roh, IK Song, BC Lee, and SH Baeck. Enhanced performance as a lithium-ion battery cathode of electrodeposited $V_2O_5$ thin films by e-beam irradiation. *Journal of Solid State Electrochemistry*, 14(10):1801–1805, 2010.

[154] L Laffont, MY Wu, F Chevallier, P Poizot, M Morcrette, and JM Tarascon. High resolution EELS of Cu–V oxides: Application to batteries materials. *Micron*, 37(5):459–464, 2006.

[155] BDA Levin. Direct detectors and their applications in electron microscopy for materials science. *Journal of Physics: Materials*, 4(4):042005, 2021.

[156] S Cheng, A Pofelski, P Longo, RD Twesten, Y Zhu, and GA Botton. The performance evaluation of direct detection electron energy-loss spectroscopy at 200 kV and 80 kV accelerating voltages. *Ultramicroscopy*, 212:112942, 2020.

[157] I Timrov, M Markov, T Gorni, M Raynaud, O Motornyi, R Gebauer, S Baroni, and N Vast. Ab initio study of electron energy loss spectra of bulk bismuth up to 100 eV. *Physical Review B*, 95(9):094301, 2017.